Lecture Notes

Fluid Mechanics of Turbomachines II

N.P. Kruyt

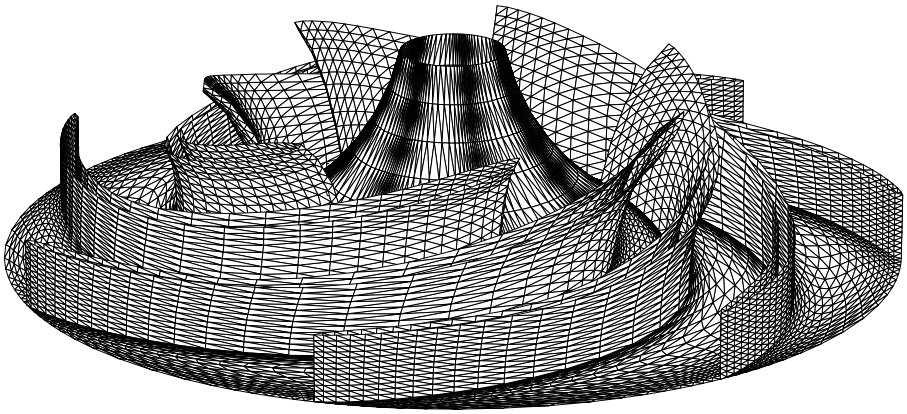

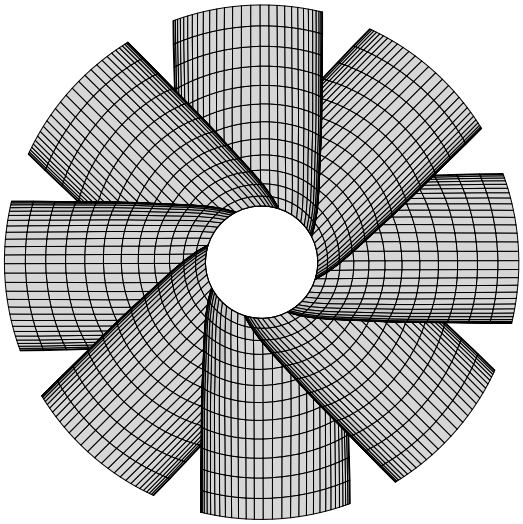

Turbomachinery Laboratory
Engineering Fluid Dynamics
Department of Mechanical Engineering
University of Twente
The Netherlands

Last updated April 19 2005

CONTENTS

CHAPTER 1

Introduction

Classical methods for designing turbomachinery are based on scaling relations for non-dimensional numbers, like the flow number and the head coefficient, and experimental correlations to correct for the limitations of one-dimensional flow-analysis methods. One approach to improving the design of turbomachinery is formed by more detailed analyses of the flow phenomena that occur in such machinery. The results of such analyses indicate what part of the geometry of the machine must be modified in order to improve its performance. Preferably, such analyses also give a quantification of the performance. In addition, such simulations can enhance the qualitative understanding of the flow. Of course, experimental validation is always required, but an analysis tool makes it possible to greatly reduce the required number of experiments: the analysis tool forms a "computer wind tunnel". Furthermore, computer simulations can generally be performed much more rapidly than real, physical experiments. Hence, the cost (in time and money) of such "computer experiments" is usually much smaller than that of the corresponding physical experiments.

The objective of this course is therefore to give more detailed knowledge of the flow in turbomachinery, in particular of pumps and fans for which the compressibility of the fluid can be neglected. Hence, this course goes beyond the simple one-dimensional methods that are discussed in the course Turbomachinery I. These one-dimensional methods give a thorough qualitative understanding of the basic physics, and of the energy transfer in particular.

Generally the flow field in turbomachines is very complicated, due to its three-dimensional nature and the rapidly changing curvature of the passages in rotating impellers. In addition, turbomachines exhibit unsteady behaviour as a result of the interaction between rotating and stationary parts. Considering these complexities, most analyses of the flow fields are based on numerical methods for solving the simplified governing equations.

This chapter gives some mathematical notations and mathematical theorems that will be used subsequently.

Mathematical notation

The magnitude (or length) of a vector $\underline{a} = (a_x, a_y, a_z)^T$ is defined by

$$\|\underline{a}\| = \sqrt{a_x^2 + a_y^2 + a_z^2} \tag{1.1}$$

inner product

The inner product of two vectors $\underline{a} = (a_x, a_y, a_z)^T$ and $\underline{b} = (b_x, b_y, b_z)^T$ is a scalar defined by

$$\underline{a} \bullet \underline{b} = a_x b_x + a_y b_y + a_z b_z \tag{1.2}$$

The inner product equals $\underline{a} \bullet \underline{b} = \|\underline{a}\| \|\underline{b}\| \cos\theta$, where θ is the angle between the vectors $\underline{a}$ and $\underline{b}$. Note that the two vectors are perpendicular (or orthogonal) when $\underline{a} \bullet \underline{b} = 0$.

The cross product (or outer product) of two vectors $\underline{a} = (a_x, a_y, a_z)^T$ and $\underline{b} = (b_x, b_y, b_z)^T$ is a vector defined by

cross product

$$\underline{a} \times \underline{b} = (a_y b_z - a_z b_y,\ a_z b_x - a_x b_z,\ a_x b_y - a_y b_x)^T \tag{1.3}$$

The cross product $\underline{c} = \underline{a} \times \underline{b}$ is a vector that is perpendicular to the vectors $\underline{a}$, $\underline{b}$ and its magnitude is equal to $\|\underline{a}\| \|\underline{b}\| \sin\theta$, where θ is the angle between the vectors $\underline{a}$ and $\underline{b}$.

divergence

The *divergence* of a vector field $\underline{v}(x, y, z, t) = (v_x(x, y, z, t), v_y(x, y, z, t), v_z(x, y, z, t))^T$ is a scalar field defined by

$$\underline{\nabla} \bullet \underline{v} = \frac{\partial v_x}{\partial x} + \frac{\partial v_y}{\partial y} + \frac{\partial v_z}{\partial z} \tag{1.4}$$

where v_x, v_y and v_z are the (Cartesian) components of the velocity vector $\underline{v}$.

gradient, rotation (curl)

The *gradient* $\underline{\nabla}\phi$ of a scalar field $\phi(x, y, z, t)$ and the *rotation* (or curl) $\underline{\nabla} \times \underline{v}$ of a vector field $\underline{v}(x, y, z, t)$ are vector fields that are defined by

$$\nabla\phi = \begin{bmatrix} \frac{\partial \phi}{\partial x} \\ \frac{\partial \phi}{\partial y} \\ \frac{\partial \phi}{\partial z} \end{bmatrix} \qquad \underline{\nabla} \times \underline{v} = \begin{bmatrix} \frac{\partial v_z}{\partial y} - \frac{\partial v_y}{\partial z} \\ \frac{\partial v_x}{\partial z} - \frac{\partial v_z}{\partial x} \\ \frac{\partial v_y}{\partial x} - \frac{\partial v_x}{\partial y} \end{bmatrix} \tag{1.5}$$

Now some examples will be given. Consider the first velocity field

$$\underline{v} = \frac{q}{2\pi}\left(\frac{x}{x^2 + y^2}, \frac{y}{x^2 + y^2}, 0\right)^T \tag{1.6}$$

This velocity field, corresponding to a two-dimensional source of strength q at the origin, has zero divergence, except at the origin where the velocity is singular. The rotation, or curl of this velocity field is zero, i.e. $\underline{\nabla} \times \underline{v} = (0, 0, 0)^T$.

In the second example the velocity field is

$$\underline{v} = \Omega(-y, x, 0)^T \tag{1.7}$$

This velocity field corresponds to a rigid-body rotation around the z-axis with angular speed Ω. It has zero divergence and its rotation (or curl) equals $\underline{\nabla} \times \underline{v} = (0, 0, 2\Omega)^T$.

Stokes theorem is

Stokes theorem

$$\oint_C \underline{v} \bullet d\underline{s} = \int_S (\nabla \times \underline{v}) \bullet d\underline{A} \tag{1.8}$$

where C is a closed contour around surface S.

Gauss theorem, or divergence theorem, for an arbitrary function $\phi(\boldsymbol{x})$ is

Gauss theorem; divergence theorem

$$\int_V \nabla\phi \, dV = \int_S \phi \underline{n} \, dS \tag{1.9}$$

where V is a volume with closed boundary S and the outward unit normal vector on surface S is $\underline{n}$.

CHAPTER 2

Flow equations

This chapter deals with the conservation laws of physics. Then these conservation laws are made nondimensional. By a closer analysis of conditions prevalent in turbomachines, the conservation laws are simplified. Firstly, the definition of vorticity will be introduced.

Vorticity

vorticity

A quantity of great interest in fluid dynamics is vorticity $\underline{\omega}$, which is defined as

$$\underline{\omega} = \nabla \times \underline{v}, \tag{2.1}$$

where $\underline{v}$ is the velocity vector. This can be interpreted as twice a local angular velocity of a fluid element [1]. For instance, for a rigid body motion with angular velocity $\underline{\Omega}$, the velocity is given by $\underline{v} = \underline{\Omega} \times \underline{r}$ with position vector $\underline{r}$ and hence the vorticity is indeed $\underline{\omega} = 2\underline{\Omega}$.

Material derivative

material derivative
convective derivative

Here the time derivative, when following a fluid particle, of a quantity like temperature will be determined. This is the material derivative, or convective derivative.

Now consider the change in ϕ of a fluid particle. This quantity changes due to the time-dependent change and due to the movement of the fluid

$$\begin{aligned} \frac{D\phi}{Dt} &= \lim_{\Delta t \to 0} \frac{\phi(\underline{x} + \underline{v}\Delta t,\, t + \Delta t) - \phi(\underline{x},\, t)}{\Delta t} \\ &= \lim_{\Delta t \to 0} \frac{\left[\phi(\underline{x},\, t) + \dfrac{\partial \phi}{\partial t}\Delta t + \Delta t \underline{v} \bullet \nabla \phi\right] - \phi(\underline{x},\, t)}{\Delta t} \\ &= \frac{\partial \phi}{\partial t} + \underline{v} \bullet \nabla \phi \end{aligned} \tag{2.2}$$

The second step in this derivation follows from a Taylor expansion. Note that after a time interval of Δt the fluid particle that is at position $\underline{x}$ at time t will have moved to position $\underline{x} + \underline{v}\Delta t$. The material derivative consists of two terms, a local time derivative and a convective term.

Reynolds transport theorem

Consider an arbitrary extensive quantity Φ of a *system* (i.e. consisting of moving fluid particles) with corresponding intensive quantity ϕ (per unit mass)

$$\Phi|_{\text{system}} = \int_{V(\text{system})} \rho(\underline{x}, t)\phi(\underline{x}, t)dV \tag{2.3}$$

Then Reynolds transport theorem [2] states

Reynolds transport theorem

$$\begin{aligned} \left.\frac{d\Phi}{dt}\right|_{\text{system}} &= \int_V \rho(\underline{x}, t)\frac{\partial}{\partial t}\phi(\underline{x}, t)dV + \int_S \rho(\underline{x}, t)\phi(\underline{x}, t)[\underline{v}(\underline{x}, t) \bullet \underline{n}]dS \\ &= \int_V \rho(\underline{x}, t)\frac{D\phi(\underline{x}, t)}{Dt}dV \end{aligned} \tag{2.4}$$

where the second equality follows from Gauss theorem (1.9) and the definition (2.2) of the material derivative.

Conservation laws

The general conservation equations of fluid mechanics will be given here. These are [1]

- conservation of mass
- conservation of momentum
- conservation of angular momentum
- conservation of energy

Conservation of mass

The conservation law of mass, or continuity equation, is

conservation of mass; continuity equation

$$\frac{D\rho}{Dt} + \rho\nabla\bullet\underline{v} = 0 \tag{2.5}$$

where ρ is the density, $\underline{v}$ is the velocity vector.

Conservation of momentum

The conservation laws of momentum, or Navier Stokes equations are

conservation of momentum; Navier-Stokes equations

$$\begin{aligned} \rho\frac{D\underline{v}}{Dt} &= \nabla\bullet\sigma + \rho\underline{f} \\ &= -\nabla p + \nabla\bullet\sigma' + \rho\underline{f} \end{aligned} \tag{2.6}$$

where σ is the total stress tensor, p is the pressure, σ' is the deviatoric stress tensor and $\underline{f}$ denotes body forces like gravity. The deviatoric stress tensor is the part of the stress tensor excluding the hydrostatic part (pressure). Hence the total stress tensor and the deviatoric stress tensor are related by

deviatoric stress

$$\sigma = -pI + \sigma' \tag{2.7}$$

where I is the identity tensor
For the Newtonian fluids that are considered here the deviatoric stress σ' is related linearly to the strain rate

Newtonian fluid

$$\sigma' = \mu\left[\nabla\underline{v} + (\nabla\underline{v})^T - \frac{2}{3}I\nabla\bullet\underline{v}\right] \tag{2.8}$$

index notation

In index notation a summation over *repeated* subscripts is implied. For example

$$\cdot\frac{\partial v_i}{\partial x_i} = \frac{\partial v_1}{\partial x_1} + \frac{\partial v_2}{\partial x_2} + \frac{\partial v_3}{\partial x_3} = \nabla\bullet\underline{v} \tag{2.9}$$

Another example is

$$\frac{\partial^2\phi}{\partial x_j\partial x_j} = \frac{\partial^2\phi}{\partial x_1^2} + \frac{\partial^2\phi}{\partial x_2^2} + \frac{\partial^2\phi}{\partial x_3^2} = \nabla^2\phi \tag{2.10}$$

In index notation, the expression (2.8) for the deviatoric stress tensor becomes

$$\sigma'_{ij} = \mu\left(\frac{\partial v_i}{\partial x_j} + \frac{\partial v_j}{\partial x_i} - \frac{2}{3}\delta_{ij}\frac{\partial v_k}{\partial x_k}\right) \tag{2.11}$$

dynamic viscosity; kinematic viscosity

where μ is the dynamic viscosity of the fluid and δ_{ij} is the Kronecker symbol: $\delta_{ij} = 1$ if $i = j$ and $\delta_{ij} = 0$ otherwise. The last term in between the brackets is such as to make $\sigma'_{ii} = 0$. The kinematic viscosity ν is defined by $\nu = \mu/\rho$.

Conservation of angular momentum

The conservation law of angular momentum is

conservation of angular momentum

$$\underline{\sigma}' = \underline{\sigma}'^T \qquad \sigma'_{ij} = \sigma'_{ji} \tag{2.12}$$

which means that the deviatoric stress tensor $\underline{\sigma}'$, and hence the total stress tensor σ, is symmetric.
Note that this conservation law is automatically satisfied for a Newtonian fluid.

Conservation of energy

The conservation law of energy of energy, or the first law of thermodynamics, can be stated as follows: for a *system* composed of fluid particles, the change of the sum of the kinetic energy and the internal energy equals the sum of work done on the system (per unit time), W, and the heat added *to* the system (per unit time), Q. The kinetic energy of the system K and the internal energy E are defined by

$$K = \int_{V(\text{system})} \rho\frac{1}{2}v_i v_i dV \qquad E = \int_{V(\text{system})} \rho e dV \tag{2.13}$$

In this section index notation is used once more, implying a summation over repeated subscripts. For example, in the term $v_i v_i$ a summation over the i index is implied.
The work done on the system, W, consists of work done by volume forces and of work done by surface forces

$$W = \int_V \rho v_i f_i dV + \int_S v_i(\sigma_{ij} n_j) dS \tag{2.14}$$

The heat added to the system is given by

$$Q = -\int_S q_j n_j dS \tag{2.15}$$

where q_i is the heat-flux vector at the boundary. The minus sign for the heat-flux term is present since the normal vector n_i is directed outward.

The conservation of energy equation, $d(K+E)/dt = W + Q$, now becomes upon use of Reynolds transport theorem (2.4)

$$\int_V \rho \frac{D}{Dt}\left(\frac{1}{2} v_i v_i + e\right) dV = \int_V v_i f_i dV + \int_S v_i(\sigma_{ij} n_j) dS - \int_S q_j n_j dS \tag{2.16}$$

Using Gauss theorem (1.9) for the surface integrals and noting that the result must hold for any volume V we obtain

$$\rho \frac{D}{Dt} e - \sigma_{ij} \frac{\partial v_i}{\partial x_j} + \frac{\partial q_j}{\partial x_j} = v_i \left(\frac{\partial \sigma_{ij}}{\partial x_j} + \rho f_i - \rho \frac{D}{Dt} v_i \right) \tag{2.17}$$

The term inside the brackets equals zero, as follows from the conservation law of momentum (2.6). The conservation law of energy becomes

conservation of energy

$$\rho \frac{D}{Dt} e = \sigma_{ij} \frac{\partial v_i}{\partial x_j} - \frac{\partial q_j}{\partial x_j} \tag{2.18}$$

The heat-flux vector q_i is defined by Fourier's law

Fourier's law

$$q_i = -\lambda \frac{\partial T}{\partial x_i} \tag{2.19}$$

where T is the absolute temperature and λ is the heat-conduction coefficient, which is assumed to be constant (and isotropic).

Using the Gibbs thermodynamic relation $Tds = de + pd\upsilon$ (with υ the specific volume, i.e. $\upsilon = 1/\rho$), the decomposition of stress (2.7) and the continuity equation (2.5), we obtain the dissipation equation

dissipation equation

$$\rho T \frac{Ds}{Dt} = \lambda \nabla^2 T + \sigma' : \nabla \underline{v} \tag{2.20}$$

The term on the left-hand side gives the increase in entropy s, the first term on the right-hand side gives the conduction of heat, while the second term on the right-hand side gives the dissipation due to viscosity. In index notation this second term is $\sigma'_{ij} \partial v_j / \partial x_i$, where again a summation over the i and j subscripts is implied.

In the energy equation a number of thermodynamic quantities are present. To complete the system of equations, a thermodynamic equation of state is required that describes the thermodynamic properties of the fluid. In general, relations for the temperature T, pressure p and internal energy e are necessary

$$e = e(s, \rho) \qquad T = \left(\frac{\partial e}{\partial s}\right)_\rho \qquad p = -\left(\frac{\partial e}{\partial\left(\frac{1}{\rho}\right)}\right)_s \tag{2.21}$$

ideal gas

For an ideal gas with constant specific heat coefficients c_p and c_v

$$e = c_v T \qquad \frac{p}{\rho} = RT \qquad s - s_{\text{ref}} = c_p \ln\frac{T}{T_{\text{ref}}} - R\ln\frac{p}{p_{\text{ref}}} \tag{2.22}$$

where R is the gas constant (with $R = c_p - c_v$) and s_{ref}, T_{ref} and p_{ref} are entropy, temperature and pressure at a reference state.

Dimensional analysis

dimensional analysis

In general the governing equations are (hardly) solvable due to their complicated and nonlinear character. A suitable means to investigate whether a simplification is feasible in specific circumstances is by *dimensional analysis*.
Firstly, all variables are made nondimensional by scaling them with a quantity that is characteristic for the situation at hand. The new, nondimensional variables will then be of order of magnitude 1. For instance, the velocities $\underline{v}$ are written as $\underline{v} = U\underline{v}^*$, where $\underline{v}^*$ is the nondimensional velocity and U is a characteristic velocity scale.
The variables of interest are made nondimensional as follows:

$$\begin{gathered} \underline{v} = U\underline{v}^* \qquad \nabla = \frac{\nabla^*}{L} \qquad t = \frac{L}{U}t^* \qquad \rho = \rho_0\rho^* \\ T = T_0 T^* \qquad p = \rho_0 U^2 p^* \qquad s = c_p s^* \end{gathered} \tag{2.23}$$

Nondimensional variables are denoted with a *. U is a characteristic velocity, L is a characteristic length, ρ_0 is a characteristic density, T_0 is a characteristic temperature.
The nondimensional equations for a Newtonian fluid that result are

$$\frac{D\rho}{Dt} + \rho\nabla\bullet\underline{v} = 0 \tag{2.24}$$

$$\frac{D\underline{v}}{Dt} = -\frac{1}{\rho}\nabla p + \frac{1}{Re}\nabla\bullet\sigma' \tag{2.25}$$

$$\rho T\frac{Ds}{Dt} = \frac{1}{RePr}\nabla^2 T + \frac{Ec}{Re}\sigma' : \nabla\underline{v} \tag{2.26}$$

where the nondimensional variables are denoted *without* a * for the sake of convenience!
The nondimensional numbers present in these equations are respectively the Reynolds, Prandtl, Péclet and Eckert numbers

Reynolds number

$$Re = \frac{\rho_0 UL}{\mu} = \frac{\text{inertia forces}}{\text{viscous forces}} \tag{2.27}$$

$$Pr = \frac{c_p\mu}{\lambda} = \frac{\text{viscous dissipation}}{\text{thermal dissipation}} \tag{2.28}$$

$$Pe = RePr = \frac{\text{entropy increase}}{\text{heat conduction}} \tag{2.29}$$

$$Ec = \frac{U^2}{c_p T_0} = \frac{\text{kinetic energy}}{\text{thermal energy}} \tag{2.30}$$

Two limiting cases can be distinguished: (i) creeping flows with $Re \ll 1$ where inertia terms can be neglected relative to viscous terms and (ii) inviscid flows with $Re \gg 1$ where viscous terms can be neglected relative to inertia terms.

The flow conditions in turbomachinery are usually such that $Re \gg 1$. Typical values for the characteristic scales are L = 1 m, U = 1 m/s, $\nu_{air} = 1\times10^{-5}$ m^2/s, $\nu_{water} = 1\times10^{-6}$ m^2/s, corresponding to Reynolds numbers $Re = 10^5 - 10^6$.

The Prandtl and Eckert numbers are usually of the order of magnitude 1, so

$$\frac{1}{Re} \ll 1 \qquad \frac{1}{RePr} \ll 1 \qquad \frac{Ec}{Re} \ll 1 \tag{2.31}$$

This implies that for flows with large Reynolds number the viscous terms can be neglected from the momentum equations.

A similar consideration of the dissipation equation shows that for large Reynolds numbers the flow can be considered as isentropic

isentropic flow

$$\frac{Ds}{Dt} = 0 \tag{2.32}$$

boundary layers

A consequence of neglecting the viscous terms is that, in mathematical terms, the order of the governing partial differential equations is reduced. This means that not all boundary conditions can be enforced. The stick condition (or no-slip condition) at solid walls can not be enforced, but only that there is no flow through solid walls. This means that the assumptions made are not valid near a solid wall, where a boundary layer will be present. The same applies to wakes. Hence, regions near the wall and in wakes have to be analysed differently. This is the subject of boundary-layer theory, see also Chapter 8.

Inviscid flow

inviscid flow

When the viscous terms are neglected we speak of *inviscid flow*. Note that these are not only a property of the fluid, but also of the flow conditions. The governing equations of inviscid flows are

$$\frac{D\rho}{Dt} + \rho\nabla\bullet\underline{v} = 0 \qquad \text{conservation of mass} \tag{2.33}$$

Euler equations

$$\frac{D\underline{v}}{Dt} = -\frac{1}{\rho}\nabla p + \underline{g} \qquad \text{Euler equations} \tag{2.34}$$

$$\frac{Ds}{Dt} = 0 \qquad \text{isentropic flow} \tag{2.35}$$

These equations can not be used when viscous terms are important, such as in boundary layers, wakes and turbulence.

Turbulence

Most of the flows in turbomachines are turbulent, with laminar and transitional regimes occurring near the leading edges of impeller and diffuser blades. Turbulence is characterised by irregular fluctuations. Its origin is often the result of instability of the laminar flow.

In most theories of turbulence the so-called Reynolds averaging is employed, see [30]. The velocity is decomposed into a time-averaged value and a fluctuating part. Substitution of this decomposition into the Navier-Stokes equations leads to an extra term in the Navier-Stokes equations. This extra term, the Reynolds stress, consists of the correlation between the fluctuations. The problem is that this correlation is not related (directly) to the time-averaged velocity, which is the primary variable in the Reynolds-averaged Navier-Stokes equations. Thus, there is a *closure problem* in turbulence. Assumptions have to be made for this correlation term, i.e. extra equations relating the correlations to primary variables like the time-averaged velocity. The subject of turbulence modelling is a vast and important field in itself, but it is beyond the scope of this course.

An overview of turbulence modelling in the context of turbomachinery is given in [14].

Irrotational flow

A further simplification of inviscid flow is obtained by considering *irrotational* flows. Before proceeding with a discussion of these, Kelvin's (or Thompson's) theorem of conservation of circulation for inviscid flows will be derived. Circulation around a closed contour C is defined by

circulation

$$\Gamma(C) = \oint_C \underline{v} \bullet \underline{ds} \tag{2.36}$$

The material derivative of the circulation is

$$\frac{D}{Dt}\Gamma(C) = \oint_C \frac{D}{Dt}\underline{v} \bullet \underline{ds} + \oint_C \underline{v} \bullet \frac{D}{Dt}\underline{ds} \tag{2.37}$$

The second term of the right-hand side equals zero, since $D\underline{ds}/Dt = d\underline{v}$ and $\oint_C \underline{v} \bullet d\underline{v} = (1/2)\oint_C d(v^2) = 0$. Using Stokes theorem (1.8), the first term can be written as

$$\oint_C \frac{D}{Dt}\underline{v} \bullet \underline{ds} = \int_S \left(\nabla \times \frac{D}{Dt}\underline{v}\right) \bullet \underline{dA} \tag{2.38}$$

From the Euler equation (2.34) it follows that this equation can be rewritten as

$$\int_S \left(\nabla \times \frac{D}{Dt}\underline{v}\right) \bullet \underline{dA} = -\int_S \frac{1}{\rho}(\nabla \times \nabla p) \bullet \underline{dA} = 0, \tag{2.39}$$

since $\nabla \times \nabla \phi = 0$ for an arbitrary scalar function ϕ. The result is Kelvin's circulation theorem

Kelvin's circulation theorem

$$\frac{D}{Dt}\Gamma = 0 \tag{2.40}$$

In words this means that, when moving with the flow, circulation does not change in inviscid flows.
Application of Stokes theorem gives

$$\Gamma = \oint_C \underline{v} \bullet \underline{ds} = \int_S (\nabla \times \underline{v}) \bullet \underline{dA} = \text{constant} \qquad \textbf{(2.41)}$$

when following the flow.
An important consequence of this theorem is that when the *inflow* is irrotational for inviscid flow, the flow *remains* irrotational. Then the flow is *irrotational* everywhere!

irrotational flow

$$\nabla \times \underline{v} = \underline{0} \qquad \textbf{(2.42)}$$

Potential flow

potential flow

In this section deals with the simplifications that are possible by considering irrotational flows. For irrotational flows it is possible to define a *velocity potential* ϕ such that the gradient of the potential gives the velocity

velocity potential

$$\underline{v} = \nabla \phi \qquad \textbf{(2.43)}$$

For instance, in the two-dimensional case with velocity vector $\underline{v} = (u, v, 0)^T$, the only non-zero component of $\nabla \times \underline{v}$ is in the third direction with component $\partial v / \partial x - \partial u / \partial y$. With $u = \partial \phi / \partial x$ and $v = \partial \phi / \partial y$ this component of $\nabla \times \underline{v}$ is always zero.
Note that the number of unknown quantities is greatly reduced. Instead of three unknown components of the velocity, only the velocity potential is unknown.
The law of conservation of mass now becomes

$$\frac{1}{\rho}\frac{\partial \rho}{\partial t} + \frac{1}{\rho}\nabla \phi \bullet \nabla \rho + \nabla^2 \phi = 0 \qquad \text{conservation of mass} \qquad \textbf{(2.44)}$$

The Euler equations can be simplified using the vector identity

$$\underline{v} \bullet \nabla \underline{v} = \frac{1}{2}\nabla(\underline{v} \bullet \underline{v}) + (\nabla \times \underline{v}) \times \underline{v} \qquad \textbf{(2.45)}$$

Note that the last term on the right-hand side is zero for irrotational flows, see (2.42). From the thermodynamic relation $dh = Tds + (1/\rho)dp$ for isentropic flows ($ds = 0$, see (2.35)), we find $(1/\rho)\nabla p = \nabla h$. Hence

$$\frac{D\underline{v}}{Dt} + \nabla h = 0 \Rightarrow \frac{\partial}{\partial t}\nabla \phi + \frac{1}{2}\nabla(\underline{v} \bullet \underline{v}) + \nabla h = 0 \qquad \textbf{(2.46)}$$

and we obtain the unsteady Bernoulli equation

unsteady Bernoulli equation

$$\frac{\partial \phi}{\partial t} + \frac{1}{2}\underline{v} \bullet \underline{v} + h = c(t) \qquad \textbf{(2.47)}$$

Note that this result is also valid for compressible flow.
For an ideal gas we have

$$h = c_p T \qquad p = \text{const}\rho^{\gamma} \qquad \textbf{(2.48)}$$

where the second relation is a form of the Poisson relations for isentropic processes, with $\gamma = c_p/c_v$ is the ratio of the specific heat coefficients.

Incompressible potential flow

In this section the case of *incompressible* flow is considered, for which the density ρ is constant. Now we will investigate when this is the case. For isentropic flows there is a relation between density ρ and pressure $p = p(\rho)$. Hence

$$\delta\rho = \left(\frac{\partial\rho}{\partial p}\right)_s \delta p = a^{-2}\delta p \qquad \textbf{(2.49)}$$

where a is the speed of sound. For inviscid flows pressure differences $\delta p \propto \rho U^2$, as follows from the Bernoulli equation. Hence the relative change in density is given by

Mach number

$$\frac{\delta\rho}{\rho} \propto \left(\frac{U}{a}\right)^2 = Ma^2 \qquad \textbf{(2.50)}$$

where Ma is the nondimensional Mach number, the ratio of a characteristic velocity of the flow over the speed of sound. For an ideal gas the sped of sound is given by $a = \sqrt{\gamma RT}$.

In many cases the assumption of incompressible flow is valid, such as in pumps and fans. In other cases, such as compressors and gas turbines, this assumption is invalid. A rule of thumb is that the flow may be considered as incompressible when $Ma < 0.3$.

For incompressible flow the conservation of mass equation (2.5) reduces to $\nabla\bullet\underline{v} = 0$. Using the expression (2.43) for the velocity in terms of the velocity potential, the conservation of mass equation results in the Laplace equation

Laplace equation

$$\nabla^2\phi = 0 \qquad \text{conservation of mass} \qquad \textbf{(2.51)}$$

and the unsteady Bernoulli equation is

$$\frac{\partial\phi}{\partial t} + \frac{1}{2}\underline{v}\bullet\underline{v} + \frac{p}{\rho} = c(t) \qquad \text{unsteady Bernoulli equation} \qquad \textbf{(2.52)}$$

Note that the actual value of $c(t)$ is not relevant when determining pressure *differences*.

superposition principle

An important observation is that the Laplace equation (2.51) is *linear*. This is a major advantage of the simplifications that were introduced (besides the reduction in the number of variables). Linear equations satisfy the superposition principle: for two solution ϕ_1 and ϕ_2 that satisfy the Laplace equation we have that the linear combination $\phi = c_1\phi_1 + c_2\phi_2$ (with arbitrary c_1 and c_2) also satisfies the Laplace equation, as can be easily verified.

Summarising, the equations that describe incompressible potential-flows are

$$\nabla^2\phi = 0 \qquad \underline{v} = \nabla\phi \qquad \frac{\partial\phi}{\partial t} + \frac{1}{2}\underline{v}\bullet\underline{v} + \frac{p}{\rho} = c(t) \qquad \textbf{(2.53)}$$

Firstly, the velocity potential ϕ has to be determined by the first equation of (2.53) (with appropriate boundary conditions). Secondly, the velocity field $\underline{v}$ is computed from the second equation of (2.53). Finally, the pressure is determined from the last equation of (2.53).

The assumptions that lead to the equations (2.53) that describe incompressible potential flows are summarised by

overview of assumptions

- Inviscid flow corresponding to $Re \gg 1$ (does not apply in attached boundary layers and wakes; boundary layers should not separate, since the vorticity present in the boundary layers is then introduced in the main flow)
- Incompressible flow corresponding to $Ma^2 \ll 1$
- Irrotational inflow

Potential flow in the rotating frame

absolute frame of reference; rotating frame of reference

Up to now, the equations have been formulated with respect to an absolute frame of reference (or inertial frame of reference), i.e. one where the observer does not move. In many cases it is more natural to consider the flow in the rotating frame of reference, i.e. the frame of reference that rotates with the rotor. The observer of the flow would then see the *relative velocity*, while an observer in an absolute frame of reference sees the *absolute* velocity. For instance, at the design point the flow in the impeller may be assumed to be steady in the rotating frame of reference, while it is unsteady in the absolute frame of reference.

relative velocity; absolute velocity

The absolute velocity $\underline{v}$ and the relative velocity $\underline{w}$ are related by

$$\underline{v} = \underline{w} + \underline{\Omega} \times \underline{r} \tag{2.54}$$

where $\underline{\Omega}$ is the angular velocity of the rotating frame of reference and $\underline{r}$ is the position vector. The second term on the right-hand side gives the (local) blade velocity.

Since

$$\nabla \bullet (\underline{\Omega} \times \underline{r}) = 0 \qquad \nabla \times (\underline{\Omega} \times \underline{r}) = 2\underline{\Omega} \tag{2.55}$$

it follows that

$$\nabla \bullet \underline{w} = 0 \qquad \nabla \times \underline{w} = -2\underline{\Omega} \tag{2.56}$$

The second of these equations implies that the *relative velocity is not irrotational* when the absolute velocity is irrotational! Therefore it is *not* possible to define a potential ξ such that $\underline{w} = \nabla\xi$.

Since the change of scalar variable when following a fluid element, which is the meaning of the material derivative, is identical in the relative and the absolute frame of reference, it follows that

$$\left.\frac{\partial \phi}{\partial t}\right|_R + \underline{w} \bullet \nabla\phi \equiv \left.\frac{D\phi}{Dt}\right|_R = \frac{D\phi}{Dt} \equiv \frac{\partial \phi}{\partial t} + \underline{v} \bullet \nabla\phi \tag{2.57}$$

where the subscript *R* denotes that the time derivative is to be taken relative to the rotating frame of reference. Note that the expression for the material derivative in the rotating frame of reference involves the *relative* velocity.

Now the Bernoulli equation in the rotating frame of reference becomes

$$\left.\frac{\partial \phi}{\partial t}\right|_R + (\underline{w} - \underline{v}) \bullet \nabla\phi + \frac{1}{2}\underline{v} \bullet \underline{v} + \frac{p}{\rho} = c(t) \tag{2.58}$$

Using the definition of potential and the relations between absolute and relative velocities, this equation can be expressed in terms of relative velocities as

Bernoulli equation in the rotating frame

$$\left.\frac{\partial \phi}{\partial t}\right|_R + \frac{1}{2}\underline{w} \bullet \underline{w} + \frac{p}{\rho} - \frac{1}{2}(\underline{\Omega} \times \underline{r}) \bullet (\underline{\Omega} \times \underline{r}) = c(t) \tag{2.59}$$

In an impeller with a vaneless diffuser, where there is no influence of the stationary parts on the rotating parts, one would have a steady flow field in the rotating frame of reference. This is the so-called "free impeller" assumption. Hence

"free impeller" assumption

$$\left.\frac{\partial \phi}{\partial t}\right|_R = 0 \tag{2.60}$$

free impeller case

This means that the potential field is stationary for an observer that rotates with the impeller. This is the "free impeller" case. In this case the flow in each of the channels formed by two consecutive blades will be identical.

Rothalpy

For flows that are steady in the rotating frame, it follows from the Bernoulli equation in the rotating frame of reference (2.59) that the rothalpy I is constant

$$I = \text{constant} \tag{2.61}$$

For incompressible flow rothalpy is defined by

rothalpy

$$I = \frac{p}{\rho} + \frac{1}{2}\underline{w} \bullet \underline{w} - \frac{1}{2}(\underline{\Omega} \times \underline{r}) \bullet (\underline{\Omega} \times \underline{r}) \tag{2.62}$$

Counter vortex

If the flow in the inlet is irrotational, this has important consequences for the flow in the impeller. For an irrotational absolute velocity, the *relative* velocity is *not* irrotational, see (2.56).

These consequences are analysed in more detail for a simple model problem. This is the case of the two-dimensional flow between straight infinitely-long impeller blades. This geometry is sketched in Figure 2.1

The relative velocity then satisfies (2.56). In polar coordinates (r, θ) these equations become [1]

$$\begin{aligned} \frac{1}{r}\frac{\partial}{\partial r}(r w_r) + \frac{1}{r}\frac{\partial w_\theta}{\partial \theta} &= 0 \\ \frac{1}{r}\frac{\partial}{\partial r}(r w_\theta) - \frac{1}{r}\frac{\partial w_r}{\partial \theta} &= -2\Omega \end{aligned} \tag{2.63}$$

where w_r and w_θ are the radial and circumferential components of the relative velocity.

The boundary conditions are that for small r, $w_r = Q/(2b\pi r)$ and for $\theta = -\pi/Z$ and $\theta = \pi/Z$ $w_\theta = 0$, where b is the height of the channel and Z is the number of blades.

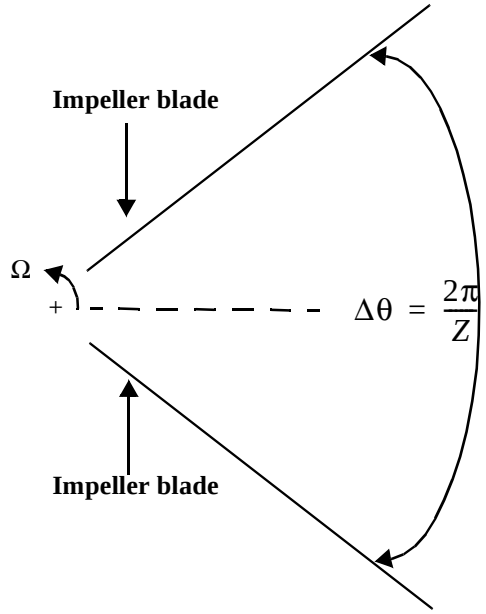

FIGURE 2.1. Geometry of infinitely long straight impeller blades.

stream function

These equations are simplified by introducing a stream function ψ [1], [2]

$$w_r = \frac{1}{r}\frac{\partial \psi}{\partial \theta} \qquad w_\theta = -\frac{\partial \psi}{\partial r} \tag{2.64}$$

The physical meaning of the stream function is that it is constant along streamlines.
By substituting these equation into (2.63), it follows that the first of (2.63) is automatically satisfied (that is exactly the advantage of introducing a stream function!), while the second of (2.63) becomes

$$\frac{\partial^2 \psi}{\partial r^2} + \frac{1}{r}\frac{\partial \psi}{\partial r} + \frac{1}{r^2}\frac{\partial^2 \psi}{\partial \theta^2} = 2\Omega \tag{2.65}$$

Since ψ is a stream function the boundary conditions at the impeller blades become $\psi = -Q/(2bZ)$ at $\theta = -\pi/Z$ and $\psi = Q/(2bZ)$ at $\theta = \pi/Z$. Note that only the difference in value of the stream function is important.
It follows from the physical meaning of the stream function that the difference between the value of the stream function at two stations equals the flowrate through any curve connecting these stations.
It is easily verified that for the case of a large number of impeller blades ($Z \gg 1$) the first two terms of (2.65) can be neglected. The corresponding solution for the stream function and the corresponding velocities is given by

$$\psi = \Omega r^2\left[\theta^2 - \left(\frac{\pi}{Z}\right)^2\right] + \frac{Q\theta}{2\pi b}$$
$$w_r = 2\Omega r\theta + \frac{Q}{2\pi b r} \qquad w_\theta = -2\Omega r\left[\theta^2 - \left(\frac{\pi}{Z}\right)^2\right] \tag{2.66}$$

counter-vortex

The expression for radial velocity w_r is a combination of a term increasing linearly with angle and a uniform flow corresponding to the flowrate. The first term signifies the *counter vortex*. It corresponds to a vortex that rotates in the direction opposite to the impeller

rotation. Therefore the radial velocity is *not* uniform from pressure side to suction side of the blades, contrary to what is assumed in the basic, one-dimensional theory of turbomachinery flow that is described in the course “Fluid Mechanics of Turbomachines I”.
In the case studied here the radial velocity equals the through-flow (or meridional) velocity. Hence, the throughflow velocity it is not uniform from blade to blade: the through-flow velocity is higher at the suction side than at the pressure side. An example of the relative velocity field (2.66) is shown in Figure 2.2.
This pattern for the through-flow velocity has been obtained for the simple case of straight blades, but it holds qualitatively in general for irrotational flow in rotating channels.

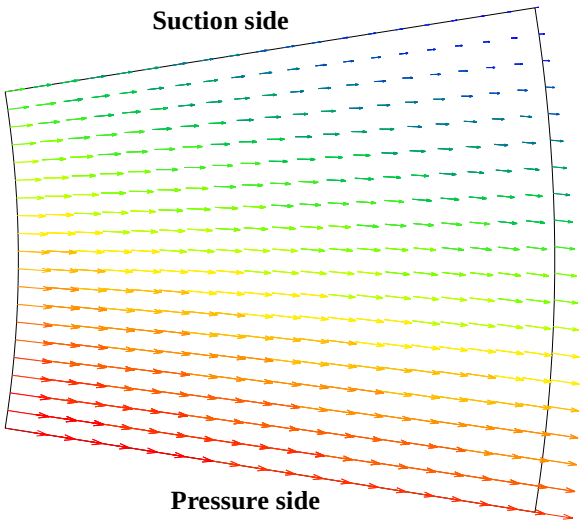

FIGURE 2.2. **Relative velocity field: counter vortex.**

CHAPTER 3

Circulation and wakes

In this chapter it will be shown how circulation can be incorporated into the potential-flow model by introducing *slit lines* (for two-dimensional problems) or *slit surfaces* (for three-dimensional problems). In aerodynamics circulation is directly related to the lift of an airfoil, while for turbomachinery circulation is related to the work input. The conditions that are valid on these slits depend on the nature of the problem (steady or unsteady; two-dimensional or three-dimensional).

Circulation in potential flows

It is well known ([1], §6.7) that the lift force L (per unit span) acting on an airfoil is closely related to the presence of circulation around this body

$$L = \rho U \Gamma \tag{3.1}$$

where U is the velocity of the airfoil.
The equivalent of a lift force acting on an airfoil is a moment acting on a blade of a turbomachine. In the course "Fluid Mechanics of Turbomachines I" it was shown that, for pumps without pre-rotation at the inlet, the specific work input W is given by the Euler relation

$$W = \Omega r_2 c_{\theta 2} \tag{3.2}$$

where the subscript 2 denotes conditions at the trailing edge. The circulation Γ_{pump} for a circular contour just beyond the trailing edge is $2\pi r_2 c_{\theta 2}$, using the one-dimensional flow model adopted in course "Fluid Mechanics of Turbomachines I". Hence the circulation is directly related to the work input.
With the flow model as described so far, it is not possible to predict lift forces, since it gives zero circulation. This can be seen the definition of circulation and the relation for the velocity potential (2.36)

$$\Gamma(C) = \oint_C \nabla\phi \cdot d\underline{s} = \oint_C \frac{\partial \phi}{\partial s} \cdot ds = \oint_C d\phi = \phi_{\text{end}} - \phi_{\text{start}} = 0 \tag{3.3}$$

slit line

if the potential ϕ is *continuous*. By letting the potential be *discontinuous* over a line, circulation can be introduced. The line over which this discontinuity occurs is called a *slit line*. A slit line is also called a cut (in the domain).
This idea is illustrated in Figure 3.1 in which an airfoil is depicted. A slit line is shown emanating from the airfoil to the outer boundary of the domain of interest. In order to identify the two sides of the slit line, they are denoted by a '+' and a '–'. Since the position of the slit line is artificial (and arbitrary), the velocity must be continuous over the slit line. Note that if the velocity is continuous over the slit line, then the pressure is also continuous over the slit line, as follows from (2.52). Now it follows the continuity of the

velocity vector over the slit line and from the expression (2.43) for the velocity in terms of the velocity potential ϕ that

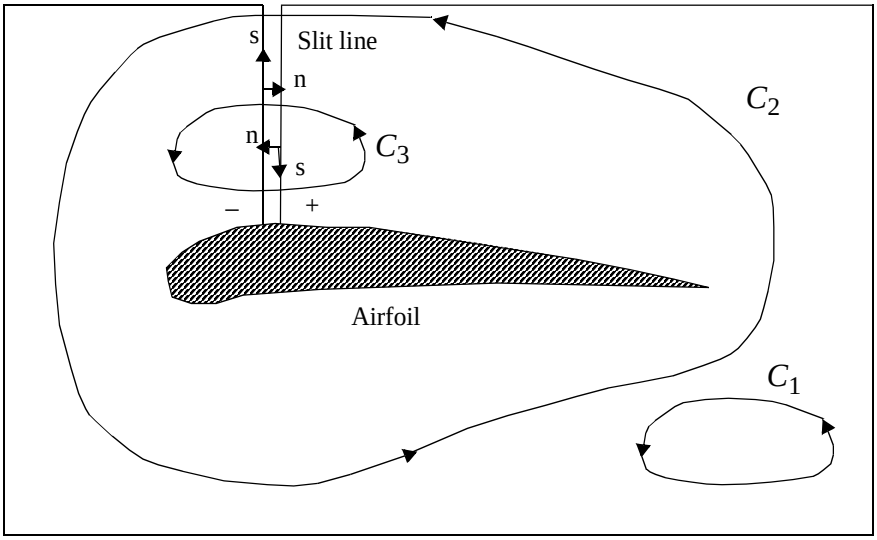

FIGURE 3.1. Airfoil geometry with slit line.

$$\left.\frac{\partial \phi}{\partial n}\right|_{+} = -\left.\frac{\partial \phi}{\partial n}\right|_{-} \qquad \left.\frac{\partial \phi}{\partial s}\right|_{+} = -\left.\frac{\partial \phi}{\partial s}\right|_{-} \tag{3.4}$$

where n denotes the outward normal direction and s denotes the counter-clockwise tangential direction. The minus sign is present since the normal and tangential directions are opposite on the '+' and '–' sides.

The so-called jump relation for the potential along the cut follows from the second equation of (3.4) by integration in s-direction

$$\phi^{+}(s) - \phi^{-}(s) = \text{constant} \tag{3.5}$$

The circulation around a closed contour C_1 that does not cross the slit line equals zero, while the circulation around a closed contour C_2 that does cross the slit line equals $\phi^{+}(s) - \phi^{-}(s)$. This means that the jump over the slit line equals the circulation around the airfoil! The reader is advised to check that the circulation around the contour C_3, that crosses the slit line twice, equals zero.

Kutta condition

Kutta condition

By introducing the slit line it has become possible to introduce circulation around the airfoil into the potential-flow model. The problem then arises of how to determine the unknown value of the circulation. For any value of the circulation, a flow field can, in principle, be determined. Each of these flow fields will be different. The condition that determines the actual value of the circulation is the so-called *Kutta condition* (or Joukowski condition) [1].

Observations have shown that wedge-shaped or cusp-shaped trailing edges have a large influence on the overall flow behaviour. The Kutta-Joukowski hypothesis, or Kutta

hypothesis for short, states that the rear dividing streamline leaves the airfoil at the trailing edge.

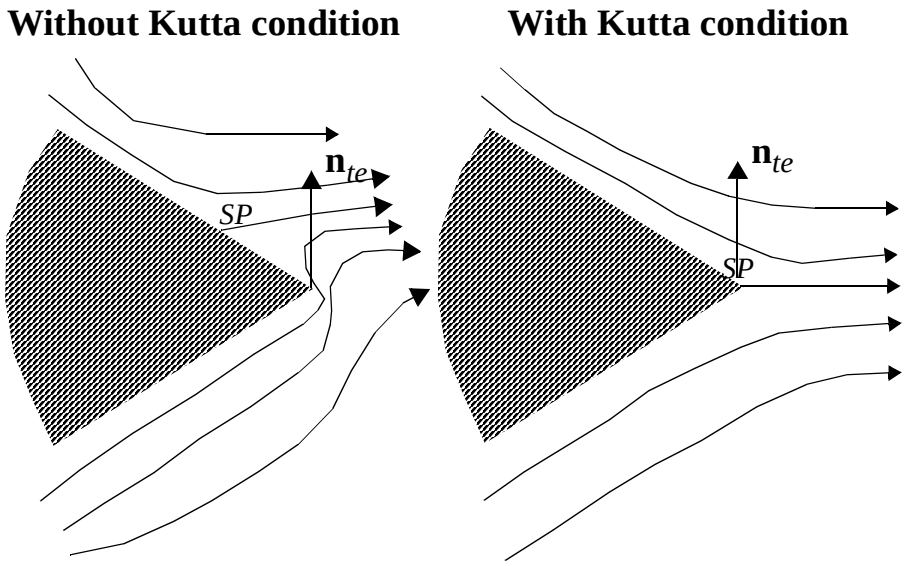

FIGURE 3.2. Flow near the trailing edge of an airfoil, without and with Kutta condition.

To make this plausible the flow is considered near the trailing edge as shown in Figure 3.2a. In this figure the stagnation point (*SP*) is located on the upper side of the airfoil. Consider the streamline that starts near the lower surface of the airfoil. Near the trailing edge the streamline changes direction abruptly and it continues in the direction of the stagnation point where the pressure is maximum. This deceleration and change of direction must be caused by a large pressure-gradient with low pressure near the trailing edge and high pressure near the stagnation point. It is expected that such an adverse pressure-gradient will lead to boundary-layer separation, until the separation point is located at the end point of the trailing edge and the flow is as depicted in Figure 3.2b. In this situation the rear dividing streamline leaves the airfoil at the trailing edge. The Kutta condition requires that the flow leaves "smoothly" from the trailing edge (*te*) of the airfoil.

The Kutta condition can be formulated mathematically in many ways. Here it is formulated by

Kutta condition

$$(\underline{v} \cdot \underline{n})\big|_{te} = 0\,, \tag{3.6}$$

where $\underline{n}$ is the normal vector at the trailing edge of the airfoil.

As has been sketched, the Kutta condition is related to boundary-layer separation that would occur if the Kutta condition were violated. This means that the Kutta condition is closely related to viscous phenomena: in a way the Kutta condition describes a viscous effect within an inviscid theory.

Unsteady case

From Kelvin's circulation theorem it follows that a change in the circulation around an airfoil must result in the shedding of vorticity from the airfoil. This time-dependent vortex shedding results in a wake behind the trailing edge. The vorticity shed is equal in

magnitude to the bound vorticity, but of opposite sign. The vortices in the wake move away from the airfoil.
Since the pressure and normal velocity are continuous across the wake, it follows from the unsteady Bernoulli equation that

$$\frac{\partial}{\partial t}(\phi^+ - \phi^-) + \frac{1}{2}(|\nabla\phi^+|^2 - |\nabla\phi^-|^2) = 0 \qquad (3.7)$$

After linearisation we obtain

$$\frac{\partial}{\partial t}(\phi^+ - \phi^-) + U_s\frac{\partial}{\partial s}(\phi^+ - \phi^-) = 0 \qquad (3.8)$$

where s is the coordinate along the wake and U_s is the mean velocity along the wake. This means that vortices shed the trailing edge are convected downstream with the mean velocity along the wake. This equation describes the evolution with time of the jump distribution on the wake.
Note that in the unsteady case the tangential velocity will not be continuous: the jump in tangential velocity is equal to $\partial(\phi^+ - \phi^-)/\partial s$, as follows from the definition of potential (2.43), which is not zero in unsteady flow according to (3.8).

Three-dimensional case

slit surface

In the three-dimensional case the circulation will in general vary along the span of the trailing edge. The wake behind the trailing edge, see Figure 3.3, will now be represented by a *slit surface.* The distribution of the jumps (discontinuities) in the potential on wake surfaces is given by

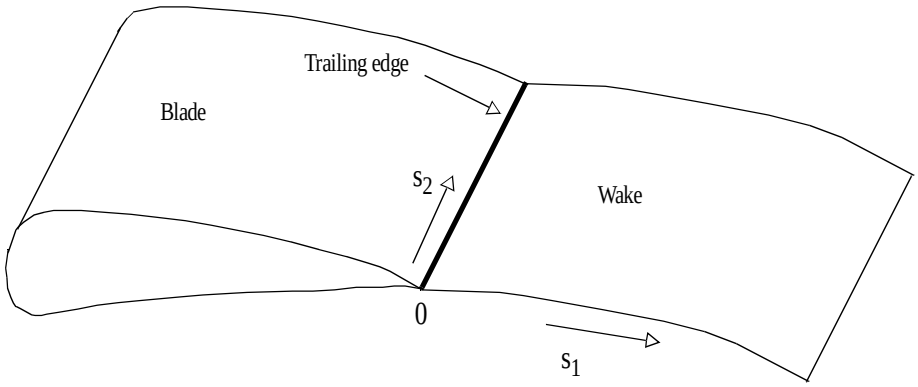

FIGURE 3.3. Representation of a wake behind a blade. Coordinate s_1 is in streamwise direction.

$$\phi^+(s_1, s_2) = \phi^-(s_1, s_2) + \gamma(s_1, s_2) \qquad (3.9)$$

where '+' and '–' denote the upper and lower sides of the wake, s_1 and s_2 are coordinates along the wake (s_1 is in streamwise direction) and $\gamma(s_1, s_2)$ is the potential jump distribution. The blade circulation $\Gamma(s_2)$ at spanwise station s_2 is related to the potential jump distribution by

$$\Gamma(s_2) = \gamma(0, s_2) \qquad (3.10)$$

CHAPTER 4

Potential flows in pumps

This chapter deals firstly with potential-flow computations of the flow in an impeller channel without volute. The superposition method that is used to enforce the Kutta condition is explained in detail.

This is followed by a brief exposition of an (exact) analytical solution that was developed for the two-dimensional potential-flow field in impeller channels formed by logarithmic blades.

Finally, the emphasis is on some aspects of potential-flow computations that are different for pumps in comparison to airfoils.

Superposition method

free impeller case

In this section the method is described that can be used to solve the potential-flow problem in turbomachines. For simplicity the “free impeller” case, where there is no influence of the stationary parts on the rotating parts (volute or diffusor), is discussed. In this (idealised) case the influence of the volute on the flow field in the impeller channels is negligible. Then only the flow in a single impeller channel needs to be considered, because of the symmetry of the impeller flow channels. The geometry of the channel is shown in Figure 4.1.

The boundary conditions that apply to this channel are given in Table 1. These boundary conditions are

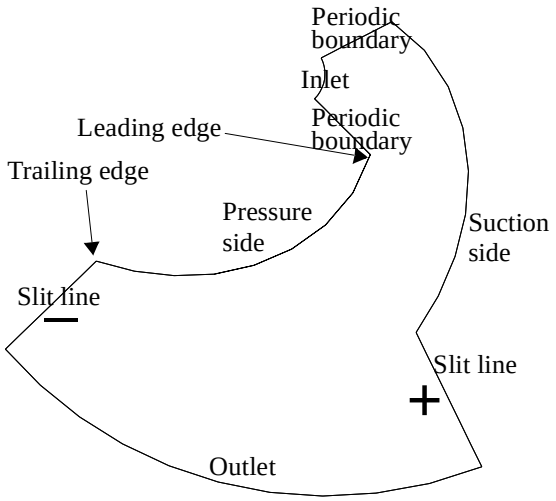

FIGURE 4.1. Geometry of impeller channel.

- Inlet: Uniform inflow at a velocity that is determined from the flowrate Q; this is an *assumption* that is valid "far away" from the leading edge of the impeller;
- Outlet: Uniform inflow at a velocity that is determined from the flowrate Q; this is an *assumption* that is valid "far away" from the trailing edge of the impeller;
- Impeller blades: the blades are impermeable, so the normal component of *relative* velocity equals zero;

periodic boundary conditions

- "Periodic" boundaries and slit lines: the velocities are "periodic" on the two surfaces ('+' and '–' sides). This means that the normal velocity and the tangential velocity on corresponding points on the two surfaces are equal

$$\left.\frac{\partial\phi}{\partial n}\right|_{+} = -\left.\frac{\partial\phi}{\partial n}\right|_{-} \qquad \left.\frac{\partial\phi}{\partial s}\right|_{+} = -\left.\frac{\partial\phi}{\partial s}\right|_{-} \tag{4.1}$$

The second of these implies

$$\phi|_{+} - \phi|_{-} = \text{constant} \tag{4.2}$$

On the periodic boundary near the leading edge this constant equals zero for inflow without pre-rotation (check this by considering a contour around the rotation axis!), while on the periodic boundary near the trailing edge this constant equals the (unknown) circulation around a blade.

- A so-called essential boundary condition (prescribed value for the potential) in a point is required to fix the level of the potential; otherwise if ϕ were a solution, then ϕ + constant would also be a solution (i.e. the solution is not unique).

Note that in the potential-flow model, like with the Euler equations, the "stick" condition of (relative) zero velocity can not be enforced on the impeller blades: only the impermeability condition can be prescribed!

The flowrate Q and the rotation rate Ω are given as process parameters, but the circulation around the impeller blades is not yet known. Its value has to be determined from the Kutta condition. As discussed before, the Kutta condition requires that the flow leaves "smoothly" from the trailing edge of the impeller blades. For a rotating trailing edge the Kutta condition is

$$\underline{w} \cdot \underline{n}\big|_{te} = 0 \tag{4.3}$$

where the relative velocity $\underline{w}$ is defined by

$$\underline{v} = \underline{w} + \underline{\Omega} \times \underline{r} \tag{4.4}$$

From these equations it follows that in a rotating system the Kutta condition can be formulated as

$$\left.\frac{\partial\phi}{\partial n}\right|_{te} = (\underline{\Omega} \times \underline{r}) \cdot \underline{n}\big|_{te} \tag{4.5}$$

The governing Laplace equation (2.51) for potential flow can not be solved directly, since the boundary conditions contain the unknown value for the circulation.

superposition principle; subpotentials

The method to be used to determine the unknown circulation is based on the superposition principle, which can be employed since the governing Laplace equation (2.51) is *linear*. Here three subpotentials are distinguished: a unit subpotential corresponding to the through-flow (flow subpotential ϕ^Q), a unit subpotential corresponding to the rotation of the impeller blades (rotation subpotential ϕ^Ω) and a unit subpotential corresponding to the circulation around an impeller blade (circulation subpotential ϕ^Γ). The complete solution ϕ can be expressed in terms of the three subpotentials as

$$\phi = \frac{Q}{Q=1}\phi^{Q} + \frac{\Omega}{\Omega=1}\phi^{\Omega} + \frac{\Gamma}{\Gamma=1}\phi^{\Gamma} \tag{4.6}$$

Terms like $Q = 1$ in the denominator have been added for dimensional consistency.
The boundary conditions for the complete solution and the three subpotentials are given in Table 1. It is easily verified that the superposition in (4.6) satisfies all boundary conditions for the complete solution. Note that the three subpotentials are unit potentials: for example the flow subpotential corresponds to $Q = 1$, $\Omega = 0$ and $\Gamma = 0$.
The three subpotentials can be determined with the boundary conditions listed in Table 1. From these three subpotentials the velocity at the trailing edge can also be determined. Then the unknown circulation can be computed from

$$\frac{Q}{Q=1}\frac{\partial\phi^{Q}}{\partial n}\bigg|_{te} + \frac{\Omega}{\Omega=1}\frac{\partial\phi^{\Omega}}{\partial n}\bigg|_{te} + \frac{\Gamma}{\Gamma=1}\frac{\partial\phi^{\Gamma}}{\partial n}\bigg|_{te} = (\underline{\Omega}\times\underline{r})\cdot\underline{n}\big|_{te} \tag{4.7}$$

With the value of the circulation thus determined, the complete solution can be computed since all parameters in the boundary conditions are now known.
Summarizing, with the known boundary conditions the three subpotentials can be computed. Then the Kutta condition gives the value for the unknown circulation. This value of the circulation, which is unknown at start, is present in the boundary conditions. Finally, the complete solution can be computed. This solution gives the pressure and velocity field in the impeller channel.

TABLE 1. Boundary conditions for the complete solution and for the three subpotentials for a free impeller computation.

	Complete solution	Subpotentials		
		Flow	Rotation	Circulation
Inlet	$\frac{\partial\phi}{\partial n} = \frac{-Q}{A_{\text{inlet}}}$	$\frac{\partial\phi}{\partial n} = \frac{-1}{A_{\text{inlet}}}$	$\frac{\partial\phi}{\partial n} = 0$	$\frac{\partial\phi}{\partial n} = 0$
Outlet	$\frac{\partial\phi}{\partial n} = \frac{Q}{A_{\text{outlet}}}$	$\frac{\partial\phi}{\partial n} = \frac{1}{A_{\text{outlet}}}$	$\frac{\partial\phi}{\partial n} = 0$	$\frac{\partial\phi}{\partial n} = 0$
Impeller blades	$\frac{\partial\phi}{\partial n} = \Omega\left(\begin{bmatrix}0\\0\\1\end{bmatrix}\times\underline{r}\right)\cdot\underline{n}$	$\frac{\partial\phi}{\partial n} = 0$	$\frac{\partial\phi}{\partial n} = \left(\begin{bmatrix}0\\0\\1\end{bmatrix}\times\underline{r}\right)\cdot\underline{n}$	$\frac{\partial\phi}{\partial n} = 0$
"Periodic" boundaries	$\phi\big\|_{+} - \phi\big\|_{-} = 0$ $\frac{\partial\phi}{\partial n}\big\|_{+} = -\frac{\partial\phi}{\partial n}\big\|_{-}$	$\phi\big\|_{+} - \phi\big\|_{-} = 0$ $\frac{\partial\phi}{\partial n}\big\|_{+} = -\frac{\partial\phi}{\partial n}\big\|_{-}$	$\phi\big\|_{+} - \phi\big\|_{-} = 0$ $\frac{\partial\phi}{\partial n}\big\|_{+} = -\frac{\partial\phi}{\partial n}\big\|_{-}$	$\phi\big\|_{+} - \phi\big\|_{-} = 0$ $\frac{\partial\phi}{\partial n}\big\|_{+} = -\frac{\partial\phi}{\partial n}\big\|_{-}$
Slit line	$\phi\big\|_{+} - \phi\big\|_{-} = \Gamma$ $\frac{\partial\phi}{\partial n}\big\|_{+} = -\frac{\partial\phi}{\partial n}\big\|_{-}$	$\phi\big\|_{+} - \phi\big\|_{-} = 0$ $\frac{\partial\phi}{\partial n}\big\|_{+} = -\frac{\partial\phi}{\partial n}\big\|_{-}$	$\phi\big\|_{+} - \phi\big\|_{-} = 0$ $\frac{\partial\phi}{\partial n}\big\|_{+} = -\frac{\partial\phi}{\partial n}\big\|_{-}$	$\phi\big\|_{+} - \phi\big\|_{-} = 1$ $\frac{\partial\phi}{\partial n}\big\|_{+} = -\frac{\partial\phi}{\partial n}\big\|_{-}$
Essential point P	$\phi = 0$ in P	$\phi = 0$ in P	$\phi = 0$ in P	$\phi = 0$ in P

Relation between process parameters and circulation

For the free-impeller case the relation between process parameters flowrate Q, angular velocity Ω and head H will be investigated. The starting point is the angular-momen-

tum principle as discussed in the course “Fluid Mechanics of Turbomachines I” (but see also [1]). In integral form this principle states

$$M = \int_{CS} r v_\theta \rho (\underline{v} \cdot \underline{n}) dA \tag{4.8}$$

where M is the torque exerted on the control volume by the axis and CS is the control surface enclosing the control volume under consideration. Note that in this formulation of the angular-momentum principle surface forces have been neglected and steady conditions are considered (this latter assumption is actually not necessary: what we are actually considering is the torque averaged over a revolution, and then time-averages cancel out).

With the condition of uniform inflow and uniform outflow that is applicable to the free-impeller case, we have $\underline{v} \cdot \underline{n} = \pm Q/A$ (independent of position at inflow and outflow surfaces). Hence, using the fact that ρ is constant, the expression for the torque becomes

$$M = \frac{\rho Q}{A} \left[\int_{CS,out} r v_\theta dA - \int_{CS,in} r v_\theta dA \right] \tag{4.9}$$

where CS,out and CS,in are the outlet and inlet regions of the control surface. For cases without inlet-swirl, $v_\theta = 0$, and with two-dimensional outlet surfaces this becomes

$$M = \rho Q r_{out} \overline{v_\theta} \tag{4.10}$$

where $\overline{v_\theta}$ is the average tangential velocity at the outlet and r_{out} is the radius at the outlet. For circular outlet surfaces this average tangential velocity at the outlet is related to the circulation Γ_{imp} around the impeller by $\Gamma_{imp} = 2\pi r_{out} \overline{v_\theta}$, as follows from the definition of circulation (2.36). The circulation around the impeller Γ_{imp} is related to the circulation around a single blade Γ by $\Gamma_{imp} = Z\Gamma$ where Z is the number of blades. The torque M now is given by

$$M = \frac{\rho Q Z \Gamma}{2\pi} \tag{4.11}$$

The power transferred from the pump axis to the fluid, P_{in}, is given by $P_{in} = \Omega M$. The net power that is transferred to the fluid as pressure rise, P_{out} is given by $P_{out} = \rho Q g H$. Assuming the efficiency is 100%, $P_{out} = P_{in}$, we find the relation between circulation around the blade and head

$$gH = \frac{Z \Omega \Gamma}{2\pi} \tag{4.12}$$

Note that this relation is only valid for two-dimensional free-impeller cases!

Potential flow in logarithmic channels

The special case of potential flow in the channels of a two-dimensional impeller consisting of Z logarithmic blades with constant blade angle β has been studied in detail [33]. Process parameters of the flow are the flowrate Q and the rotation rate of the impeller Ω. The two-dimensional velocity and pressure field corresponding to potential flow in the impeller channels were studied analytically, using the method of conformal mapping and asymptotic expansions. This section summarizes their main results for the case that the inlet flow has no pre-rotation.

The geometry of logarithmic blades will first be described. Then the results for the head and the condition of “shock-free” approach according to one-dimensional theory (as discussed in the course “Fluid Mechanics of Turbomachines I”) and according to the two-dimensional theory of [33] will be given.

Contrary to the two-dimensional theory, the one-dimensional theory does not account for the non-uniformity in the flow field that is caused by the presence of the counter vortex, as discussed on page 13. The results of the two-dimensional theory show the nature of the required corrections, but it is only valid for the simple geometry of logarithmic blades: it does not apply to more general, realistic blade geometries. The results of the two-dimensional theory are also very useful for verifying numerical solutions. Note that only numerical methods are suitable for computing the flow field in general geometries!

Geometry of logarithmic blades

blade angle

The geometry of the flow channel is defined by the radius of the leading edge r_{le}, the radius of the trailing edge r_{te}, the constant blade angle β, the height of the impeller B and the number of blades Z. In the two-dimensional case considered here, the blade angle is the angle between the radial direction and the tangent to the blade (see Figure 4.2). Note that often another convention is used where the blade angle is defined as the angle between circumferential direction and the tangent to the blade.

From Figure 4.2 it follows that

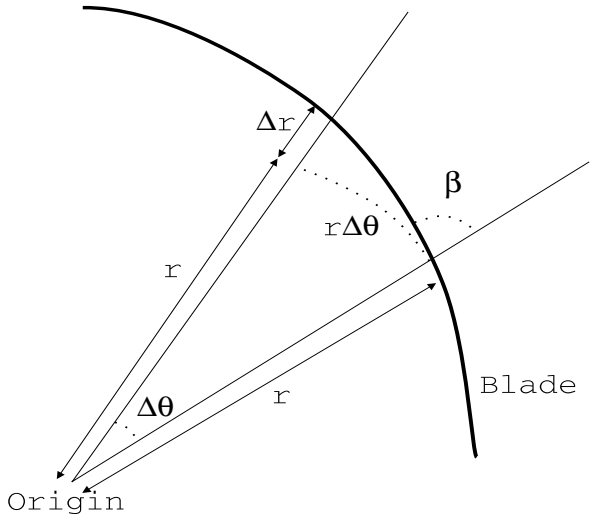

FIGURE 4.2. Definition of blade angle β.

$$r\frac{d\theta}{dr} = \tan\beta \tag{4.13}$$

By integrating this equation (using that β is constant!) with initial condition $\theta = \theta_{le}$ for $r = r_{le}$, we obtain the equation describing the shape of the logarithmic blades

$$\theta = \theta_{le} + \tan\beta \ln\left(\frac{r}{r_{le}}\right) \tag{4.14}$$

Here θ and r are the polar coordinates of a point on the blade, while θ_{le} and r_{le} are the polar coordinates of the leading edge. Note that β is negative for backswept (or backward curved) blades! This means that they are curved in the direction opposite to the direction of rotation of the blades.

One-dimensional theory

The results according to the one-dimensional theory (as discussed in the course “Fluid Mechanics of Turbomachines I”) for the condition of “shock-free” flow and the head imparted to the fluid by the impeller are briefly recapitulated here for the case without pre-rotation. The one-dimensional theory assumes that

$$\frac{w_\theta}{w_r} = \tan\beta \quad w_r = \frac{Q}{2\pi r B} \quad v_\theta\big|_{le} = 0 \tag{4.15}$$

It follows that the head imparted to the fluid by the impeller is given by

$$gH = (\Omega r_{te})^2 + \frac{\tan\beta}{2\pi}\Omega\frac{Q}{B} \tag{4.16}$$

and the condition of “shock-free” approach is given by

$$-\tan\beta = 2\pi r_{le}^2 \Omega\frac{B}{Q} \tag{4.17}$$

Two-dimensional theory

Based on the Laplace equation (2.51) corresponding to potential flow, the method of conformal mapping and asymptotic expansions was used in [33] to obtain, after rather lengthy algebra, the head H that is imparted to the fluid by the impeller according to the two-dimensional theory

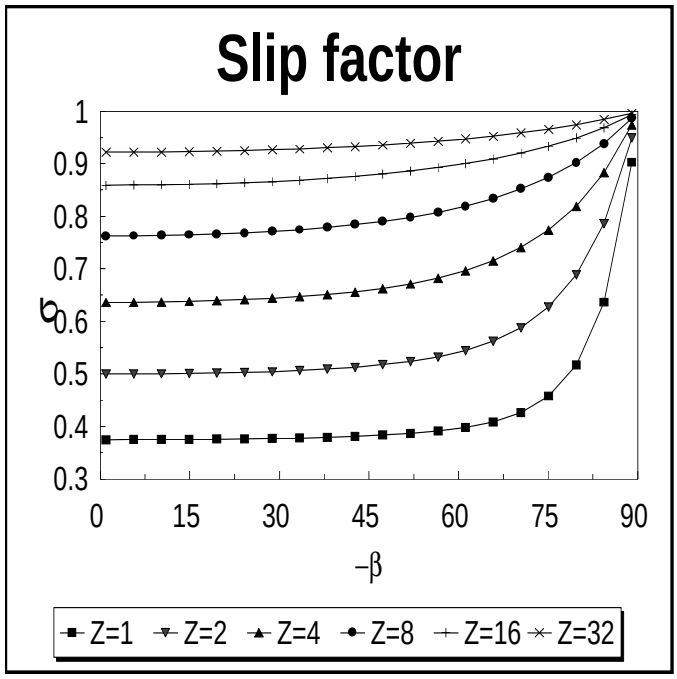

FIGURE 4.3. Slip factor.

$$gH = \sigma(Z, \beta)(\Omega r_{te})^2 + \frac{\tan\beta}{2\pi}\Omega\frac{Q}{B} \tag{4.18}$$

slip factor

The slip factor $\sigma(Z, \beta)$ is plotted in Figure 4.3. Note that this slip factor is not an empirical fit, like the expressions for the slip factor that were given in the course "Fluid Mechanics of Turbomachines I". Equations that can be used to compute the slip factor are given in the Appendix. For free impellers the relation between head H and the circulation Γ around a single impeller blade is given by (4.12). The circulation around the complete impeller is of course $Z\Gamma$.
According to [33] the condition of "shock-free" flow of the impeller is given by

$$-\tan\beta = \tau_\beta(Z, \beta) 2\pi r_{1e}^2 \Omega \frac{B}{Q} \tag{4.19}$$

where the "correction factor" $\tau_\beta(Z, \beta)$ for "shock-free" flow is given approximately by

$$\tau_\beta(Z, \beta) = 1 + (\tau_0(Z) - 1)\cos\beta \tag{4.20}$$

and $\tau_0(Z)$ is given in the Appendix. The function $\tau_0(Z)$ is plotted in Figure 4.4.

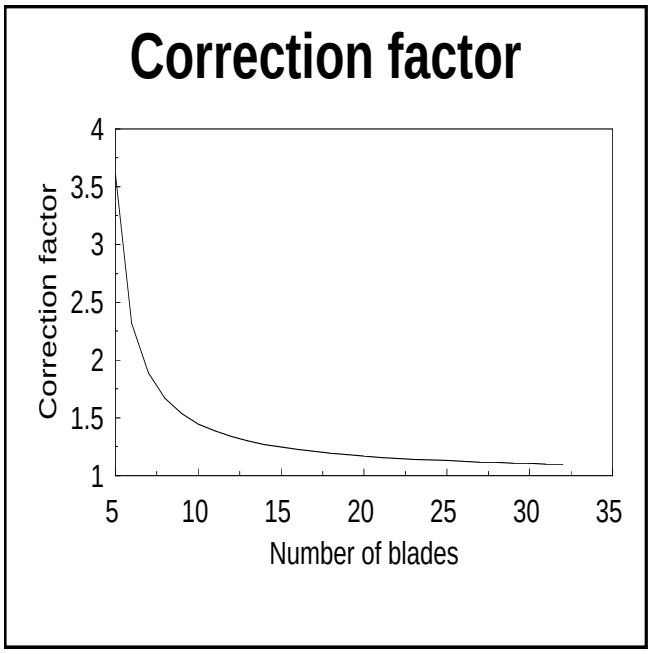

FIGURE 4.4. "Correction factor" for "shock-free" approach for straight-bladed impellers.

Potential flow in complete pumps

Special complications arise when computing potential flows in complete pump configurations. One complication is that the flow is time-dependent, due to the presence of rotating and stationary parts. Only in the design point (best efficiency point) can one expect that time-dependent phenomena are not very significant.

rotor-stator interface; sliding surface

The presence of rotating and stationary parts creates additional problems with mesh generation, since the computational domain changes continuously due to the movement of the blades. One attractive solution is to have separate meshes for the rotating part and the stationary part. By rotating the mesh for the rotor the topology of this mesh remains

intact. Of course, interface over which the meshes "slide" must be a conical surface, see also Figure 4.5. This artificial rotor-stator interface is called the "sliding surface" (not to be confused with the "*slit* surfaces" where a jump, i.e. a discontinuity, in the potential is present). As discussed in Chapter 3 the slit surfaces were introduced to account for circulation, while the sliding surfaces are introduced for computational efficiency.

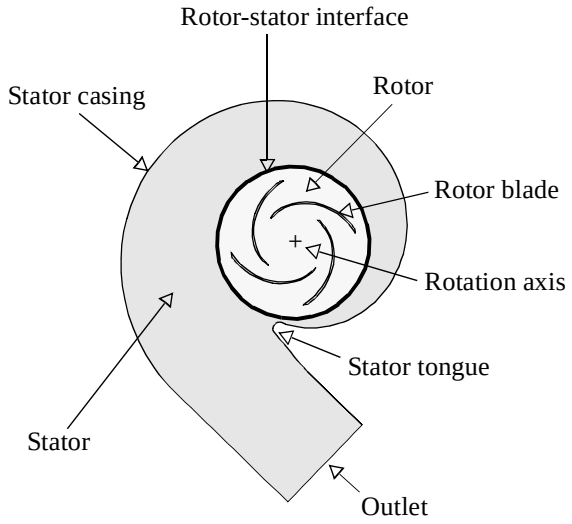

FIGURE 4.5. Rotor-stator interface.

Since the wakes behind the trailing edges of the rotor are expected to move with the rotor, the slit lines or slit surfaces must be part of the mesh for the rotor. Therefore the mesh for the rotor must be large enough to capture sufficient detail of the wakes, but on the other hand it may not exceed the stator wall. A compromise between these has to be made.

Since the wakes are located in the rotor part (and not in the stator part), the jumps at the rotor-stator interface must become constant over the height. This means that some sort of smoothing has to be applied to the jump distribution on the wake. If this were not done, than the velocity at the rotor-stator interface, which is a non-physical, computational feature, would not be continuous.

Appendix: slip factor

The slip factor $\sigma(Z, \beta)$ can be computed using complex numbers. The equation for $\sigma(Z, \beta)$ is

$$\sigma(Z, \beta) = \frac{e^{-2\frac{\beta \sin 2\beta}{Z}}}{\left(1 + 4\frac{\cos^2\beta}{Z}\right)(2\cos\beta)^{4\frac{\cos^2\beta}{Z}} B(\delta(Z, \beta), \overline{\delta(Z, \beta)})} \tag{4.21}$$

where $\bar{w}$ denotes the conjugate of a complex number w and the Beta-function $B(x, y)$ [11] is defined by

$$B(x, y) = \frac{\Gamma(x)\Gamma(y)}{\Gamma(x + y)} \tag{4.22}$$

and

$$\delta(Z, \beta) = 1 + 2\frac{\cos^2\beta}{Z} + i\frac{\sin 2\beta}{Z} \tag{4.23}$$

where $\Gamma(z)$ denotes the Euler Gamma function [11] (here Γ is not the symbol for circulation!). Note that $B(\delta(Z, \beta), \overline{\delta(Z, \beta)})$ in (4.21) always is a real number!
The "correction factor" $\tau_0(Z)$ for "shock-free" flow of straight blades is given approximately by

$$\tau_0(Z) = 2^{4/Z}\frac{\Gamma(1 - 4/Z)}{\Gamma(1 - 2/Z)^2} \tag{4.24}$$

CHAPTER 5

Numerical method

This chapter describes the numerical method that was developed especially for computations of time-dependent potential flows in pumps with rotating and stationary parts.

Wakes

unsteady computation

The correct description of the evolution of the jump distribution on the wake is given by (3.8). This is used in *unsteady* computations.

quasi-steady computation

In *quasi-steady* simulations the convection of vortices in the wake is neglected, and the potential jump over the wake surface is taken constant in streamwise direction

$$\gamma(s_1, s_2) = \Gamma(s_2) \tag{5.1}$$

Summarising, in quasi-steady computations (without unsteady wakes) the potential jump distribution in the wake is given by (5.1), while in unsteady computations (with unsteady wakes) the potential jump distribution satisfies (3.8).

Boundary conditions

On the *inlet* and *outlet* surfaces of the turbomachine, a uniform normal velocity is prescribed

$$\frac{\partial \phi}{\partial n} = \mp \frac{Q}{A} \tag{5.2}$$

where Q is the flowrate and A is the area of the surface.
At the impermeable *blade surfaces* (both pressure and suction sides), where $w_n = 0$, the Neumann boundary condition takes the form

$$\frac{\partial \phi}{\partial n} = (\underline{\Omega} \times \underline{r}) \cdot \underline{n} \tag{5.3}$$

At the *hub* and the *shroud* of the rotor and at the *stator walls*, the normal velocity vanishes

$$\frac{\partial \phi}{\partial n} = 0 \tag{5.4}$$

Wakes are present behind trailing edges. These wakes are a result of both nonuniform blade loading (variations of the circulation along the blade's span) and time-dependent

variations of the blade circulations. Within the potential-flow model, wakes are modelled by the boundary conditions

$$\begin{aligned} \phi^+(s_1, s_2) &= \phi^-(s_1, s_2) + \gamma(s_1, s_2) \\ \frac{\partial}{\partial n}\phi^+(s_1, s_2) &= -\frac{\partial}{\partial n}\phi^-(s_1, s_2) \end{aligned} \qquad \textbf{(5.5)}$$

The second equation of (5.5) states that the normal velocity is continuous on the wake surface. Note that wakes should coincide with stream surfaces. In general an iterative method is needed to meet this requirement.

Rotor-stator interface

When considering configurations of complete pumps or turbines, special care has to be taken of the presence of both rotating and stationary parts, see also Figure 4.5. In order to achieve this without having to create a new mesh for each time step (as was done in [26]), the rotor and the stator are separated by a cylindrical or conical surface, the so-called rotor-stator interface, or “sliding surface”. “Connections” between nodes at both sides of this interface are changing over time due to the rotation of the rotor. In this way the rotor is allowed to rotate freely while “sliding” along the stator.

Multi-block approach

The presence of a rotor and a stator part with their separate coordinate systems naturally suggests using a multi-block approach. In such a multi-block approach the flow region of interest is divided into subdomains or blocks, all having a topologically cubic shape. The subdomains are non-overlapping, with nodal coincidence at the interfaces. For a free rotor computation one block will usually suffice, although a division into more blocks is possible. However, for a flow computation inside a complete pump or turbine (rotor and stator) a number of blocks is required (see Figure 5.1).
An advantage of the multiblock approach is the greater ease in creating a good mesh for the complex three-dimensional geometries that are considered here. It also constitutes an important component of the numerical method that is described in the next section.
In the multiblock approach additional boundary conditions have to be formulated that apply to the artificial internal boundaries between blocks. The velocity field at these internal boundaries should be continuous. Therefore the values of the potential at corresponding nodes can differ only by a fixed amount and the normal velocities are opposite. This means that the boundary conditions for such internal boundaries are the same as those for wakes (see equation (5.5)), with γ constant. Periodic boundary conditions, as apply for a free rotor computation, are also of this type.

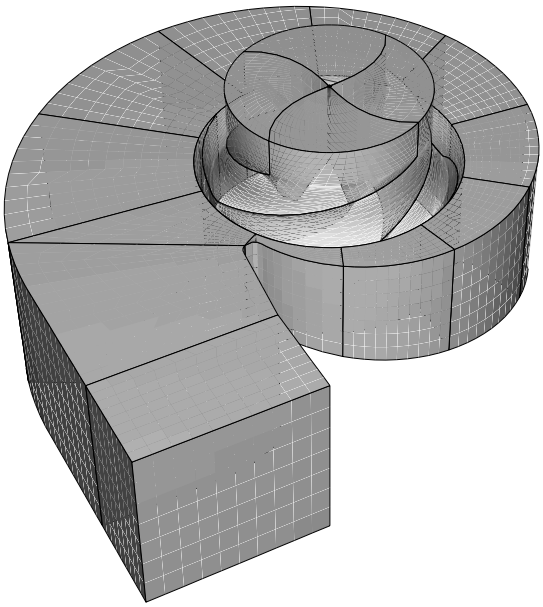

FIGURE 5.1. Example of a pump geometry divided into blocks and cross-section of pump.

Numerical method

Outline

superelement technique; substructuring technique

The flow field is solved by means of a finite element method using an extension of the superelement technique [35]. In the superelement technique (or substructuring technique) internal degrees of freedom (*DOFs* for short) are eliminated from the discretized governing (Laplace) equation. The extension of the superelement method developed deals with an analogous elimination of the internal DOFs from the discretized Kutta conditions. The detailed description of the method is given in [25].

The method consists of two steps:

- elimination of internal DOFs from the system of equations (Laplace equation and Kutta conditions), for all blocks separately. This leads to the formulation of the superelements.
- assemblage of the superelements. After solving the resulting global system of equations, the previously eliminated DOFs are obtained.

Superelement formulation: elimination step

For each block, the Laplace equation for the velocity potential together with the natural and essential boundary conditions (if any) is discretized according to the standard finite-element method, resulting in a system of linear equations

$$[L]\{\phi\} = \{F\} + \{R\} \tag{5.6}$$

where $[L]$ is a positive-definite matrix reflecting the discretized Laplace operator, $\{\phi\}$ is the vector of DOFs and $\{F\}$ is the vector corresponding to flowrates through block boundaries resulting from Neumann type boundary conditions. Vector $\{R\}$ is related to (unknown) flowrates at internal block boundaries.
For each block, the discretized Kutta conditions (equation (4.5)) can be expressed in terms of potential values in the block using the modified gradient operator $[K]$ (K stands for Kutta)

$$[K]\{\phi\} = \{(\underline{\Omega} \times \underline{r}) \cdot \underline{n}|_{te}\} \tag{5.7}$$

Using the values of the potential, operator $[K]$ gives the normal velocities at the trailing edges.
The basic idea of the superelement technique is to express (5.6) and (5.7) in terms of DOFs at internal block boundaries (called the "master" DOFs), by eliminating the remaining interior "slave" DOFs. For this purpose (5.6) and (5.7) are partitioned as follows

$$\begin{bmatrix} [L^{ss}] & [L^{sm}] \\ [L^{ms}] & [L^{mm}] \end{bmatrix} \begin{Bmatrix} \{\phi^s\} \\ \{\phi^m\} \end{Bmatrix} = \begin{Bmatrix} \{F^s\} \\ \{F^m\} + \{R^*\} \end{Bmatrix} \tag{5.8}$$

$$\begin{bmatrix} [K^s] & [K^m] \end{bmatrix} \begin{Bmatrix} \{\phi^s\} \\ \{\phi^m\} \end{Bmatrix} = \{(\underline{\Omega} \times \underline{r}) \cdot \underline{n}|_{te}\} \tag{5.9}$$

Superscripts s and m denote "slaves" and "masters" respectively. Vector $\{R^*\}$ denotes the non-zero part of vector $\{R\}$ in (5.6).
By solving for the slave DOFs from (5.8), it follows that

$$\{\phi^s\} = \left[L^{ss}\right]^{-1}\{F^s\} - \left[L^{ss}\right]^{-1}\left[L^{sm}\right]\{\phi^m\} \tag{5.10}$$

The resulting "super system", formulated exclusively in terms of the "master" DOFs, is obtained after substituting (5.10) into (5.8) and (5.9)

$$\begin{aligned} \left[L^{\text{sup}}\right]\{\phi^m\} &= \{F^{\text{sup}}\} + \{R^*\} \\ \left[K^{\text{sup}}\right]\{\phi^m\} &= \{G^{\text{sup}}\} \end{aligned} \tag{5.11}$$

where

$$\begin{aligned} [L^{\text{sup}}] &= [L^{mm}] - [L^{ms}][L^{ss}]^{-1}[L^{sm}] \\ [K^{\text{sup}}] &= [K^m] - [K^s][L^{ss}]^{-1}[L^{sm}] \end{aligned} \tag{5.12}$$

$$\begin{aligned} \{F^{\text{sup}}\} &= \{F^m\} - [L^{ms}][L^{ss}]^{-1}\{F^s\} \\ \{G^{\text{sup}}\} &= \{(\underline{\Omega} \times \underline{r}) \cdot \underline{n}|_{te}\} - [K^s][L^{ss}]^{-1}\{F^s\} \end{aligned} \tag{5.13}$$

Note that column i of $-[L^{ms}][L^{ss}]^{-1}$ in (5.12) can be interpreted as the values of the "slave" potentials corresponding to master DOF i equal to 1 and all other "master" DOFs equal to zero. Similarly, the term $[L^{ss}]^{-1}\{F^s\}$ in (5.13) represents the effect of Neumann boundary conditions on "slave" DOFs, while keeping the "master" DOFs equal to zero. Note that these potentials can be computed by simple backsubstitutions once the matrix $[L^{ss}]$ has been decomposed.

This section describes how the reduced set of equations is obtained, in terms of DOFs at block interfaces only. In principle this procedure must be carried out for all blocks that form the entire geometry. However, an important observation is that the supermatrices and vectors are invariant under rotation for the scalar equations considered. Therefore the symmetry of the rotor can be exploited, as in general all rotor channels are geometrically identical. This means that the superelement formulation step has to be performed for the block(s) of a single rotor channel only! Furthermore, in a time-dependent computation, the superelement formulation step has to be carried out only once.
The assemblage of blocks, which can be regarded as superelements, is part of the second step. This is described in the following subsection.

Assemblage of superelements: global solution step

In the global solution step, the values of "master" DOFs of all participating blocks are determined by assembling and solving the global system of equations.
A complicating factor in the computation of the "master" DOFs is the fact that blade circulations and, as a consequence, the potential jumps at nodes on the wakes are still unknown. Therefore the values of blade circulations are regarded as additional variables to be determined along with the nodal DOFs (see also [12]). The vector of unknowns in the global problem is now denoted by

$$\{u\}^T = \{\phi_1, ...,\phi_{n_\Phi}, \Gamma_1, ...,\Gamma_{n_\Gamma}\} = \{\{\Phi\}^T\{\Gamma\}^T\} \tag{5.14}$$

where n_Φ is the number of nodes in all block connections (coinciding nodes are counted as one), n_Γ is the number of unknown blade circulations (i.e. the total number of nodes at trailing edges), $\{\Phi\}$ is the vector of unknown "master" DOFs for the potential and $\{\Gamma\}$ is the vector of unknown blade circulations.
The "master" DOFs can now be expressed in terms of global DOFs. Note that master DOFs may also involve potential jumps, see (5.5). These jumps are composed of known and unknown potential jumps (see also the appendix).
All "master" DOFs of block *b* are now written formally as

$$\{\phi_b^m\} = [T_b^\Phi]\{\Phi\} + [W_b]\{\Gamma\} + \{\gamma_b\} \tag{5.15}$$

where

- $[T_b^\Phi]$ = matrix which gives the transformation of global equation numbers of nodal DOFs to the local numbering of "master" DOFs in block *b*. Each row contains exactly one nonzero coefficient, having the value 1.
- $[W_b]$ = matrix which gives the equation numbers of global blade circulation DOFs for the "masters" of block *b*. It also accounts for the "averaging" of potential jumps on the wakes (see the appendix).
- $\{\gamma_b\}$ = known values of potential jumps at boundaries of block *b*. These jumps are present in computations including unsteady wakes (see the appendix).

Similar to the way in which element matrices and right-hand side vectors are assembled to form the large system of equations, the superelement matrices and right-hand side vectors of (5.11) are assembled into a global system of equations for the Laplace equation and for the Kutta conditions

$$\begin{aligned}
\sum_{b=1}^{b} [T_b^\Phi]^T [L_b^{\sup}]\{\phi_b^m\} &= \sum_{b=1}^{b} [T_b^\Phi]^T \{F_b^{\sup}\} \\
\sum^{n_b} [T_b^\Gamma]^T [K_b^{\sup}]\{\phi_b^m\} &= \sum^{n_b} \left[T_b^\Gamma\right]^T \{G_b^{\sup}\}
\end{aligned} \tag{5.16}$$

where matrices $[T_b^\Gamma]$ account for the transformation of the global blade circulation DOFs to the equation numbers of the local numbering of trailing edge nodes and n_b is the total number of participating blocks. Note that the contribution of the vectors $\{R_b^*\}$ in (5.11) cancel out at internal block boundaries.

Substituting $\{\phi_b^m\}$ from (5.15) into (5.16) gives the global system of equations

$$\begin{bmatrix} [M^{\Phi\Phi}] & [M^{\Phi\Gamma}] \\ [M^{\Gamma\Phi}] & [M^{\Gamma\Gamma}] \end{bmatrix} \begin{Bmatrix} \{\Phi\} \\ \{\Gamma\} \end{Bmatrix} = \begin{Bmatrix} \{H^\Phi\} \\ \{H^\Gamma\} \end{Bmatrix} \tag{5.17}$$

where

$$\begin{aligned} [M^{\Phi\Phi}] &= \sum_{b=1}^{n_b} [T_b^\Phi]^T [L_b^{\sup}][T_b^\Phi] \qquad [M^{\Phi\Gamma}] = \sum_{b=1}^{n_b} [T_b^\Phi]^T [L_b^{\sup}][W_b] \\ \left[M^{\Gamma\Phi}\right] &= \sum^{n_b} [T_b^\Gamma]^T [K_b^{\sup}][T_b^\Phi] \qquad \left[M^{\Gamma\Gamma}\right] = \sum^{n_b} [T_b^\Gamma]^T [K_b^{\sup}][W_b] \end{aligned} \tag{5.18}$$

$$\begin{aligned} \{H^\Phi\} &= \sum_{b=1}^{b} [T_b^\Phi]^T (\{F_b^{\sup}\} - [L_b^{\sup}]\{\gamma_b\}) \\ \{H^\Gamma\} &= \sum_{b=1}^{n_b} [T_b^\Gamma]^T (\{G_b^{\sup}\} - [K_b^{\sup}]\{\gamma_b\}) \end{aligned} \tag{5.19}$$

Once the global system is solved, the solution for the potential for a block is obtained by first computing the values for the ”master” DOFs (using (5.15)) and subsequently performing a backsubstitution to determine the slave DOFs from (5.10). This procedure is carried out using the decomposed matrix $\left[L^{ss}\right]$ which is stored on disk during the elimination step.

Advantages of the method

Here the main advantages of the method are summarized:

- The presented method exploits the geometrical symmetry of the flow channels in the rotor. Only the superelements of a single flow channel need to be computed, since they are identical.
- The superelement matrices have to be computed only once during an unsteady computation.
- The Kutta conditions are imposed implicitly. Therefore the need no longer exists to determine a large number of subpotentials in order to impose the Kutta condition at all trailing edge nodes. This is especially important in three-dimensional computations where the number of subpotentials increases rapidly, since the circulation varies along the span of the trailing edges.
- The elimination of internal DOFs results in a major reduction of computing time for unsteady computations, since these computations are performed with a greatly reduced number of DOFs.

Implementation

The developed numerical method has been implemented in the parametric hydraulic analysis system *COMPASS* [24]. Second-order accuracy for potential, velocities and pressures is obtained by employing linear elements in combination with the SPR-technique [36] for the determination of the gradient of the potential, i.e. the velocity. In the global solution step the system of equations is solved using a direct method. The profile width of the sparse global matrix is reduced using a spectral renumbering technique [22], [29].

The various forms of modelling the wakes have been implemented.

Implementation of wake models

This appendix deals with some aspects of the implementation of the wake models. A detailed account is given in [18]. The value of the potential jump on the wake depends on the type of computation. Two types are distinguished: quasi-steady computations (without unsteady wakes) and unsteady computations (with unsteady wakes). The wake representation is shown in Figure 3.3. As explained below, these computations differ in the nature of the jump distribution on the wake: known versus unknown jumps.

Quasi-steady computations

The flow field in a rotor-stator configuration of a pump will in general be unsteady. Especially at off-design conditions, the blade circulations will vary in time. One way of computing this unsteady flow would be to incorporate the variation of blade circulations along the span, but to neglect the convection of shed vortices in the wake. This is called the quasi-steady approach. If wake surfaces could extend from the trailing edges down to the exit pipe of the pump, the potential jumps would be described properly by (5.1). However, these surfaces cannot be extended beyond the cylindrical or conical rotor-stator interface. Therefore the varying potential jump on the wake must become constant upon reaching this interface. In other words, the varying potential jump on the wake must eventually be averaged out. The value of the potential jump on the wake is now described by

$$\gamma(s_1, s_2) = \Gamma(s_2) + \alpha(s_1, s_2)[\,\Gamma_{ave} - \Gamma(s_2)\,] \qquad \textbf{(5.20)}$$

where Γ_{ave} is the spanwise average of the blade circulation. The factor α is dependent on the position in the wake and varies between the value 0 at the trailing edge and the value 1 at the rotor-stator interface. The second term at the right hand side can be considered as a deviation from Kelvin's circulation theorem. However, when averaging this deviation over all wake nodes at constant s_1-coordinate, this averaged deviation reduces to zero. At the rotor-stator interface, the averaged value of the potential jump is guided to the outer wall of the pump, along part of the cylindrical or conical rotor-stator interface and some block boundaries located in the stator region of the pump. This type of averaging of the jump distribution is depicted in Figure 5.2.

In this type of wake modelling the jump distribution is determined completely by the unknown blade circulations.

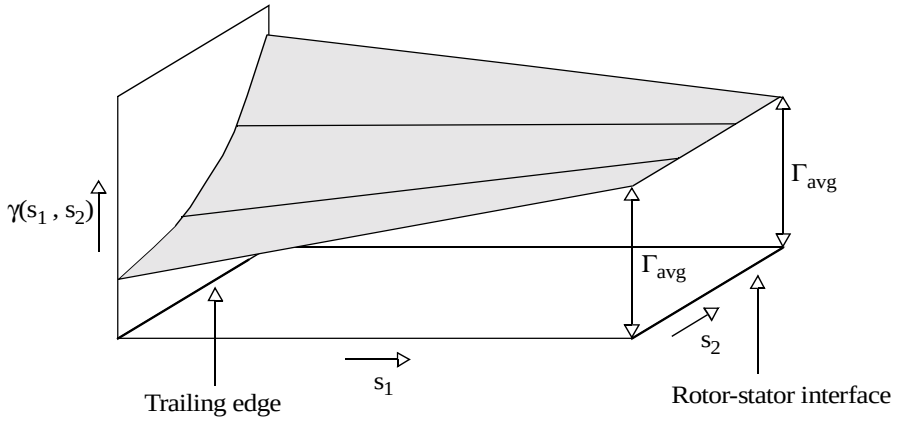

FIGURE 5.2. Schematic representation of the potential jump distribution $\gamma(s_1, s_2)$ on a wake in quasi-steady computations. The average blade circulation is Γ_{avg}.

Unsteady computations

Contrary to the former approach, a (fully) unsteady computation of the flow field in a rotor-stator configuration requires the convection of vortices according to (3.8) to be taken into account as well. Once again, the varying potential jump will have to be averaged out at the rotor-stator interface. Suppose that the potential jump distribution at a given time step is given by $\gamma^*(s_1, s_2)$. An averaging procedure very similar to that for quasi-steady flow is now introduced

$$\gamma(s_1, s_2) = \gamma^*(s_1, s_2) + \alpha(s_1, s_2)[\gamma^*_{avg}(s_1) - \gamma^*(s_1, s_2)] \qquad \textbf{(5.21)}$$

where factor α depends on the position of the vortex in the wake and varies between the value 0 at the trailing edge and the value 1 at the rotor-stator interface. The average value of the potential jumps $\gamma^*(s_1, s_2)$ along the line with constant s_1 is denoted by $\gamma^*_{avg}(s_1)$. The deviation from the exact solution reduces to zero when averaging over nodes at constant s_1-coordinate. As was the case in the quasi-steady approach, the potential jump is equal to the local blade circulation at nodes on the trailing edge. Upon reaching the rotor-stator interface, the potential jump becomes equal for all s_2. This averaged value is guided to the outer wall of the pump.
In this type of wake modelling the jump distribution is determined by the unknown blade circulations and the known jump distribution on the wake corresponding to previously shed vortices.

CHAPTER 6

Loss models

In the basic potential-flow model viscosity is neglected. Since viscosity is the main source of losses, the basic potential-flow model can not be used to predict realistic head-capacity curves. In fact, the model would always predict a hydraulic efficiency of 100 %. This seems to make the potential-flow model almost useless.

However, it is important to realize that the potential-flow model is valid for the core flow (i.e. the flow in the region between the blades, but outside of boundary layers and wakes), provided no boundary-layer separation occurs. Then the core flow can be considered as inviscid. The viscous effects are restricted to thin zones along the walls of the rotor and stator, and in wakes behind trailing edges. In these thin zones viscosity dissipates energy. By developing separate models for these zones, viscosity can be accounted for very efficiently.

Sources of loss are dissipation by viscous stresses in boundary layers at solid walls, mixing losses in wakes, disk friction, leakage flows, tip losses, mechanical losses. Mechanical losses are not specified here, but they can be included by multiplying the efficiency by the mechanical efficiency.

Models are given for each of these sources of losses. Many of these models use the potential-flow field as input.

An overview of the various losses is given by Denton [17], while this chapter closely follows the exposition of [18].

Power balance

Only part of the power that is applied at the axis is transferred to the fluid. The power at the shaft is denoted by P_{shaft}, while the increase of fluid power is P_{net}. Then the power losses ΔP are

$$P_{\text{shaft}} = P_{\text{net}} + \Delta P \tag{6.1}$$

The shaft power P_{shaft} is related to the shaft torque M_{shaft} by

$$P_{\text{shaft}} = \Omega M_{\text{shaft}} \tag{6.2}$$

The increase in fluid power P_{net} is used to define the pump's head H

$$P_{\text{net}} = \rho g H Q \tag{6.3}$$

The efficiency of the pump η is defined by

$$\eta = \frac{P_{\text{net}}}{P_{\text{shaft}}} = \frac{P_{\text{shaft}} - \Delta P}{P_{\text{shaft}}} \tag{6.4}$$

The power lost ΔP is the sum of the various loss contributions

$$\Delta P = \Delta P_{\text{hydr}} + \Delta P_{\text{leak}} + \Delta P_{df} \tag{6.5}$$

where ΔP_{hydr} is the hydrodynamical loss of power, ΔP_{leak} is the power lost due to the leakage flow and ΔP_{df} is the power lost by disk friction. The hydrodynamical loss consist of mixing loss and frictional loss in the boundary layers. For each of these losses, models will be given in the following sections.

Shaft power

From the conservation of angular momentum (see also [2]) for the control volume shown in Figure 6.1 it follows

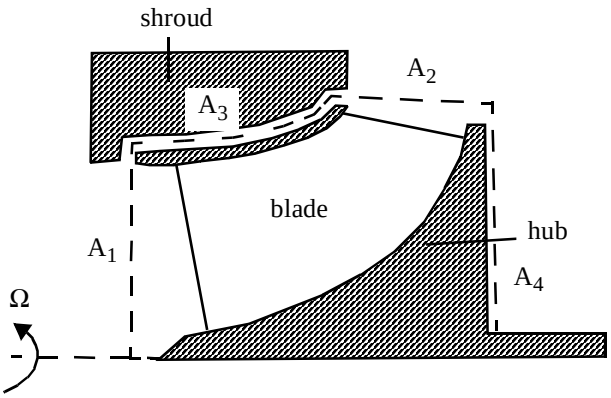

FIGURE 6.1. Control volume enclosing the impeller.

$$M_{\text{shaft}} + \int_A r F_{s,\theta}\, dA = \frac{\partial}{\partial t}\int_V \rho r v_\theta\, dV + \int_A \rho r v_\theta (\underline{v} \bullet \underline{n})\, dA \tag{6.6}$$

The term with the time derivative can be ignored, since its time-averaged contribution (over a period of revolution of the impeller) equals zero for the periodic situation considered. The term $F_{s,\theta}$ is a wall-shear surface force in circumferential direction. It can be neglected for the inlet and outlet surfaces A_1 and A_2.

The effect of the boundary layers on the velocity profiles at entrance and exit are neglected. Then

$$M_{\text{shaft}} = M_{\text{Euler},\, Q + Q_{leak}} + M_{df} \tag{6.7}$$

where

$$M_{\text{Euler},\, Q + Q_{leak}} = \int_{A_1 + A_2} \rho r v_\theta (\underline{v} \bullet \underline{n})\, dA \tag{6.8}$$

The inviscid Euler moment $M_{\text{Euler},\, Q + Q_{leak}}$ is the torque exerted by the impeller blades on the internal fluid by pressure forces. The larger flowrate due to the leakage flow has to be taken into account. The torque M_{df}, acting in the direction opposite to the shaft torque M_{shaft}, is the torque exerted by frictional shear stresses at the surfaces external to the impeller

$$M_{df} = -\int_{A_3 + A_4} r\tau_{w,\theta} dA \tag{6.9}$$

Boundary-layer losses

Due to the presence of solid walls, boundary layers form in which (generally) the flow adjusts from the core velocity to the slip condition at the wall, see Figure 6.2.

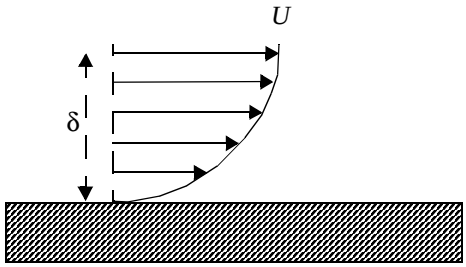

FIGURE 6.2. Velocity profile in the boundary layer.

According to [17], the power loss in boundary layers ΔP_{bl} is

$$\Delta P_{bl} = \frac{1}{2}\rho \int_A c_D w^3 dA \tag{6.10}$$

dissipation coefficient

The coefficient c_D is a *dissipation coefficient*. A representative value is 0.004. Its value is not very sensitive to the state of the boundary layer, although it may very from 0.002 for boundary layers in accelerating flow, to 0.005 for boundary layers in decelerating flow.

Note the analogy of (6.10) with the expression for the shear stress at the wall τ_w

$$\tau_w = \frac{1}{2}\rho c_f w^2 \tag{6.11}$$

where c_f is a friction coefficient.

Expansion and contraction losses

A sudden change in through-flow area may lead to dissipation of kinetic energy, see for example [18] for more information. The magnitude of this source of loss is usually of minor importance.

Wake mixing

An important type of loss is the mixing of the boundary layers in the wake behind a blade, see Figure 6.3. According to [17] this mixing loss is given by

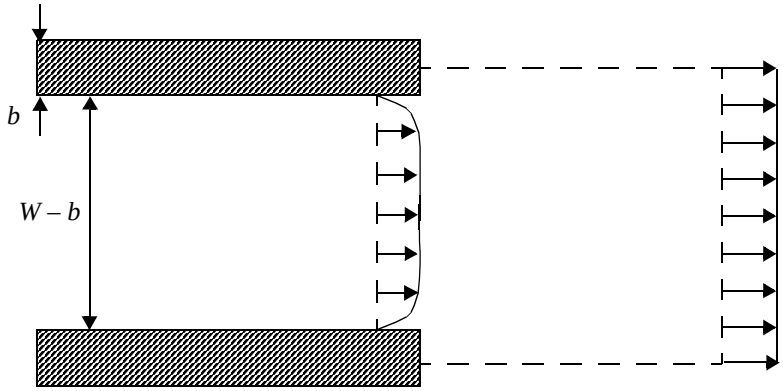

FIGURE 6.3. Control volume behind trailing edge.

$$\Delta P_{mix} = (Q + Q_{\text{leak}})\frac{1}{2}\rho w_{\text{ref}}^2\left[-\frac{C_{pb}}{W} + 2\frac{\theta}{W} + \left(\frac{\delta^* + b}{W}\right)^2\right] \quad \textbf{(6.12)}$$

where b is the blade thickness, W is the blade pitch. The sum of the momentum thicknesses of the boundary layers on the pressure and suction sides of the blades is denoted by θ. The sum of the displacement thicknesses is δ^*. The so-called base pressure coefficient C_{pb} is defined by

$$C_{pb} = \frac{p_b - p_{\text{ref}}}{\frac{1}{2}\rho w_{\text{ref}}^2} \quad \textbf{(6.13)}$$

where p_b is the static pressure acting on the blunt trailing edge, p_{ref} and w_{ref} are reference values for the pressure and velocity. A typical value for the base pressure coefficient C_{pb} is –0.15.

The first term in (6.12) represent the loss due to the low pressure acting on the blunt trailing edge, the second term is the actual mixing loss, while the third term signifies the effect of blockage by the blade and the boundary layers.

A detailed overview of various theories for predicting the base pressure is given in [31].

Disk friction

Consider a disk with radius R that is rotating with angular velocity Ω in a cylindrical container. At the bottom of the container a thin layer of liquid is present with thickness h. Due to viscous stresses at the bottom of the disk power is required to keep the disk spinning. This disk friction power P_{df} that continuously has to be provided to the system equals

$$P_{df} = \Omega M_{df} \quad \textbf{(6.14)}$$

where the frictional torque M_{df} acting on a rotating radial disk is given by (neglecting shear stresses at the top of the disk by air, for example)

$$M_{df} = \int_A r\tau dA \quad \textbf{(6.15)}$$

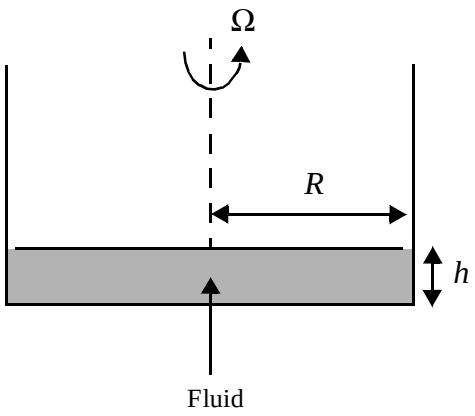

FIGURE 6.4. Geometry for disk friction.

where τ is the shear stress in circumferential direction. The shear stress can be expressed as

$$\tau = \frac{1}{2}\rho C_f v^2 = \frac{1}{2}\rho C_f (\Omega r)^2 \tag{6.16}$$

For a disk of radius R this leads to

$$M_{df} = \frac{1}{5}\pi\rho C_f \Omega^2 R^5 \equiv \frac{1}{2}\rho C_m \Omega^2 R^5 \tag{6.17}$$

where $C_m \equiv 2\pi/5 C_f$.

Correlations for C_m were obtained by [16]. Four different regimes were identified, depending on the type of flow, laminar or turbulent, and whether separate boundary layers exist on both sides of the solid surfaces, or the boundary layers have merged.

These regimes are characterised by a nondimensional Reynolds number $Re = \Omega R^2/\nu$ and a nondimensional gap parameter $G = h/R$.

- Regime I: laminar flow, boundary layers have merged

$$c_m = \pi G^{-1} Re^{-1} \qquad \begin{cases} G < 1.62 Re^{-5/11} \\ G < 188 Re^{-9/10} \end{cases} \tag{6.18}$$

- Regime II: laminar flow with two separate boundary layers

$$c_m = 1.85 G^{1/10} Re^{-1/2} \qquad \begin{cases} G > 1.62 Re^{-5/11} \\ G > 0.571 0^{-6} Re^{15/16} \\ Re < 1.581 0^5 \end{cases} \tag{6.19}$$

- Regime III: turbulent flow, boundary layers have merged

$$c_m = 0.040 G^{-1/6} Re^{-1/4} \qquad \begin{cases} G < 0.571 0^{-6} Re^{15/16} \\ G < 0.402 Re^{-3/16} \\ G > 188 Re^{-9/10} \end{cases} \tag{6.20}$$

- Regime IV: turbulent flow with two separate boundary layers

$$c_m = 0.051 G^{1/10} Re^{-1/5} \qquad \begin{cases} G > 0.402 Re^{-3/16} \\ Re > 1.5810^5 \end{cases} \tag{6.21}$$

The regimes are shown in Figure 6.5.

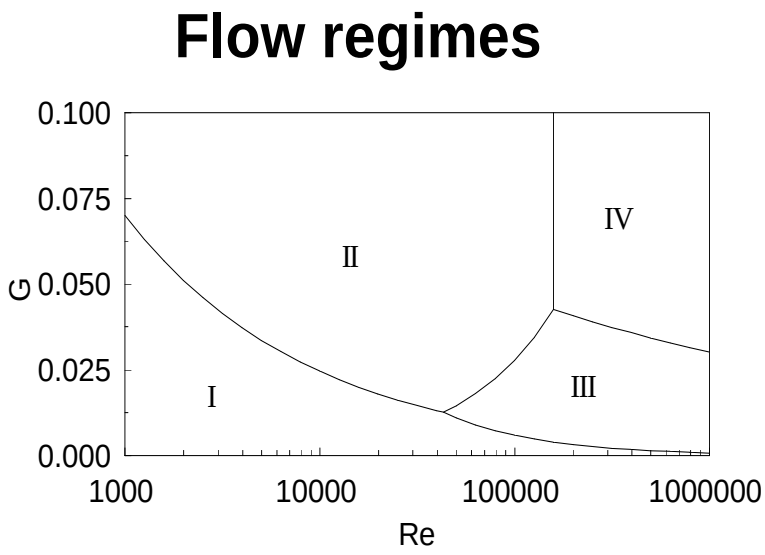

FIGURE 6.5. Regimes for disk friction.

Leakage flow

Many hydraulic turbomachines are equipped with (rotating) shrouds. In order to minimize leakage flow, various types of seals are used. Without seals between the shaft and the pump housing, the fluid would squirt out of the pump, due to its high pressure.

Here a model is given for the mixing loss due to the leakage flow joining the main flow and a model is given for determining the leakage flowrate. This latter bulk flow model also provides the contribution of disk friction associated with the leakage flow.

Mixing loss

Due to the mixing of the leakage flow with the main flow, the flow incurs a loss. From conservation of axial momentum for the control volume depicted in Figure 6.6 it follows that

$$(p_2 + \rho v_{z,2}^2) A_2 = (p_3 + \rho v_{z,3}^2) A_3 \tag{6.22}$$

Assuming that the main flow is irrotational, the final circumferential velocity of the mixed-out flow is determined from conservation of angular momentum

$$v_{\theta,\text{leak}} Q_{\text{leak}} = \frac{1}{2} v_{\theta,3} (Q + Q_{\text{leak}}) \tag{6.23}$$

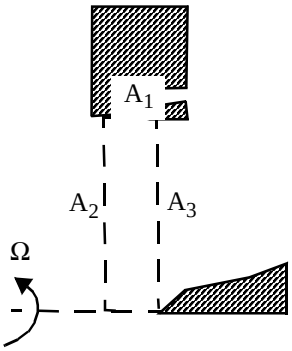

FIGURE 6.6. Control volume at the impeller inlet.

The factor 1 / 2 follows from the reduction in average radius. Since $A_1 = A_3$, the loss in total pressure is Δp_0

$$\Delta p_0 = \frac{1}{2}\rho\frac{(2\varepsilon + \varepsilon^2)}{(1+\varepsilon)^2}v_{z,3}^2 - \frac{1}{2}\rho\frac{4\varepsilon^2}{(1+\varepsilon)^2}v_{\theta,\,\mathrm{leak}}^2 \tag{6.24}$$

where $\varepsilon = Q_{\mathrm{leak}}/Q$.
The power loss through mixing ΔP_{mix} then becomes

$$\Delta P_{\mathrm{mix}} = (Q + Q_{\mathrm{leak}})\Delta p_0 = Q_{\mathrm{leak}}\left[\frac{1}{2}\rho\left(\frac{2+\varepsilon}{1+\varepsilon}\right)v_{z,3}^2 - \frac{1}{2}\rho\left(\frac{4\varepsilon}{1+\varepsilon}\right)v_{\theta,\,\mathrm{leak}}^2\right] \tag{6.25}$$

Bulk-flow model for conical leakage area

In most cases the leakage flow is through a narrow conical gap with a constant height h. Hence, in relation to the geometry sketched in Figure 6.1, a conical gap for the leakage flow corresponds to a shroud that is straight. The steady momentum equations in the conical coordinate system, see Figure 6.7, are

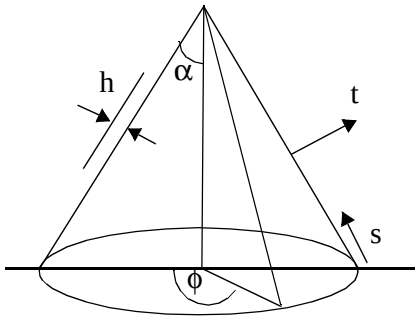

FIGURE 6.7. Conical coordinate system.

$$\begin{aligned}\rho\left(v_s\frac{\partial v_s}{\partial s} + \sin\alpha\frac{v_\theta^2}{r}\right) &= -\frac{\partial p}{\partial s} - \frac{1}{r}\frac{\partial}{\partial t}(r\tau_{st})\\ \rho\left(v_s\frac{\partial v_\phi}{\partial s} - \sin\alpha\frac{v_\theta v_s}{r}\right) &= -\frac{1}{r^2}\frac{\partial}{\partial t}(r^2\tau_{\phi t})\end{aligned} \tag{6.26}$$

for the throughflow direction t and the circumferential direction ϕ.
For a thin film the derivatives of the shear stresses in the t-direction are

$$\frac{\partial \tau_{st}}{\partial t} = \frac{\tau_{st}^S + \tau_{st}^R}{h} \tag{6.27}$$

$$\frac{\partial \tau_{\phi t}}{\partial t} = \frac{\tau_{\phi t}^S + \tau_{\phi t}^R}{h} \tag{6.28}$$

where the superscripts R and S denote values at the rotating and stationary walls.
The shear stresses are expressed as

$$\tau_{\phi t}^S = C_f^S \frac{1}{2} \rho v_\phi v^S \tag{6.29}$$

$$\tau_{\phi t}^R = C_f^R \frac{1}{2} \rho (v_\phi - \Omega r) v^R \tag{6.30}$$

$$\tau_{st}^S = C_f^S \frac{1}{2} \rho v_s v^S \tag{6.31}$$

$$\tau_{st}^R = C_f^R \frac{1}{2} \rho v_s v^R \tag{6.32}$$

where v^S and v^R are the magnitudes of the bulk velocities relative to the rotating and stationary walls

$$\begin{aligned} v^S &= \sqrt{v_s^2 + v_\phi^2} \\ v^R &= \sqrt{v_s^2 + (v_\phi - \Omega r)^2} \end{aligned} \tag{6.33}$$

Various empirical relations can be employed for the various friction factors, see [18].
For a given leakage flow Q_{leak}, corresponding to known distribution of v_s from mass conservation, the equations (6.26) can be solved for the circumferential velocity v_ϕ and the pressure p. The leakage flow has to be adjusted such that it gives the pressure drop corresponding to the head increase of the impeller.
The power loss associated with the leakage flow consists of two parts. The first part is disk friction, which can be computed once the velocity distribution in the gap is known, since the shear stress is determined from the velocities and the friction coefficients. The second part is due to the fact that in the impeller the pressure increases, but the pressure increase of the leakage flow is lost. Hence

$$\Delta P_{\text{leak}} = Q_{\text{leak}} \rho g H_{\text{imp}} \tag{6.34}$$

where H_{imp} is the head increase over the impeller.
Examples of results for the pressure distribution in seals are given in [18].

CHAPTER 7

Cases

This chapter shows various examples of the methodology described in preceding chapters: the potential-flow model is used to describe the core flow and additional models for the various sources of losses are employed that use the potential-flow field as input. The examples vary in range of specific speed from a low specific-speed centrifugal pump to a high specific-speed axial cooling fan.

Centrifugal pump, free impeller

In order to study the flow in centrifugal impellers, detailed measurements of velocity and pressure have been performed for the SHF impeller (Societé Hydraulique de France). This is a low specific speed, $n_\omega = (\Omega\, Q^{1/2})/(g\, H)^{3/4} = 0.58$, centrifugal impeller with seven blades. Its inlet diameter is 220 mm and its outlet diameter is 400 mm. The blade outlet angle is 67.5° with respect to the radius. At 1200 rpm, the nominal flowrate Q_n is 0.1118 $m^3 \cdot s^{-1}$ and the corresponding head is 31 m. The geometry is shown in Figure 7.1.

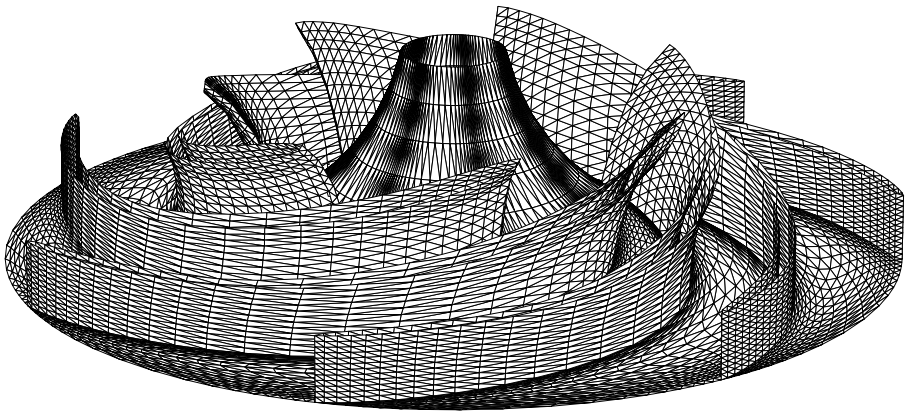

FIGURE 7.1. Geometry of SHF impeller.

The results of Laser Doppler Velocimetry measurements are reported in [15] and the results of pressure measurement are given in [27]. Since a detailed description of the geometry is available, this impeller was analysed with the present code [19]. In the computation the thickness of the impeller blades was taken into account. Here the main results are recapitulated.

The computed head H equals 33 m in comparison with the measured head of 31 m. The computed and measured pressure distribution on the blade is plotted in Figure 7.2; good agreement is observed. A detailed comparison of computed and measured velocities is given in [19].

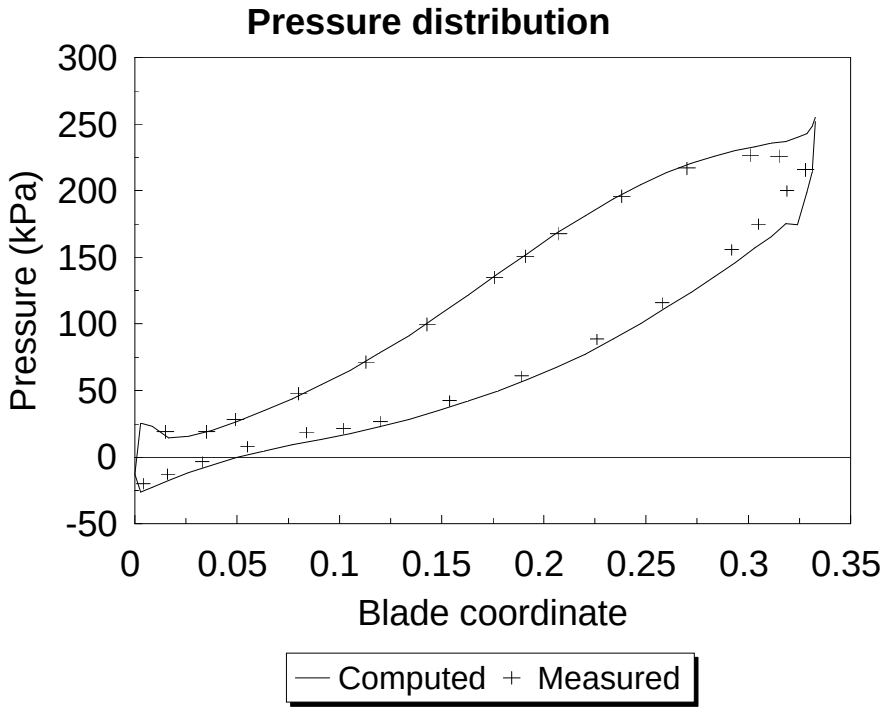

FIGURE 7.2. Computed and measured pressure distribution on SHF impeller.

Centrifugal pump, volute

This section is based on [23]. This example deals with the flow in a low-specific speed pump consisting of an impeller with logarithmic blades and a volute. The emphasis of this case is on the flow in the volute.

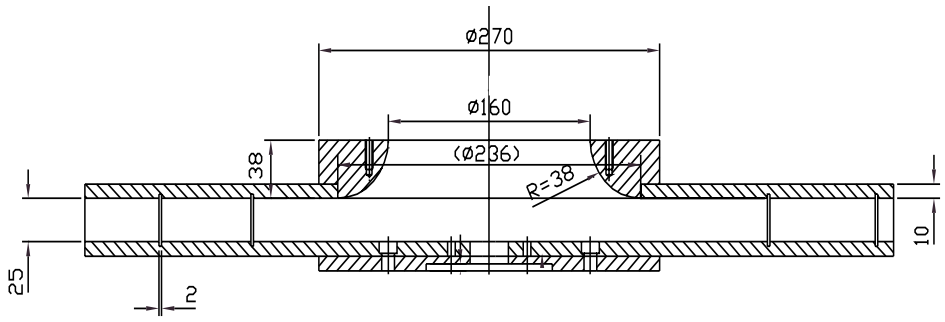

FIGURE 7.3. Centrifugal impeller (cross-section). All dimensions in mm.

Measurements were performed at a centrifugal pump with a low specific-speed $n_\omega = (\Omega\, Q^{1/2})/(g\, H)^{3/4}$ of 0.4. The impeller (see Figure 7.3) has seven blades with a constant blade angle of 70° with respect to the radius and a thickness of 2 mm. The impeller inner diameter is 320 mm, its outer diameter 640 mm, and the axial width is 25 mm. The volute, see Figure 7.4, has a trapezoidal cross-section and is designed to approximately match the impeller at design condition (Q = 0.008 m^3/s, Ω = 4.2 rad/s), according to the

method of constant angular momentum [5] (see also Chapter 7). The Reynolds number $(\Omega D^2)/\nu$ is $1.7 \cdot 10^6$, where ν is the kinematic viscosity of water. The tongue has a cylindrical shape with a diameter of 2 mm. During construction special attention was paid to the minimization of leakage flows. Measurements are presented for flowrates of 82.5 %, 100 % and 117.5 % of the design flowrate.

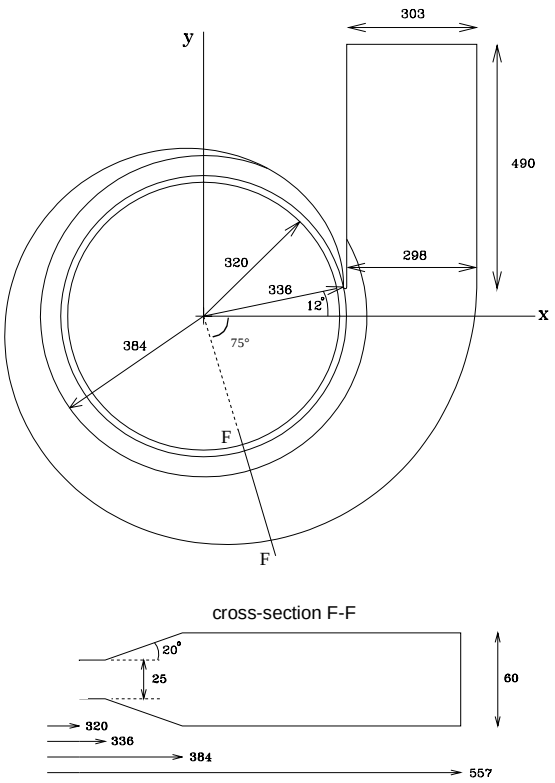

FIGURE 7.4. Spiral volute (plane view and cross-section) All dimensions in mm.

Velocity measurements were performed using LDV. The LDV configuration is described in detail in [32] and [33]. It employs a dual reference beam forward scattering system, capable of parallel detection of two perpendicular velocity components. Two Bragg cells were used to effectuate preshifts between main beam and the two reference beams, thus enabling the determination of the direction of the velocity components. Two detectors measured the Doppler frequency. These signals were sampled and stored on disk. Time-averages and RMS-values could be computed. Information on the axial velocity component could not be obtained. U-tube manometers were used to obtain values of the static pressure. Figure 7.5 shows the locations in the volute where velocity and static pressure measurements were obtained.

The head-capacity curve was derived from the static pressure difference between inlet and outlet of the pump and the assumption of uniform velocity in these regions. It is not possible to measure the hydraulic efficiency of the pump with the current experimental setup.

Air-bubble visualization was used to investigate the flow near the tongue of the volute.

Results

In this section the results of measurements and computations are compared. These results deal with velocities, pressures and overall characteristics. The computational mesh is shown in Figure 7.6. It contains a total of 168,000 nodes, of which 14,500 are located in

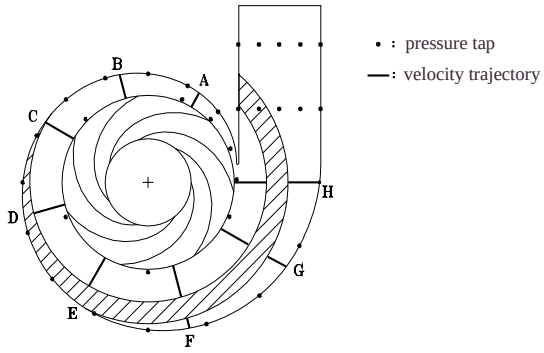

FIGURE 7.5. Measurement locations in the laboratory centrifugal pump. LDV measurements are performed along trajectories *A* to *H*. Static pressure measurement locations are indicated with solid markers. Hatched area shows region which is not visually accessible.

each of the seven impeller channels Computations are performed with 105 timesteps per shaft revolution. Although the computations yielded time-dependent quantities, only time-averaged quantities are presented.

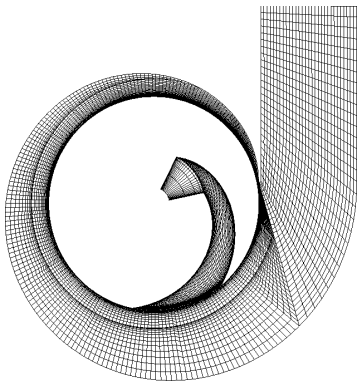

FIGURE 7.6. Plane view of the computational mesh for the centrifugal pump with spiral volute. Only one of the seven impeller channels is shown.

Velocity

Radial and circumferential velocity components were measured in a plane at half the axial width of the volute. Several trajectories (see Figure 7.5) were scanned for the three flowrates 82.5 %, 100 % and 117.5 % of the nominal flowrate.

Typical results are shown in Figure 7.7, together with the computed values. In a large region of the volute (60°-285° from the tongue) computed circumferential velocities agree very well with measurements at optimum flow conditions. At low flowrate this excellent agreement is restricted to a smaller region (150°-285° from the tongue). At high flowrate the agreement is not very good except for a small region 60°-150° from the tongue. The agreement between computed and measured radial velocities is very poor.

This discrepancy was further investigated by performing traverses over the height of the volute. Results are given in Figure 7.8 which shows the variation of radial and circumferential velocity over the height of the volute for two radial positions on traverse F (see Figure 7.5). The circumferential velocity is practically constant over the height of the volute, while the (much smaller) radial velocity shows severe secondary flow.

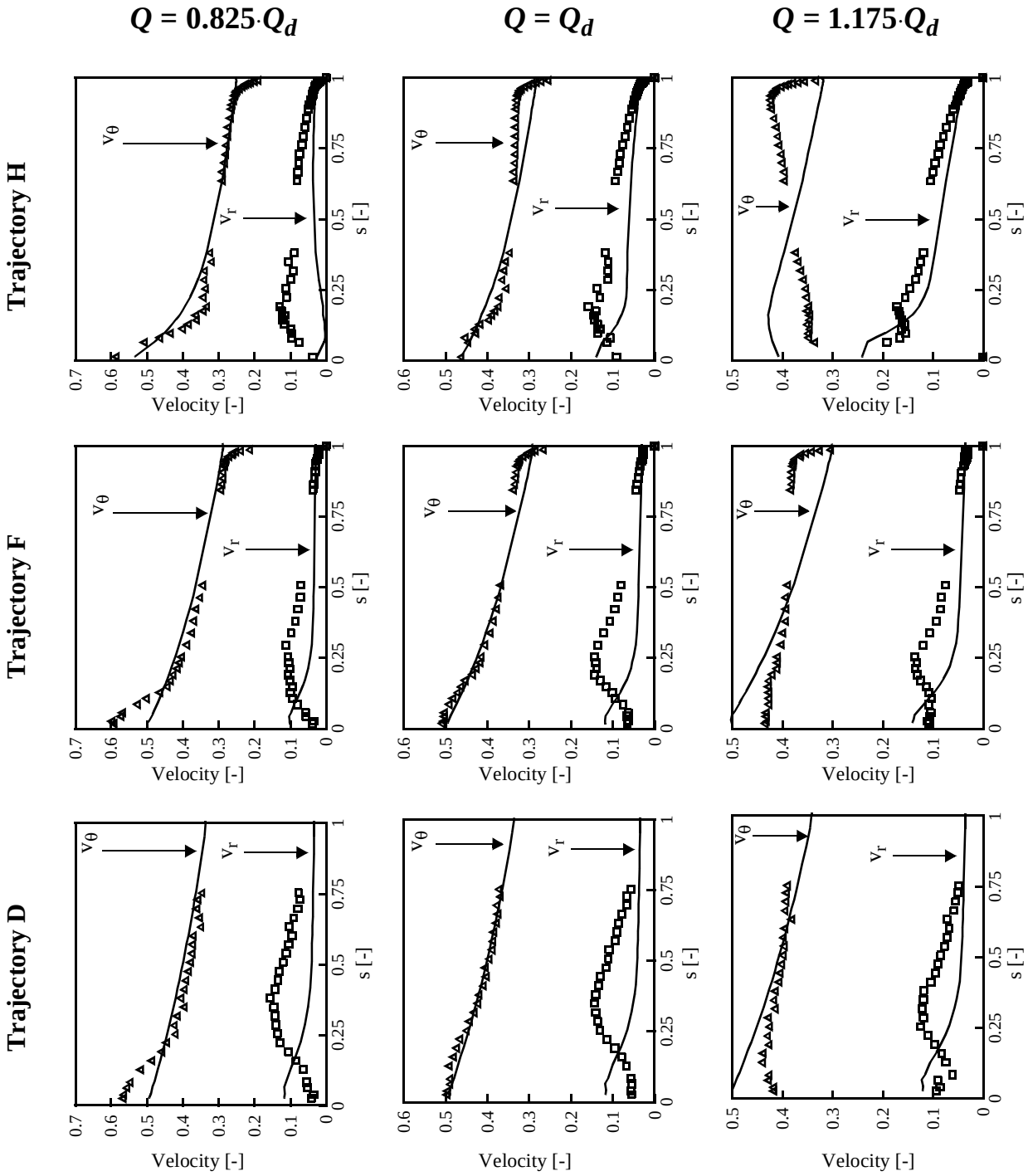

FIGURE 7.7. Nondimensional radial and circumferential velocity in the volute along different trajectories for three flowrates. Comparison between measurements (symbols) and computations (solid line). The scaled local coordinate along the trajectory is denoted by *s*, ranging from 0 at the impeller outer radius to 1 at the volute wall. Velocities are scaled with blade tip speed.

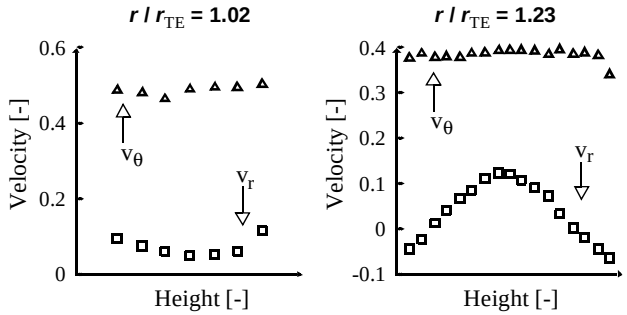

FIGURE 7.8. Variation of radial and circumferential velocities with height for two radial positions on trajectory *F* (blade tip radius denoted by r_{TE}). Velocities are scaled with blade tip speed.

Pressure

The static pressure difference Δp between the inlet of the pump and locations in the volute is measured using U-tube manometers. It is made nondimensional with the blade tip speed according to

$$\Delta p = \frac{p_{vol} - p_{inlet}}{\rho(\Omega r_2)^2} \tag{7.1}$$

In Figure 7.9 results of measurements and computations are shown for locations just outside the impeller and along the volute outer wall, for three different flowrates. The (inviscid) computations lead to pressure values which, on the average, are too high. However, in a large region, not too near to the tongue, the qualitative agreement is quite good. A constant static pressure around the impeller can be observed at design flowrate. The computed static pressure values can be corrected for viscous losses in the impeller

$$\Delta p_{corr} = \Delta p_{invisc} - \rho g H_{L,h,imp} \tag{7.2}$$

where the hydraulic head loss in the impeller is denoted by $H_{L,h,imp}$. By doing so, the agreement is improved, although considerable deviations still occur at off-design conditions.

Head curve

Figure 7.10 shows the head-capacity curve. The methods described in Chapter 6 are used to quantify the effects of boundary-layer dissipation and wake mixing. The fraction that wake mixing contributes to the total head loss ranges from 10% at high mass flow to 25% at low mass flow.

Discussion

An investigation of the axial distribution of radial velocities at a number of radial positions in the impeller and the volute revealed that a region of severe secondary flow is located in the volute. Typical radial velocity profiles are sketched in Figure 7.11. The observed convex radial velocity profile in the volute region, with negative velocities near the upper and lower surfaces, can easily be explained by an analysis of pressure forces and centrifugal forces (due to curvature) in the boundary layers and the main flow. It is equivalent to the secondary flow encountered in the flow through a pipe bend. A similar analysis for the flow through the impeller can be made, where account should be given of the additional centrifugal force due to rotation and the Coriolis force. The equilibrium

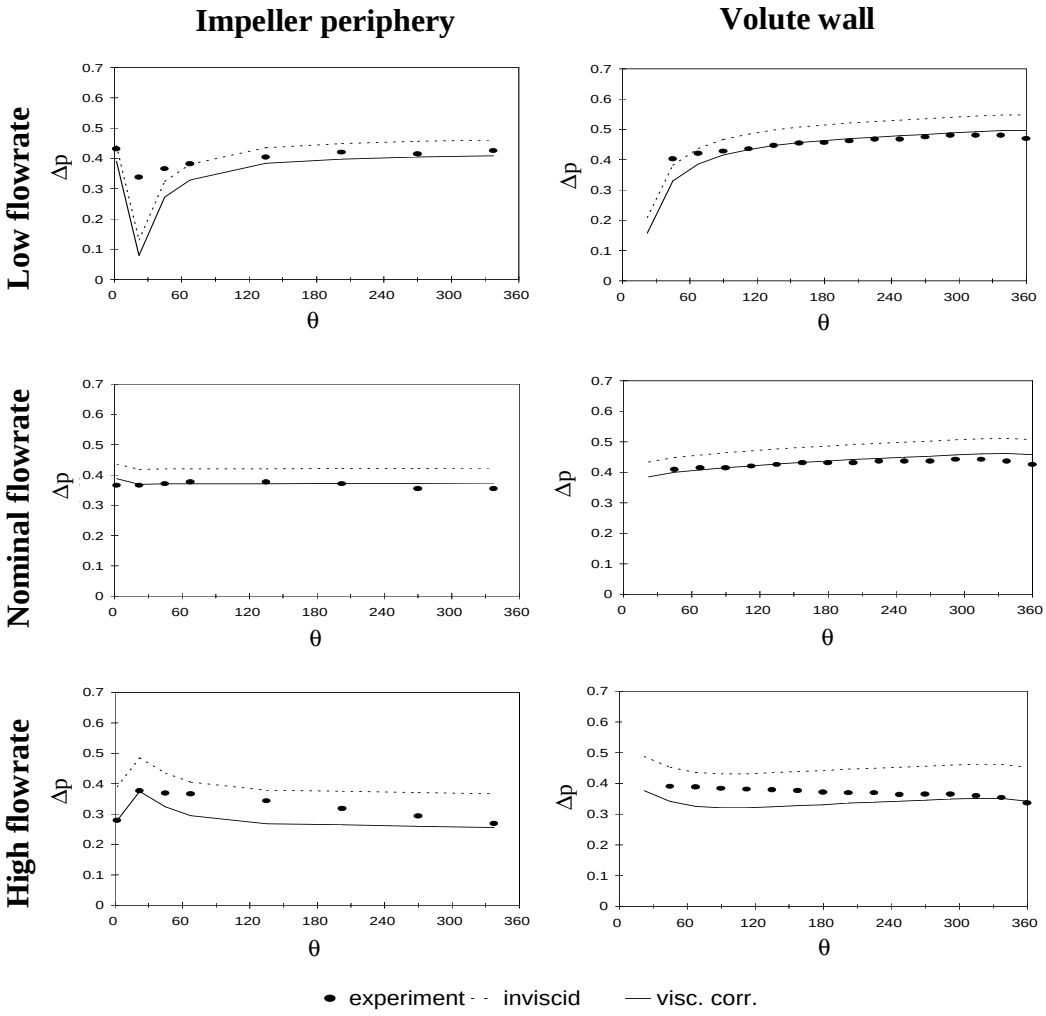

FIGURE 7.9. Static pressure difference in the volute of the laboratory centrifugal pump as a function of orientation θ (degrees) from the volute tongue, for three flowrates. See Figure 7.5 for locations at the impeller periphery and the volute wall. Pressure difference Δp is defined in (7.1) and (7.2).

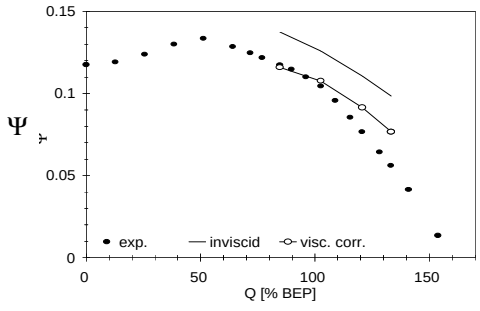

FIGURE 7.10. Head-capacity curve for the centrifugal pump, showing measured and computed values, both inviscid and corrected for viscous losses.

between pressure forces and Coriolis forces in the main flow is lost in the boundary layers at hub and shroud surfaces, leading to a secondary flow in the boundary layers

directed from pressure to suction side. In the main flow a reverse secondary flow direction is observed. This leads to the observed concave radial velocity profile for impellers with backwardly curved blades. Secondary flows are discussed in more detail in Chapter 9.

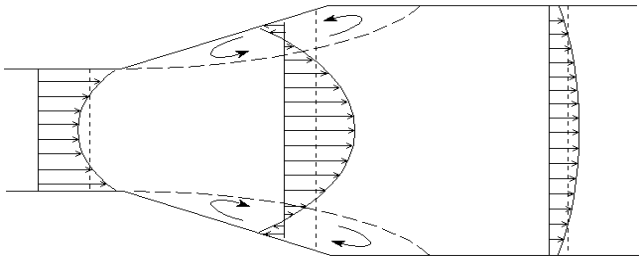

FIGURE 7.11. Cross section of impeller and volute, showing measured radial velocity profiles. Average velocities are indicated with dotted lines

The secondary flow does not seem to influence the static pressures. Except at the high flowrate, the agreement between measurements and potential-flow computations (after correcting for viscous losses in the impeller) is quite good. It can be observed from the difference between both that viscous losses build up as the fluid is flowing along the volute wall from the tongue to the volute throat.

Similar results are obtained for the head-capacity curve. The good agreement at low and optimum flowrate imply that other sources of viscous losses are not very important in this pump. At high flowrate, however, a larger deviation is observed between computations and experiments.

A possible cause for the disagreement between measurements and computations is boundary has been experimentally observed at high flowrate (Figure 7.12).

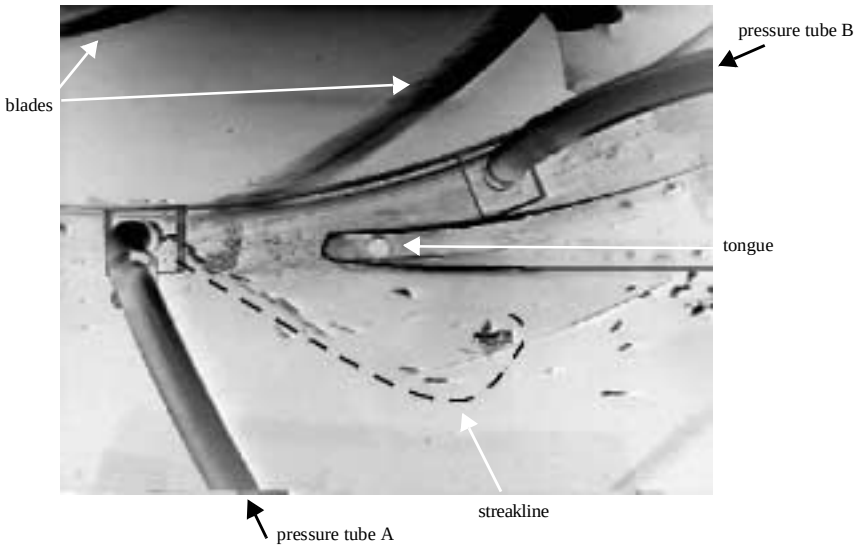

FIGURE 7.12. Photograph of flow near the tongue of the volute at high flowrate showing boundary layer separation. Air bubbles inserted through pressure tube A are used for flow visualization.

The blockage effect resulting from the separated boundary-layer could well be related to the observed tangential velocity profiles at high flowrate, which deviate considerably from the computations. A homogeneous distribution of tangential velocity was seen to cover the major part of the volute extending from trajectories B to G (Figure 7.5). It is suggested that measured velocity profiles like these have inspired Stepanoff [6] to put

forward his method of constant mean velocity for constructing volutes. A similar flow field can emerge at design flowrate if the volute is designed somewhat too small. It is known that volutes designed according to the method of Stepanoff are smaller than those designed according to the method of constant angular momentum [5].

Mixed-flow pump

This section summarises the description in [20] and [21]. Experiments were performed at the test facility of Flowserve Hengelo, The Netherlands. The model contains a shrouded mixed-flow impeller with four blades and has a specific speed n_ω of 1.6, see Figure 7.13.

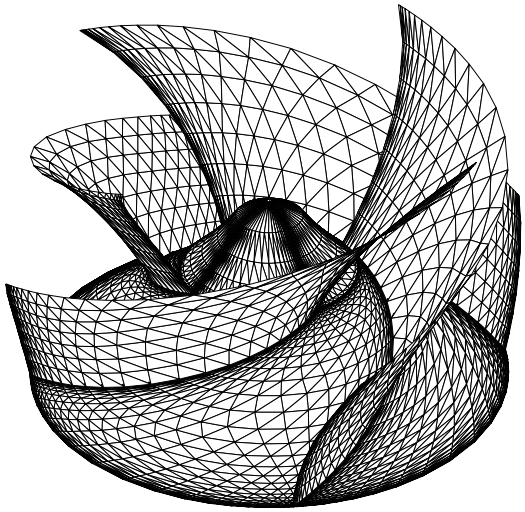

FIGURE 7.13. Geometry of impeller of mixed-flow pump.

The volute is unvaned with a trapezoidal cross-section, see Figure 7.14. It is designed according to the method of constant angular momentum [5] (see also Chapter 9).

The pump is a scale model of a much larger pump used for cooling-water transportation in power stations. Two types of measurements were carried out; overall performance measurements and detailed pressure measurements in the volute. The pressure measurements and their comparison to the computational results are given in [20].

Overall performance characteristics include the head-capacity curve and the efficiency curve. Figure 7.15 shows both the experimental and computed values. Results of inviscid computations are corrected for viscous losses, using the models described in Chapter 6. In contrast to the laboratory centrifugal pump, boundary-layer dissipation is by no means the only source of loss. The ratios Q_{leak} / Q were found to be quite high, varying from 1.7% at high flowrate ($Q = 1.4\, Q_n$) to 6.4% at the lowest flowrate considered ($Q = 0.6\, Q_n$). A small portion of the total loss is accounted to mixing losses, an even smaller portion to expansion losses. Large deviations at very low and high flowrates may be attributed to secondary flow like stall and surge, or to boundary-layer separation.

Cavitation

This section summarises some results from [28]. To be added.

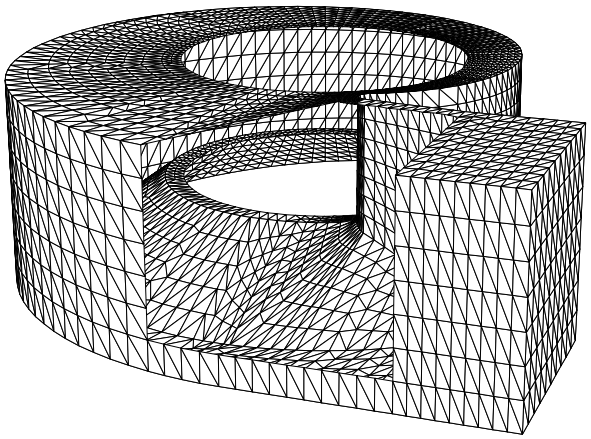

FIGURE 7.14. Geometry of volute of mixed-flow pump.

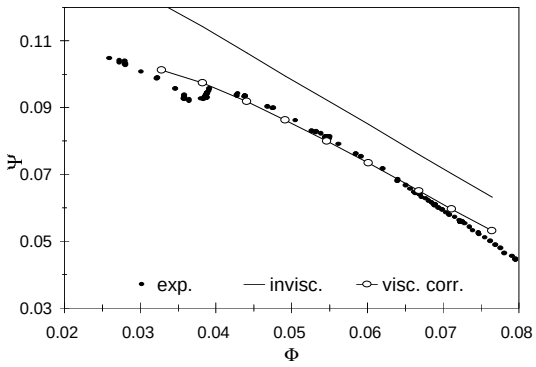

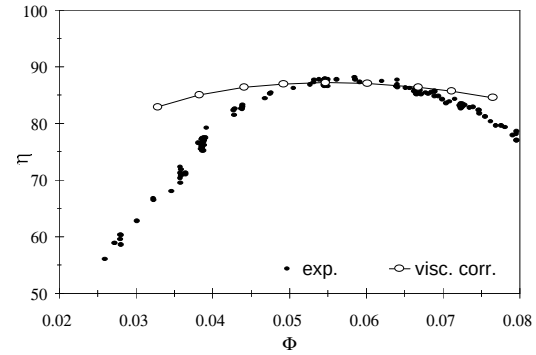

FIGURE 7.15. Head-capacity and efficiency curves of mixed-flow pump.

Axial fan

This section deals with axial cooling fans from Howden Cooling Fans, Hengelo, The Netherlands. Various configurations have been considered, see Figure 7.16. A detailed account is given in [13].

FX: 8 blades

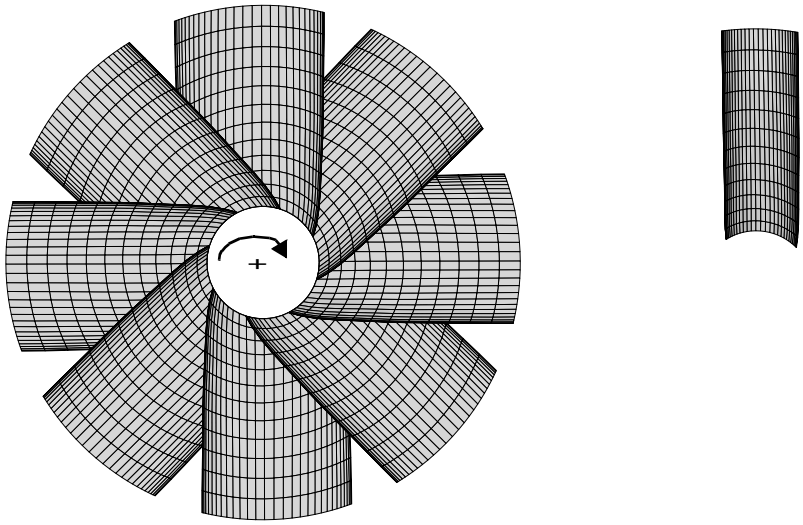

SX: 4 blades

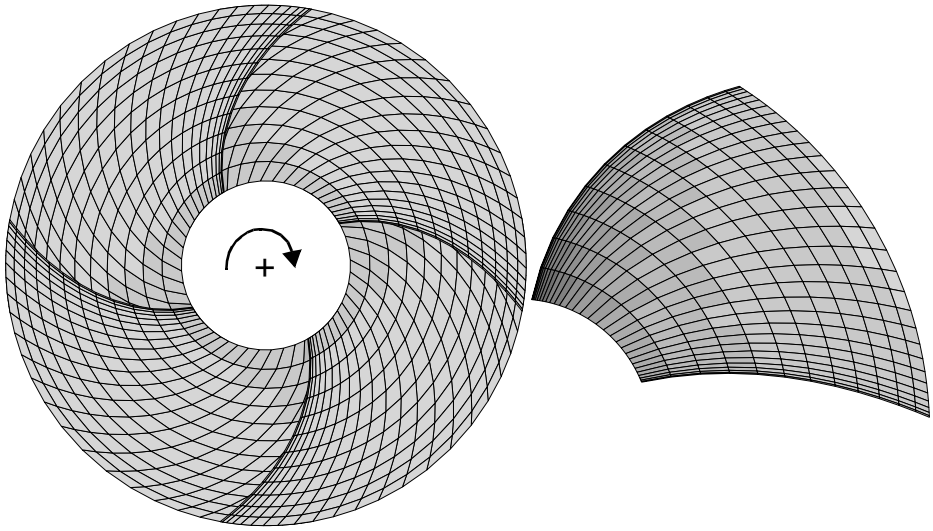

FIGURE 7.16. Geometry of FX and SX cooling fans.

For axial cooling fans the nondimensional quantities of interest determining the performance characteristics are the flow coefficient C_f, the pressure coefficient C_p and the power coefficient λ

$$C_f = \frac{c_x}{\Omega R_{\text{tip}}} \qquad C_p = \frac{p_{\text{out}} - p_{0,\text{ in}}}{\frac{1}{2}\rho(\Omega R_{\text{tip}})^2} \qquad \lambda = \frac{\Omega M_{\text{shaft}}}{\frac{1}{2}\rho(\Omega R_{\text{tip}})^3} \tag{7.3}$$

Note that the pressure coefficient is the nondimensional difference between the *static* pressure at outlet and the *total* pressure are inlet.
The comparison between measured and computed performance characteristics is shown in Figure 7.17.

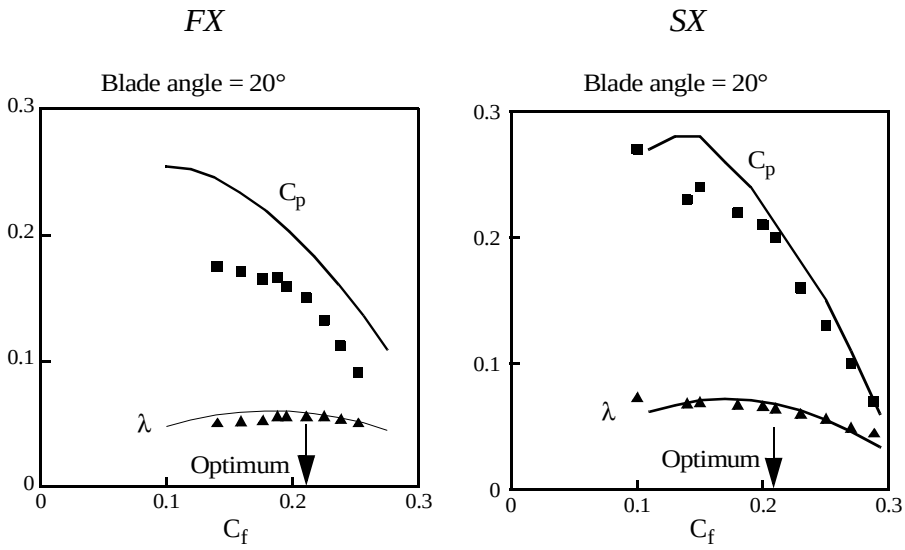

FIGURE 7.17. Measured and computed performance characteristics of FX and SX axial cooling fans.

CHAPTER 8

Boundary layers

This chapter deals with basic boundary-layer theory (textbooks on boundary-layer theory are [8], [9] and [10]). The focus is on two-dimensional wall-bounded boundary layers and incompressible flows. The emphasis is on the effect of pressure gradients outside the boundary layers, since this effect is important in applications to turbomachines.

This chapter deals with basic boundary-layer theory (textbooks on boundary-layer theory are [8], [9] and [10]). The focus is on two-dimensional wall-bounded boundary layers and incompressible flows. The emphasis is on the effect of pressure gradients outside the boundary layers, since this effect is important in applications to turbomachines.

For turbines the pressure gradient is generally favourable (accelerating flow), while for pumps and compressors the pressure gradient is generally adverse (decelerating flow).

Firstly, the boundary-layer concept is described, followed by the formulation of the boundary-layer equations in the two-dimensional case of incompressible flow. A distinction is made between the laminar and the turbulent case.

Basic boundary-layer methods are described for calculating laminar and turbulent boundary-layers. These methods take into account the pressure gradient, or equivalently the variation of the velocity, outside the boundary layer.

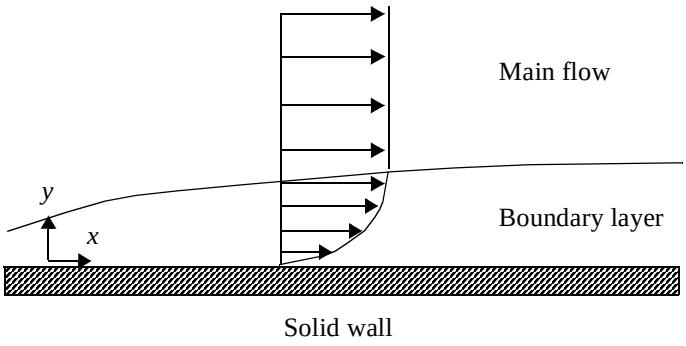

FIGURE 8.1. Sketch of the boundary layer near a solid wall.

Boundary-layer concept

As was shown in Chapter 2, in many cases the core flow may be considered as inviscid for the high Reynolds-numbers that are typical for turbomachinery flows. Hence, viscous shear stresses can be neglected in the main flow. Close to solid walls this assumption generally does not hold, since at the wall the no-slip condition applies. So there will be a rapid change in velocity in the direction normal from the wall, with zero velocity at the wall, to the main flow velocity at a small distance from the wall. This large gradient in velocity corresponds to (non-negligible) shear stresses. Thus, close to the solid walls the

assumption of inviscid flow is not correct. Inside the thin boundary-layer viscous shear-stresses can not be neglected. However, by taking into account that boundary layers are thin, other simplifying assumptions can be made that lead to simplified forms of the Navier-Stokes equations that are appropriate to the flow in boundary layers.

Boundary-layer thicknesses

boundary-layer (disturbance) thickness

Inside the boundary-layer the velocity component parallel to the wall, $u(x, y)$ with x the coordinate along the solid wall and y the distance normal to the wall, changes from zero towards the main-flow velocity $U(x)$. The *boundary-layer disturbance thickness* δ is usually defined as the distance from the wall to the point where the velocity is within 1% (or another percentage) of the freestream velocity of the core flow. This point is difficult to measure, since the velocity profile merges smoothly with the main flow. Furthermore, the 1% criterion is arbitrary. Therefore, two other boundary-layer thicknesses are introduced.

The viscous forces that are important in the boundary layer result in a retardation of the flow in comparison with the main flow. Thus, the mass-flow rate adjacent to the solid wall is smaller than that in the main flow. The mass-flow rate (per unit depth) is given by $\int_0^\infty \rho u(x, y)dy$. The decrease in mass-flow rate, relative to the corresponding mass-flow rate of a uniform inviscid flow (that would not approach zero at the wall) is given by $\int_0^\infty \rho[U(x) - u(x, y)]dy$. The *boundary-layer displacement thickness* δ^* is defined as the distance over which the solid wall would have to be displaced to give the same mass-flow deficit as that which exists in the boundary layer. Thus, the boundary-layer displacement thickness δ^* is defined by

boundary-layer displacement thickness

$$\rho U(x)\delta^*(x) = \int_0^\infty \rho[U(x) - u(x, y)]dy \tag{8.1}$$

Besides leading to a reduction of the mass-flow rate, the boundary layer also results in a reduction of the momentum transport. The momentum deficit of the actual mass-flow, $\int_0^\infty \rho u(x, y)dy$, through the boundary layer is $\int_0^\infty \rho u(x, y)[U(x) - u(x, y)]dy$. If viscous forces were absent, it would be necessary to move the solid wall outwards to obtain a momentum deficit. Denoting this distance, the *boundary-layer momentum thickness*, by θ, this deficit is equal to $\rho U(x)^2\theta(x)$. Thus the momentum thickness is defined as the thickness of a layer of fluid with velocity $U(x)$, for which the momentum flux is equal to the deficit of momentum flux through the boundary layer. Thus, the boundary-layer momentum thickness θ is defined by

boundary-layer momentum thickness

$$\rho U(x)^2\theta(x) = \int_0^\infty \rho u(x, y)[U(x) - u(x, y)]dy \tag{8.2}$$

Since the displacement thickness and the momentum thickness are defined as integrals with an integrand that vanishes in the main flow (where $u(x, y) = U(x)$), they are appreciably easier to determine experimentally than the boundary-layer disturbance thickness δ.

With constant density ρ the displacement thickness δ^* and the momentum thickness θ can be written as

$$\begin{aligned} \delta^*(x) &= \int_0^\infty \left[1 - \frac{u(x, y)}{U(x)}\right]dy \\ \theta(x) &= \int_0^\infty \frac{u(x, y)}{U(x)}\left[1 - \frac{u(x, y)}{U(x)}\right]dy \end{aligned} \tag{8.3}$$

Hence these thicknesses involve the shape of the non-dimensional velocity profile within the boundary layer. A non-dimensional parameter related to the shape of the velocity profile within the boundary layer is the *shape factor* H defined by

shape factor

$$H = \frac{\delta^*}{\theta} \tag{8.4}$$

For example, with a (often used) power-law velocity profile, $u(x, y)/U(x) = [y/\delta(x)]^{1/n}$, we find that $H = (n + 2)/n$.

Boundary-layer equations

The equations governing two-dimensional, incompressible and steady flows are the continuity equation and the two-dimensional Navier-Stokes equations. The case considered is that of the flow near a flat, solid wall. The essential assumption made in boundary-layer theory is that the boundary layer is thin, and that changes in the x-direction, along the wall, are much slower than changes in the y-direction, perpendicular to the wall. With characteristic length scales L for the x-direction and δ for the y-direction, this assumption requires

$$\frac{\delta}{L} \ll 1 \tag{8.5}$$

Laminar flow

The continuity equation (2.5) for incompressible flow is

$$\frac{\partial u}{\partial x} + \frac{\partial v}{\partial y} = 0 \tag{8.6}$$

where $u(x, y)$ and $v(x, y)$ are the velocity components along the wall and perpendicular to the wall, respectively.

For laminar flow the steady, two-dimensional Navier-Stokes equations (2.6), with (2.8) for the shear stress, for incompressible flow are

$$\begin{aligned} u\frac{\partial u}{\partial x} + v\frac{\partial u}{\partial y} &= -\frac{1}{\rho}\frac{\partial p}{\partial x} + \nu\left(\frac{\partial^2 u}{\partial x^2} + \frac{\partial^2 u}{\partial y^2}\right) \\ u\frac{\partial v}{\partial x} + v\frac{\partial v}{\partial y} &= -\frac{1}{\rho}\frac{\partial p}{\partial y} + \nu\left(\frac{\partial^2 v}{\partial x^2} + \frac{\partial^2 v}{\partial y^2}\right) \end{aligned} \tag{8.7}$$

Now the order of magnitude of the various terms will be investigated. Characteristic velocity scales for u and v are U and V, respectively. The order of magnitude of the first term in the continuity equation is $O(U/L)$, while that of the second is $O(V/\delta)$. Hence it follows that $V = (\delta/L)U$.

Now an order of magnitude analysis of the Navier-Stokes equation for the x-direction is performed, using the result for the velocity scale V. The order of magnitude of the first two terms on the left-hand side is $O(U^2/L)$, as is that of the term with the pressure gradient. The order of magnitude of the two viscous terms are $O([\nu U]/L^2)$ and $O([\nu U]/\delta^2)$, respectively. Hence the first viscous term is smaller, by a factor $O([\delta/L]^2)$, than the second viscous term.

Similarly, the order of magnitude analysis of the Navier-Stokes equation for the y-direction is performed. The order of magnitude of the first two terms on the left-hand side is $O([U^2/L][\delta/L])$, while that of the term with the pressure gradient is

$O([U^2/L][L/\delta])$. The order of magnitude of the two viscous terms is $O([U^2/L][\delta/L][\nu/(UL)])$ and $O([U^2/L][L/\delta][\nu/(UL)])$, respectively. Hence the first viscous term is smaller, by a factor $O([\delta/L]^2)$, than the second term.
From this analysis of the order of magnitude it follows that the two viscous terms containing derivatives with respect to x can be neglected. Since viscous terms are, almost by definition, important in boundary layers it follows that the order of magnitude of the terms on the left-hand side of the Navier-Stokes equations for the x-direction, $O(U^2/L)$, must be equal to the magnitude of the second viscous term, $O([\nu U]/\delta^2)$. This means that $\delta/L = O([\nu/(UL)]^{1/2})$. From these results it follows that the dominant term, by a factor $O([\delta/L]^2)$, in the Navier-Stokes equation for the y-direction is the term with the pressure gradient. The resulting, simplified equation is thus $\partial p(x, y)/\partial y = 0$, which means that inside of the boundary layer the pressure does not change in the direction perpendicular to the wall. Hence the pressure inside the boundary layer is equal to that outside the boundary layer, which (is assumed to) satisfy the Bernoulli equation, so $\partial p/\partial x = -(1/\rho)UdU/dx$.
The resulting steady, two-dimensional boundary equations for incompressible laminar flow become

$$\begin{aligned} u\frac{\partial u}{\partial x} + v\frac{\partial u}{\partial y} &= U\frac{dU}{dx} + \nu\frac{\partial^2 u}{\partial y^2} \\ 0 &= -\frac{1}{\rho}\frac{\partial p}{\partial y} \end{aligned} \tag{8.8}$$

Note that, unlike in the Navier-Stokes equations, the pressure no longer is an unknown. The pressure inside the boundary layer is equal to that outside the boundary layer. In turn, this pressure is determined from the Bernoulli equation for the inviscid, irrotational main flow.

Turbulent flow

Turbulent flow is characterised by irregular, time-dependent fluctuations. Since these high-frequency variations are generally not of interest, it is common to employ a so-called *Reynolds decomposition*. The instantaneous velocity vector $\tilde{\underline{v}}(\underline{x}, t)$ is decomposed into a mean, time-independent velocity vector $\bar{\underline{v}}(\underline{x})$ and a fluctuation $\underline{v}'(\underline{x}, t)$

$$\tilde{\underline{v}}(\underline{x}, t) = \bar{\underline{v}}(\underline{x}) + \underline{v}'(\underline{x}, t) \tag{8.9}$$

Similarly, the pressure is decomposed into a mean and a fluctuation pressure.
The fluctuation is chosen such that its time-average value (over a long period T) is zero

$$\overline{\underline{v}'(\underline{x}, t)} = 0 \tag{8.10}$$

Here the overbar denoted the time average. For an arbitrary quantity $\phi(\underline{x})$ this average is defined by

$$\overline{\phi(\underline{x})} = \lim_{T\to\infty}\frac{1}{T}\int_0^T \phi(\underline{x}, t')dt' \tag{8.11}$$

The steady, two-dimensional Reynolds-averaged Navier-Stokes equations (*RANS* for short) for incompressible flow become after some algebra

Reynolds-averaged Navier-Stokes equations

$$\begin{aligned} \bar{u}\frac{\partial}{\partial x}\bar{u} + \bar{v}\frac{\partial}{\partial y}\bar{u} &= -\frac{1}{\rho}\frac{\partial}{\partial x}\bar{p} + \nu\left(\frac{\partial^2\bar{u}}{\partial x^2} + \frac{\partial^2\bar{u}}{\partial y^2}\right) - \frac{\partial}{\partial x}(u'u') - \frac{\partial}{\partial y}(u'v') \\ \bar{u}\frac{\partial}{\partial x}\bar{v} + \bar{v}\frac{\partial}{\partial y}\bar{v} &= -\frac{1}{\rho}\frac{\partial}{\partial y}\bar{p} + \nu\left(\frac{\partial^2\bar{v}}{\partial x^2} + \frac{\partial^2\bar{v}}{\partial y^2}\right) - \frac{\partial}{\partial x}(u'v') - \frac{\partial}{\partial y}(v'v') \end{aligned} \tag{8.12}$$

where $\bar{u}$, $\bar{v}$ are the components of the time-averaged velocity vector in x-direction and y-direction, respectively, and u', v' are the components of the fluctuating velocity vector in x-direction and y-direction, respectively. The terms on the right-hand side involving the fluctuating velocities are effectively additional stresses, the so-called *Reynolds stresses* $\rho u'v'$ (and similar terms), due to momentum transfer that is the result of the random fluctuation velocities. These terms are a result of the nonlinear character of the Navier-Stokes equations.

A central problem in the study of turbulence is that, by the process of Reynolds averaging, extra unknowns, such as $u'v'$, have been introduced into the equations. Now the number of unknowns exceeds the number of equations. Therefore these additional unknowns have to be related to the primary unknowns. This is the *closure problem* in turbulence. It forms one of the major unsolved (unsolvable perhaps) problems in fluid mechanics. An advanced textbook on turbulence is [30].

Using the Reynolds decomposition (8.9), the continuity equation (8.6) becomes

$$\frac{\partial}{\partial x}\bar{u} + \frac{\partial}{\partial y}\bar{v} = 0 \tag{8.13}$$

Now an order of magnitude analysis is made of the Reynolds-averaged Navier-Stokes equations. It is assumed that all fluctuating terms ($u'u'$, $u'v'$ and $v'v'$) are of the same order of magnitude. From the order of magnitude of the continuity equation, it follows $V = (\delta/L)U$, just as in the laminar case. Similarly to the analysis of laminar boundary-layers, the terms involving derivatives with respect to x of viscous and Reynolds stress can be neglected in comparison to the terms involving derivatives with respect to y. The order of magnitude of the inertia terms on the left-hand side is the same as in the laminar case. On the right-hand side, the terms with derivatives with respect to x will be smaller, by an order of magnitude δ/L, than the terms involving derivatives with respect to y. Hence these smaller terms will be neglected. Except very close to the wall the viscous stresses will be smaller than the Reynolds stresses for turbulent boundary layers. Thus we find

$$\begin{aligned} \bar{u}\frac{\partial}{\partial x}\bar{u} + \bar{v}\frac{\partial}{\partial y}\bar{u} &= -\frac{1}{\rho}\frac{\partial}{\partial x}\bar{p} + \nu\frac{\partial^2\bar{u}}{\partial y^2} - \frac{\partial}{\partial y}(u'v') \\ 0 &= -\frac{1}{\rho}\frac{\partial}{\partial y}\bar{p} - \frac{\partial}{\partial y}(v'v') \end{aligned} \tag{8.14}$$

From detailed experimental studies it is known that the Reynolds stress $\rho v'v'$ does not vary significantly over the boundary layer. From the previous equation it follows that $\partial\bar{p}/\partial y = 0$. Hence the pressure inside the boundary layer is equal to that outside the boundary layer, which (is assumed to) satisfy the Bernoulli equation, so $\partial\bar{p}/\partial x = -(1/\rho)UdU/dx$, just as in the laminar case. Finally, we obtain

$$\begin{aligned} \bar{u}\frac{\partial}{\partial x}\bar{u} + \bar{v}\frac{\partial}{\partial y}\bar{u} &= U\frac{dU}{dx} + \nu\frac{\partial^2\bar{u}}{\partial y^2} - \frac{\partial}{\partial y}(u'v') \\ 0 &= -\frac{1}{\rho}\frac{\partial}{\partial y}\bar{p} \end{aligned} \tag{8.15}$$

Momentum integral equation

The boundary-layer equations for laminar and turbulent boundary layers (8.8) and (8.15) both can be written as

$$u\frac{\partial u}{\partial x} + v\frac{\partial u}{\partial y} = U\frac{dU}{dx} + \frac{1}{\rho}\frac{\partial \tau_{xy}}{\partial y}$$
$$0 = -\frac{1}{\rho}\frac{\partial p}{\partial y} \tag{8.16}$$

where the overbars for the velocities and pressure have been dropped in the turbulent case to simplify the notation. The *total* shear stress τ_{xy}, consisting of laminar shear-stress and turbulent Reynolds-stress, is defined as

$$\tau_{xy} = \mu\frac{\partial u}{\partial y} - \rho\overline{u'v'} \tag{8.17}$$

By adding u times the continuity equation to (8.16) we obtain

$$\frac{\partial}{\partial x}(u^2) + \frac{\partial}{\partial y}(uv) = U\frac{dU}{dx} + \frac{1}{\rho}\frac{\partial \tau_{xy}}{\partial y} \tag{8.18}$$

Integrating from $y = 0$ to $y = \Delta > \delta$, with Δ arbitrary but independent of x, gives after using the no-slip condition at the wall, $v|_{y=0} = 0$, and that the shear stresses are zero, $\tau_{xy}|_{y=\Delta} = 0$, outside the boundary layer

$$\int_0^\Delta \frac{\partial}{\partial x}(u^2)dy + (uv)|_{y=\Delta} = \int_0^\Delta U\frac{dU}{dx}dy - \frac{1}{\rho}\tau_w \tag{8.19}$$

where τ_w is the shear stress at the wall, i.e. $\tau_w = \tau_{xy}|_{y=0}$. By integrating the continuity equation from $y = 0$ to $y = \Delta$ and using the no-slip condition at the wall, $v|_{y=0} = 0$, we find that $v|_{y=\Delta} = -\int_0^\Delta \partial u/\partial x dy$. At $y = \Delta$, outside the boundary layer, we have $u|_{y=\Delta} = U$. Thus we obtain

$$\int_0^\Delta \left[\frac{\partial}{\partial x}(u^2) - U\frac{\partial u}{\partial x} - U\frac{dU}{dx}\right]dy = -\frac{1}{\rho}\tau_w \tag{8.20}$$

After some rewriting of the left-hand side we find

$$\int_0^\Delta \left[-\frac{\partial}{\partial x}[u(U-u)] - (U-u)\frac{dU}{dx}\right]dy = -\frac{1}{\rho}\tau_w \tag{8.21}$$

Since $U - u = 0$ for $y > \delta$, both parts on the left-hand side contribute only for $y < \delta$, and hence are independent of Δ. Thus

$$\int_0^\Delta -\frac{\partial}{\partial x}[u(U-u)]dy = -\frac{d}{dx}\int_0^\Delta [u(U-u)]dy \tag{8.22}$$

and hence

$$\frac{d}{dx}\int_0^\Delta [u(U-u)]dy + \frac{dU}{dx}\int_0^\Delta (U-u)dy = \frac{\tau_w}{\rho} \tag{8.23}$$

Using the definitions (8.3) of the displacement boundary-layer thickness δ^* and the momentum boundary-layer thickness θ, we obtain the von Karman *momentum integral equation*

momentum integral equation

$$\frac{d}{dx}(U^2\theta) + \delta^* U\frac{dU}{dx} = \frac{\tau_w}{\rho} \tag{8.24}$$

This equation can be rewritten as

$$\frac{d\theta}{dx} = \frac{1}{2}c_f - (H+2)\frac{1}{U}\frac{dU}{dx}\theta \tag{8.25}$$

where H is the shape factor defined in (8.4) and c_f is the *friction coefficient* defined by

friction coefficient

$$c_f = \frac{\tau_w}{\frac{1}{2}\rho U^2} \tag{8.26}$$

The momentum integral equation (8.25) shows that accelerating outer flows (as frequently encountered in turbine flows) tend to reduce the momentum thickness θ, while decelerating outer flows (as frequently encountered in pump and compressor flows) tend to increase the momentum thickness θ. Thick boundary layers, with lower wall shear-stress, are more prone to separation than thin boundary layers.

Entrainment equation

The entrainment velocity v_E is defined as the velocity component that is normal to the "edge" $y = \delta(x)$ of the boundary layer, see also Figure 8.2. From the mass conservation equation (with constant density ρ) applied to the control volume *CV* sketched in Figure 8.2, it follows that

entrainment velocity

$$v_E(x) = \frac{d}{dx}\int_0^{\delta(x)} u(x,y)dy \tag{8.27}$$

The meaning of v_E is the rate at which fluid from outside the boundary-layer (which is effectively inviscid) is "entrained" into the boundary layer where viscous effects are important. Note that the edge of the boundary layer is *not* a streamline!

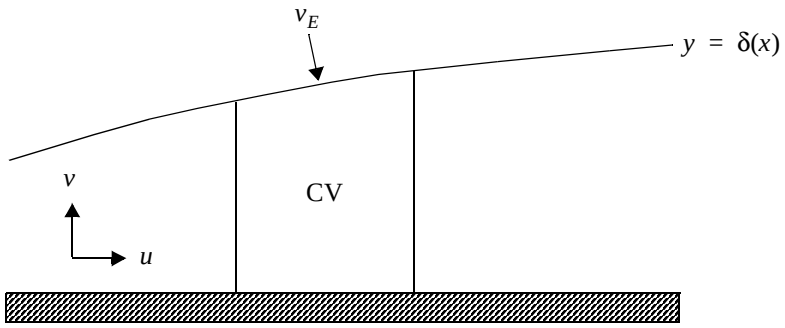

FIGURE 8.2. Definition of entrainment velocity.

Since v_E is the velocity component normal to the edge $y = \delta(x)$ of the boundary layer it follows that $v_E = u|_{y=\delta} n_1 + v|_{y=\delta} n_2$ where $(n_1, n_2)^T$ is the (inward) unit vector normal to the edge of the boundary layer. Since $d\delta/dx \ll 1$, the normal vector is given by $(n_1, n_2)^T \cong (d\delta/dx, -1)^T$ (the approximation made is that the length of this vector is not exactly equal to 1). Hence we obtain

$$v_E = u\big|_{y=\delta}\frac{d\delta}{dx} - v\big|_{y=\delta} \tag{8.28}$$

From the definition (8.3) of the displacement thickness δ^* and assuming that the integrand equals zero for $y \geq \delta$, it follows that

$$\frac{d}{dx}(U\delta^*) = \frac{d}{dx}\int_0^{\delta}(U-u)\,dy \tag{8.29}$$

By splitting the terms on the right-hand side we obtain

$$\frac{d}{dx}(U\delta^*) = \frac{d}{dx}(U\delta) - \frac{d}{dx}\int_0^{\delta} u\,dy \tag{8.30}$$

Using the definition (8.27) of the entrainment velocity v_E, it follows that

$$\frac{d}{dx}[U(\delta-\delta^*)] = v_E \tag{8.31}$$

Laminar flow: Pohlhausen's method

A method for predicting the characteristics of laminar boundary-layers that uses the momentum integral equation is Pohlhausen's method.
Firstly, a velocity profile is postulated, based on some observations of 'suitable' velocity profiles. The velocity is defined for $0 \leq y \leq \delta$. At the edge of the boundary layer, $y = \delta$, it must smoothly match the velocity $U(x)$ outside the boundary layer. Hence we require

$$u\big|_{y=\delta} = U \qquad \left.\frac{du}{dy}\right|_{y=\delta} = 0 \qquad \left.\frac{\mathrm{d}^2u}{\mathrm{d}y^2}\right|_{y=\delta} = 0 \tag{8.32}$$

At the wall, $y = 0$, we have

$$u\big|_{y=0} = 0 \qquad \left.\frac{\mathrm{d}^2u}{\mathrm{d}y^2}\right|_{y=0} = -\frac{1}{\nu}U\frac{dU}{dx} \tag{8.33}$$

The latter condition follows from (8.8) for $y = 0$, where $u = 0$ and $v = 0$. A polynomial form for the non-dimensional velocity $u(x, y)/U(x)$ in terms of the non-dimensional coordinate $\zeta = y/\delta(x)$ is postulated

$$\frac{u}{U} = a_0 + a_1\zeta + a_2\zeta^2 + a_3\zeta^3 + a_4\zeta^4 \tag{8.34}$$

The coefficients can be determined from the conditions (8.32) and (8.33). The result is (a nice Maple exercise?)

$$a_0 = 0 \qquad a_1 = 2 + \frac{\Lambda}{6} \qquad a_2 = -\frac{\Lambda}{2} \qquad a_3 = -2 + \frac{\Lambda}{2} \qquad a_4 = 1 - \frac{\Lambda}{6} \tag{8.35}$$

where the non-dimensional pressure-gradient parameter Λ is given by

$$\Lambda = \frac{\delta^2}{\nu}\frac{dU}{dx} \tag{8.36}$$

with $\Lambda < 0$ for a decelerating outer flow, $\Lambda = 0$ for an outer flow with constant velocity and $\Lambda > 0$ for an accelerating outer flow. This velocity profile is shown in Figure 8.3 for various values of Λ. Note that for $\Lambda = -12$, the shear stress at the wall, $\mu \partial u/\partial y|_{y=0}$, becomes zero, which is indicative for boundary-layer separation.
With the velocity profile thus expressed in terms of U, its derivative dU/dx and the boundary-layer (disturbance) thickness δ, the boundary-layer thicknesses δ^* and θ can be determined from (8.3), as well as the friction coefficient c_f from (8.26), since $\tau_w = \mu \partial u/\partial y|_{y=0}$. The results are

$$\frac{\delta^*}{\delta} = \frac{3}{10} - \frac{\Lambda}{120} \qquad \frac{\theta}{\delta} = \frac{37 - \frac{\Lambda}{3} - \frac{5}{144}\Lambda^2}{315} \qquad c_f = \frac{2\nu}{\delta U}\left(2 + \frac{\Lambda}{6}\right) \tag{8.37}$$

With these relations an ordinary differential equation is obtained for $\delta(x)$, which can be solved (numerically) with an initial condition.
For an outer flow with constant U, i.e. $\Lambda = 0$, we find

$$\frac{\delta(x)}{x} = 5.85\left(\frac{Ux}{\nu}\right)^{-1/2} \qquad c_f = 0.68\left(\frac{Ux}{\nu}\right)^{1/2} \tag{8.38}$$

The 'exact' solution (based on the solution of the boundary-layer equations in differential form, i.e. not integrated over the boundary layer) is the so-called Blasius solution, see [2]. For the friction coefficient c_f it gives $c_f = 0.66[(Ux)/\nu]^{1/2}$. So the simplified Pohlhausen method gives accurate results.
Note that other assumptions for the velocity profile within the boundary layer lead to different numerical values for ratios like δ^*/δ. Generally, the results are not extremely sensitive to the shape of the velocity profile. Some examples are given in [2].
Another integral method for laminar boundary-layers, which uses using empirical relations, is that of Thwaites, see for example [8].

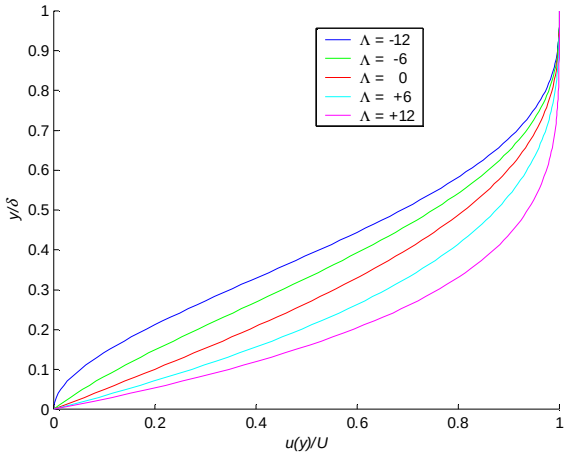

FIGURE 8.3. Pohlhausen velocity profile for various values of the pressure-gradient parameter Λ.

Turbulent flow: Head's method

For turbulent flow the method of assuming a velocity profile $u/U = f(y/\delta)$ does not work as in the laminar case, since the turbulent boundary-layer has a composite structure that accounts for the different scaling behaviour of the viscous-dependent part of the profile very close to the wall and the remaining Reynolds-stress part of the profile further away from the wall.

In order to use the momentum integral equation (8.27) without assuming a velocity profile, (empirical) relations involving the friction coefficient c_f and the shape factor H must be formulated.

In the method of Head (see for example [8] and [9]) the empirical relation due to Ludwieg & Tillmann is used for the wall-friction coefficient c_f

$$c_f = 0.246\times10^{-0.678H}Re_\theta^{-0.268} \tag{8.39}$$

where $Re_\theta = (U\theta)/\nu$.

In this method it is assumed that the nondimensional entrainment velocity, v_E/U, see (8.27), is solely a function of the shape factor H

$$\frac{v_E}{U} = \frac{1}{U}\frac{d}{dx}\int_0^\delta u\,dy = \frac{1}{U}\frac{d}{dx}[U(\delta-\delta^*)] = F(H) \tag{8.40}$$

Defining another shape factor H_1 by

$$H_1 = \frac{\delta-\delta^*}{\theta} \tag{8.41}$$

then the right-hand side equality in (8.40) can be written as

$$\frac{d}{dx}[U\theta H_1] = UF(H) \tag{8.42}$$

This other shape factor H_1 is assumed to be a function of the shape factor H only

$$H_1 = G(H) \tag{8.43}$$

Based on experimental data, a fit for the functions F and G was formulated

$$F = 0.0306(H_1-3.0)^{-0.6169} \tag{8.44}$$

$$G = \begin{cases} 0.8234(H-1.1)^{-1.287}+3.3 & H\le 1.6 \\ 1.5501(H-0.6778)^{-3.064}+3.3 & H\ge 1.6 \end{cases} \tag{8.45}$$

The resulting method consists of two ordinary differential equations (8.25) and (8.42) for θ and H. These differential equations can be solved (numerically) with initial conditions for θ and H.

Transition and separation

Separation of laminar boundary layers can be predicted with Thwaites criterion

$$\lambda \equiv \frac{\theta^2}{\nu}\frac{dU}{dx} \leq -0.082 \tag{8.46}$$

An empirical relation for predicting transition, from laminar to turbulent, of the state of the boundary layer is Michel's criterion

$$Re_{\theta,\,\mathrm{trans}} = 1.174\left(1 + \frac{22400}{Re_{x,\,\mathrm{trans}}}\right) Re_{x,\,\mathrm{trans}}^{0.46} \tag{8.47}$$

where $Re_\theta = U\theta/\nu$, $Re_x = Ux/\nu$ and the subscripts "trans" denote values at transition.

Other factors affecting transition, such as level of freestream turbulence, surface roughness and surface curvature, are discussed in [9].

The criterion for separation of the turbulent boundary layers in Head's method is that the shape factor H exceeds a certain threshold value H_{sep}, typically $H_{\mathrm{sep}} = 1.8 - 2.4$. Note that according to (8.39), $c_f \to 0$ corresponds to $H \to \infty$.

CHAPTER 9

Design aspects

This chapter deals with elementary considerations of some design methods for impellers and volutes and an outline of some advanced topics.

Impeller

Here two aspects of the design of impellers will be discussed. The first deals with the shape of the inlet to optimise the cavitation characteristics, while the second deals with considerations that are used to determine the blade shape.

Cavitation

cavitation inception

In the vicinity of the leading edge of the impeller the fluid has to accelerate in order to follow the rotating movement of the blades. This acceleration leads to a drop of the static pressure which may lead to the static pressure dropping below the vapour pressure. When this happens, vapour bubbles will form. The instant where the first vapour bubbles form is called *cavitation inception*. A simple, one-dimensional analysis will be given that gives the inlet stagnation pressure at which cavitation inception occurs.
Upstream of the impeller the static pressure equals

$$p_1 = p_{01} - \frac{1}{2}\rho c_{1x}^2 \tag{9.1}$$

At the point of cavitation inception the local pressure equals the vapour pressure p_v

$$p_v = p = p_1 - \sigma_b \frac{1}{2}\rho w_1^2 \tag{9.2}$$

blade coefficient

where the empirical *blade coefficient* σ_b depends on the blade shape and flow incidence. The latter term is the static pressure drop due to the fluid being accelerated by the rotation of the blade near the leading edge.

Thus at cavitation inception

$$p_1 = p_{01} - \frac{1}{2}\rho c_{1x}^2 = p_v + \sigma_b \frac{1}{2}\rho w_1^2 \tag{9.3}$$

Or, using $w_1^2 = c_{1x}^2 + U_1^2$

$$gH_{\text{suct}} = \frac{p_{01} - p_v}{\rho} = \frac{1}{2}c_{1x}^2 + \sigma_b \frac{1}{2}w_1^2 = \frac{1}{2}c_{1x}^2(1 + \sigma_b) + \frac{1}{2}\sigma_b U_{1s}^2 \tag{9.4}$$

where H_{suct} is the net positive suction head and it is implied that this is measured at the shroud where the blade speed is highest.

suction specific speed

The optimum inlet conditions are now considered. The suction specific speed N_{suct} is defined as

$$N_{\text{suct}} = (\Omega Q^{1/2})/(gH_{\text{suct}})^{3/4} \tag{9.5}$$

where

$$\Omega = U_{1s}/r_{1s} \qquad Q = c_{1x}A_1 = \pi r_s^2\left(1 - \frac{r_h^2}{r_s^2}\right)c_{1x} \tag{9.6}$$

Now we obtain, with $\phi' = c_{1x}/U_{1s}$

$$\frac{N_{\text{suct}}^2}{\pi\left(1 - \frac{r_h^2}{r_s^2}\right)} = \frac{U_{1s}^2 c_{1x}}{\left[\frac{1}{2}c_{1x}^2(1+\sigma_b) + \frac{1}{2}\sigma_b U_{1s}^2\right]^{3/2}} = \frac{\phi'}{\left[\frac{1}{2}\phi'^2(1+\sigma_b) + \frac{1}{2}\sigma_b\right]^{3/2}} \tag{9.7}$$

The optimum cavitation condition is now determined by finding the maximum suction specific speed N_{suct} by differentiating this equation with respect to ϕ' and setting the result to zero. A maximum for N_{suct} means that the minimum inlet stagnation pressure is obtained that corresponds to operation without cavitation. The optimum conditions become

$$\begin{aligned} \phi &= \left(\frac{\sigma_b}{2(1+\sigma_b)}\right)^{1/2} \\ gH_{\text{suct}} &= \frac{3}{2}\sigma_b\left(\frac{1}{2}U_{1s}^2\right) \\ N_{\text{suct}}^2 &= \frac{3.420\left(1 - \frac{r_h^2}{r_s^2}\right)}{\sigma_b(1+\sigma_b)^{1/2}} \end{aligned} \tag{9.8}$$

Blade shape

meridional view

The full, three-dimensional geometry of impellers is generally very complicated. Usually they are represented in the form of a meridional view (see Figure 9.1) and a planar view (see Figure 9.2).

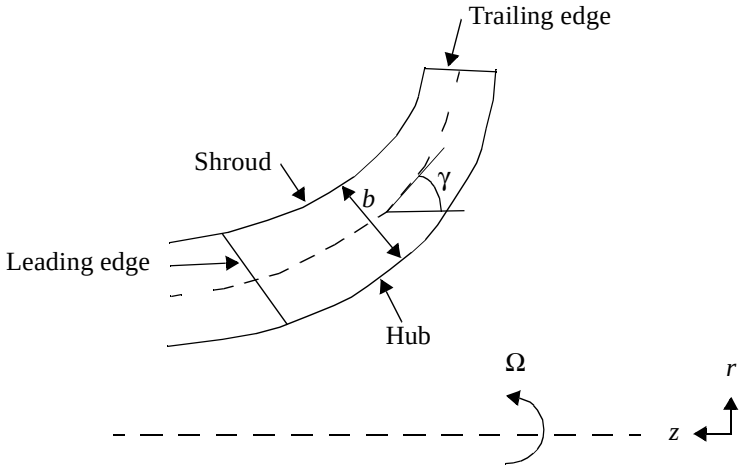

FIGURE 9.1. Meridional view of an impeller.

blade loading coefficient

Most design methods are based on a *blade loading coefficient*. Here the blade loading coefficient ξ is defined by

$$\xi = \frac{W_s - W_p}{\overline{W}} \tag{9.9}$$

where W_s and W_p are the magnitudes of the relative velocity at the suction and pressure side of the impeller blade, and $\overline{W}$ is their average, i.e. $\overline{W} = (W_s + W_p)/2$. From the definition of rothalpy (2.62) it follows that the blade loading coefficient is directly related to the pressure difference on the blade, and hence to the power input to the fluid

$$\frac{\Delta p}{\rho} = \frac{1}{2}(W_s^2 - W_p^2) = \frac{1}{2}(W_s + W_p)(W_s - W_p) = \overline{W}(W_s - W_p) \tag{9.10}$$

In most design methods it is recommended that the blade loading coefficient ξ should not exceed values in the range of 0.7 – 1.0.

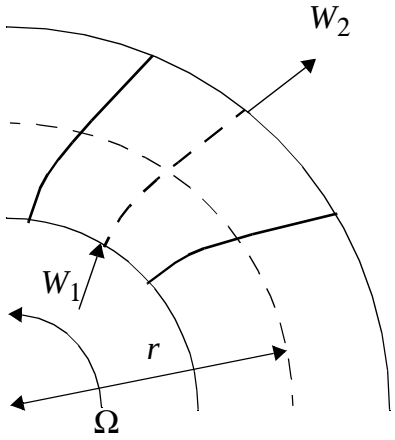

FIGURE 9.2. Planar view of impeller.

For an irrotational absolute velocity, the vorticity of the relative velocity is given by (2.55). The circulation of the relative velocity along the contour defined by the outline of the three-dimensional (nonplanar!) shaded area in Figure 9.3 is

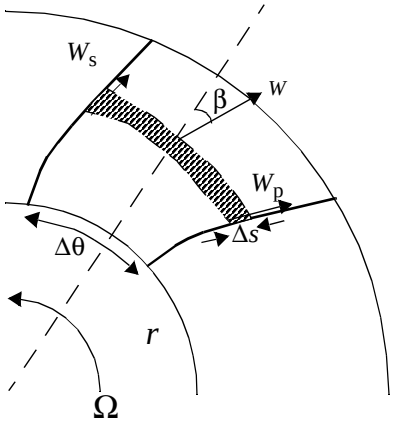

FIGURE 9.3. Section of part of an impeller.

$$\Gamma_{\text{rel}} = \oint_C \underline{w} \bullet d\underline{s} = \int_A \nabla \times \underline{w} \bullet \underline{dA} = -2\Omega A \sin\gamma = -2\Omega \sin\gamma r \Delta\theta \Delta m \tag{9.11}$$

The term $\sin\gamma$ arises because the vectorial surface $\underline{dA}$ is at an angle to the rotation axis.

The meridional distance Δm is related to the distance Δs in the planar view and the radial distance Δr by

$$\Delta r = \Delta m \sin\gamma = \Delta s \sin\gamma\cos\beta \tag{9.12}$$

The relative circulation can also be evaluated by integration of the velocity around the contour. This gives

$$\Gamma_{\text{rel}} = W_p \Delta s - W_s \Delta s - \frac{d}{ds}[W \sin\beta r \Delta\theta]\Delta s \tag{9.13}$$

or

$$W_s - W_p = -\frac{\Gamma_{\text{rel}}}{\Delta s} - \frac{d}{ds}[W \sin\beta r \Delta\theta] \tag{9.14}$$

Combining the previous equations gives

$$\frac{W_s - W_p}{r\Delta\theta} = 2\Omega \sin\gamma\cos\beta - \frac{\sin\gamma\cos\beta}{r\Delta\theta}\frac{d}{dr}[W \sin\beta r \Delta\theta] \tag{9.15}$$

The mass flow through the impeller channel is constant $\Delta M = \rho b r \Delta\theta W \cos\beta$. Hence, for incompressible flow this equation can be simplified, after some algebra, to

$$\frac{W_s - W_p}{r\Delta\theta} = 2\Omega \sin\gamma\cos\beta - W\left[\frac{d\beta}{dm} - \cos\beta \sin\beta \frac{1}{b}\frac{db}{dm}\right] \tag{9.16}$$

The left-hand side is related to the blade loading coefficient, which is assumed to be specified. Hence this equation is a differential equation for the blade angle β. An initial condition is needed for β. This can be obtained from the specified head and a slip factor, using a one-dimensional model.

Volute

The volute is one of the different types of diffusers that are used to collect the fluid and guide it to the exit pipe. An important function of the volute is to (try to) convert the high kinetic energy of the fluid leaving the impeller into pressure. The major velocity component of the fluid leaving the impeller is the tangential component, which is proportional to the blade tip speed.

method of constant angular momentum; Pfleiderer's method

The two most frequently used methods for the design of volutes are Stepanoff's method of constant circumferential velocity [6] and the method of constant angular momentum [5], [34]. Only the latter will be treated here. It is also known as Pfleiderer's method.
In this method it is assumed that the tangential and radial velocities are uniform around the impeller.
The moment exerted on the fluid by the impeller M_{imp} is

$$M_{\text{imp}} = \rho Q r v_\theta \tag{9.17}$$

With a impeller efficiency η_{imp} the impeller moment can be related to the head generated by the impeller H_{imp}

$$\eta_{\text{imp}} \Omega M_{\text{imp}} = \rho g Q H_{\text{imp}} \tag{9.18}$$

Note that the quantities η_{imp} and H_{imp} refer to the design point!
The tangential velocity becomes

$$rv_\theta = \frac{gH_{\text{imp}}}{\eta_{\text{imp}}\Omega} \tag{9.19}$$

Now a radial cross-section of the volute at angle θ is considered, see Figure 9.4. The flowrate through this cross-section equals

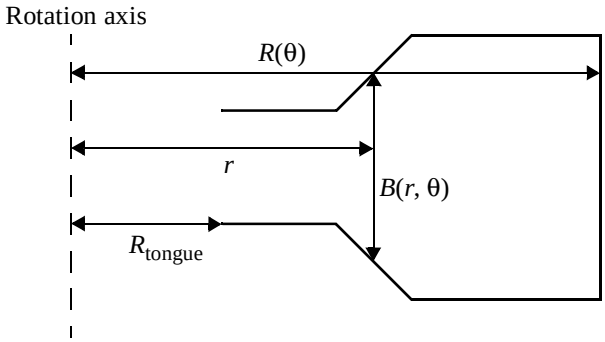

FIGURE 9.4. Cross-section of volute at angle θ.

$$Q(\theta) = \int_{R_{\text{tongue}}}^{R(\theta)} B(r,\theta)v_\theta dr = \frac{gH_{\text{imp}}}{\eta_{\text{imp}}\Omega}\int_{R_{\text{tongue}}}^{R(\theta)} \frac{B(r,\theta)}{r}dr \tag{9.20}$$

where R_{tongue} is the radius of the "tongue". Note that there must be some clearance between impeller and volute, so the radius of the tongue R_{tongue} must be larger than the radius of the trailing edge R_{te}.

Assuming that the outflow around the impeller is uniform $Q(\theta) = Q(\theta - \theta_{\text{tongue}})/(2\pi)$

$$\frac{(\theta - \theta_{\text{tongue}})}{2\pi}\frac{\eta_{\text{imp}}Q\Omega}{gH_{\text{imp}}} = \int_{R_{\text{tongue}}}^{R(\theta)} \frac{B(r,\theta)}{r}dr \tag{9.21}$$

From this equation the size of the volute as described by $R(\theta)$ can be determined.

In the two-dimensional case with constant width of the volute, i.e. $B(r, \theta) = B$, the resulting form of the volute, $R(\theta)$, becomes

$$\frac{R(\theta)}{R_{\text{tongue}}} = \exp\frac{(\theta - \theta_{\text{tongue}})}{2\pi}\frac{\eta_{\text{imp}}Q\Omega}{BgH_{\text{imp}}} \tag{9.22}$$

which is a logarithmic spiral.

Secondary flows

In many cases the flow entering a blade channel is not uniform. A prime example is the nonuniformity due to the presence of boundary layers on the blades, on the hub and on the shroud.

Consider a flow as sketched in Figure 9.5. The streamwise direction is denoted by s, while the blade-to-blade direction is n and the hub-to-shroud direction is b. In the region of uniform flow a typical streamline is indicated by AAA, while the streamline in the boundary layer is BBB. Outside of the boundary layers viscous effects may be neglected. If it is also assumed that the flow is steady and incompressible (constant den-

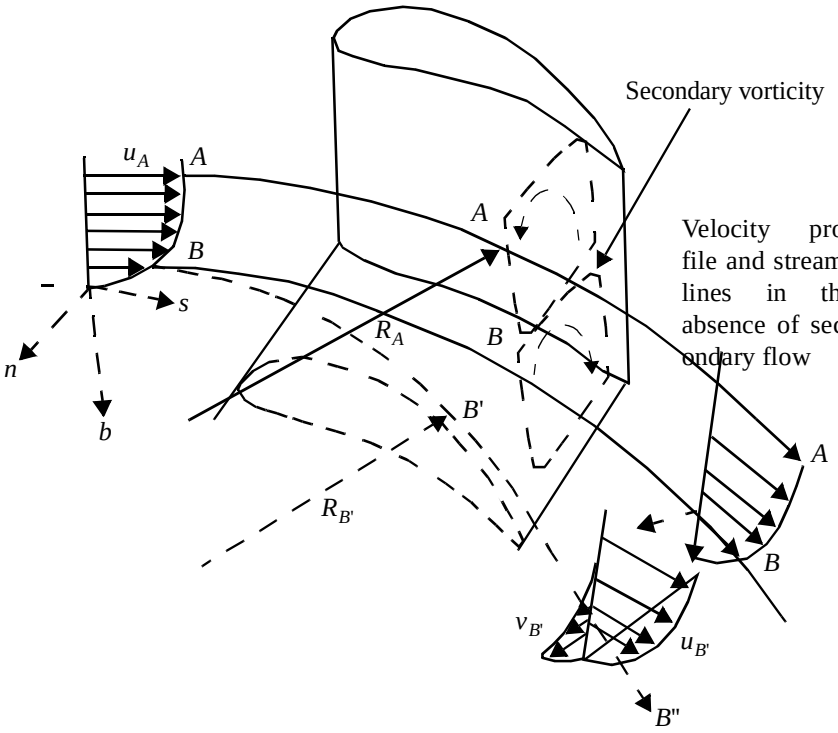

FIGURE 9.5. Secondary flow phenomenon.

sity) and that there is no variation of the flow in the n-direction, then the pressure gradient in the n-direction must be balanced by the centripetal acceleration. Hence

$$\left.\frac{\partial p}{\partial n}\right|_A = \frac{\rho u_A^2}{R_A} \tag{9.23}$$

where R_A is the radius of curvature of the streamline at A and the streamwise velocity is u_A.

When employing the usual boundary layer assumptions, it follows that the pressure gradient in n-direction should be constant in the boundary layer. Hence we obtain

$$\left.\frac{\partial p}{\partial n}\right|_A = \left.\frac{\partial p}{\partial n}\right|_B = \frac{\rho u_A^2}{R_A} > \frac{\rho u_B^2}{R_B} \tag{9.24}$$

secondary flow

Because $u_B < u_A$ and $R_B = R_A$, there is an imbalance between the pressure gradient in n-direction and the centripetal acceleration. Thus the streamline BBB will deflect more from that shown in Figure 9.5. The fluid particle originating at B would follows the path $BB'B"$, with $R_{B'} < R_B$, instead of BBB. The cross-flow v, which is the deviation from the main flow, is called the secondary flow.

From continuity considerations it follows that there are also spanwise velocities w: for a flow with constant streamwise direction $\partial u/\partial s = 0$, we find $\partial w/\partial b = -\partial v/\partial n$. This explanation provides a clear physical reasoning for the occurrence of secondary flow in a blade passage. Hence the secondary flow leads to vorticity in streamwise direction $\omega_s = -\partial v/\partial b + \partial w/\partial n$.

A similar reasoning can be presented to explain the occurrence of secondary flow due to Coriolis forces.

A more detailed description of secondary flows and of how they can be analysed quantitatively is given in [4].

Laser Doppler Velocimetry

For *non-intrusive* measurements of fluid velocities Laser Doppler Velocimetry (LDV) is often used. This method is based on Doppler effect, i.e. the change in wave length seen by a stationary observer when light reflects on a moving object. The frequency shift is proportional to the velocity of the object. Direct observation of this frequency shift is not possible, since it is far too small. Therefore a comparison is made between the original light and the reflected light.

When the object is a small particle that is carried with the fluid flow (negligible slip velocity), it becomes possible to measure the fluid velocity using LDV.

In LDV measurements a coherent light beam from a laser is split into two beam. These beams are focused into a “point”, the measurement volume, by a lens. The shift in frequency, the Doppler frequency, and its relation to the fluid velocity can be obtained from wave theory and from interference theory. The latter theory is explained here.

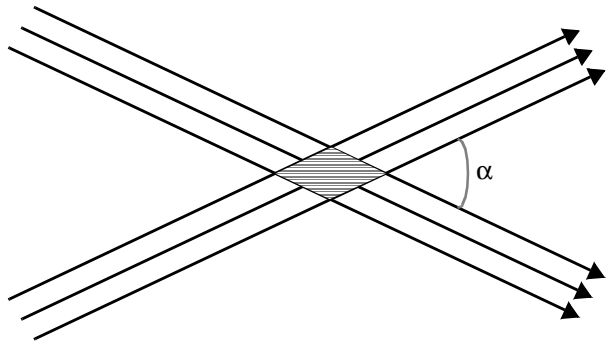

FIGURE 9.6. Interference pattern in the measurement volume.

As shown in Figure 9.6 in the region where the two beams come together an interference pattern of light and dark lines (fringes) arises. The distance Δx between the fringes depends on the wave length λ of the laser light and on the angle α between the two beams

$$\Delta x = \frac{\lambda}{2\sin\left(\frac{\alpha}{2}\right)} \tag{9.25}$$

A particle in the fluid that moves through the measurement volume will light up and extinguish with a certain frequency, depending on its velocity. This is the Doppler frequency shift Δf referred to before. It is related to the component of the velocity perpendicular to the fringes, $v_\perp$, by

$$\Delta f = \frac{v_\perp}{\Delta x} \tag{9.26}$$

Vaned diffuser

To be added.

Rotor dynamics

To be added.

Inverse-design methods

To be added.

CHAPTER 10

Literature

This chapter gives some references to text books on fluid mechanics, material for further reading and the list of references.

Text books on fluid mechanics

[1] Batchelor, G.K. (1967)
An introduction to fluid dynamics
Cambridge University Press, Cambridge, UK.

[2] Fox, R.W. & McDonald, A.T. (1998)
Introduction to fluid mechanics
John Wiley & Sons, New York, NY, USA.

Further reading on turbomachines

[3] Cumpsty, N.A. (1989)
Compressor aerodynamics
Longman Scientific & Technical, Harlow, UK.

[4] Lakshminarayana, B. (1996)
Fluid dynamics and heat transfer of turbomachinery
John Wiley & Sons, New York, NY, USA.

[5] Pfleiderer, C. (1949)
Die Kreiselpumpen für Flüssigkeiten und Gase, third edition
Springer Verlag, Berlin, Germany.

[6] Stepanoff, A.J. (1948)
Centrifugal and axial flow pumps: theory, design, and application
John Wiley & Sons, New York, NY, USA.

[7] Tuzson, J. (2000)
Centrifugal pump design
John Wiley & Sons, New York, NY, USA.

Further reading on boundary layers

[8] Cebeci, T. & Bradshaw, P. (1977)
Momentum transfer in boundary layers
McGraw-Hill, New York, NY, USA.

[9] Cebeci, T. & Cousteix, J. (1999)
Modeling and computation of boundary-layer flows
Springer Verlag, Berlin, Germany.

[10] Schlichting, H. (1968)
Boundary-layer theory
McGraw-Hill, New York, NY, USA.

Other references

[11] Abramowitz, M. & Stegun, I.A. (1972)
Handbook of mathematical functions
Dover Publications, New York, NY.

[12] Baskharone, E. & Hamed, A. (1981)
A new approach in cascade flow analysis using the finite element method
AIAA Journal **19** 65-71 (1981).

[13] Baren, M. van (1998)
Flow computations of axial fans (in Dutch)
M.Sc. Thesis, Department of Mechanical Engineering, University of Twente, The Netherlands.

[14] Bradshaw, P. (1996)
Turbulence modelling with application to turbomachinery
Progress Aerospace Science **32** 575-624.

[15] Combès, J.F. & Rieutord, E. (1992)
Numerical and experimental analysis of the flow in a centrifugal pump at nominal and partial flowrate
Proceedings *International Gas Turbine and Aeroengine Congress and Exposition*, Paper 92-GT-284.

[16] Daily, J.W. & Nece, R.E. (1960)
Chamber dimension effects on induced flow and friction resistance of enclosed rotating disks
Journal of Basic Engineering **82** 217-232.

[17] Denton, J.D. (1993)
Loss mechanisms in turbomachines
Journal of Turbomachinery **115** 621-656.

[18] Esch, B.P.M. van (1997)
Simulation of three-dimensional unsteady flow in hydraulic pumps
Ph.D. Thesis, Department of Mechanical Engineering, University of Twente, The Netherlands.

[19] Esch, B.P.M. van & Kruyt, N.P. (1995)
Analysis of the flow in a centrifugal pump using a multi-block finite element method for computing three-dimensional potential flows
ERCOFTAC Seminar and Workshop on 3D Turbomachinery Flow Prediction III, part III, pp.19-25, Val d'Isère, France.

[20] Esch, B.P.M. van & Kruyt, N.P. & Jonker, J.B. (1997)
An inviscid-viscous coupling method for computing flows in entire pump configurations.
Proceedings *Third ASME Pumping Machinery Symposium* FEDSM97-3373, June 1997, Vancouver, BC, Canada.

[21] Esch, B.P.M. van & Kruyt, N.P. (2001)
Hydraulic performance of a mixed-flow pump: unsteady inviscid computations and loss models
Journal of Fluids Engineering (Transactions of the ASME) **123** 256-264.

[22] Hendrickson, B. & Leland R. (1995)
An improved spectral graph partitioning for mapping parallel computations
SIAM Journal of Scientific Computing **16** 452-469.

[23] Kelder, J.D.H. & Dijkers, R.J.H. & Esch, B.P.M. van & Kruyt, N.P. (2001)
Experimental and theoretical study of the flow in the volute of a low specific-speed pump
Fluid Dynamics Research **28** 267-280.

[24] Kruyt, N.P. (2004)
COMPASS User Manual
Department of Mechanical Engineering, University of Twente, Enschede, The Netherlands.

[25] Kruyt, N.P. & Esch, B.P.M. van & Jonker, J.B. (1999)
A superelement-based method for computing unsteady three-dimensional potential flows in hydraulic turbomachines
Communications in Numerical Methods in Engineering **15** 381-397.

[26] Miner, S.M. & Flack, R.D. & Allaire, P.E. (1992)
Two-dimensional flow analysis of a laboratory pump
Journal of Turbomachinery **114** 333-339.

[27] Morel, P. (1993)
Ecoulements décolles dans une roue de pompe centrifuge. Conception et réalisation d'un banc d'essai. Analyse des pressions pariétales
Ph.D. Thesis University of Lille, Lille, France.

[28] Os, M.J. van (1998)
On the flow and cavitation inception of mixed-flow impellers
Ph.D. Thesis, Department of Mechanical Engineering, University of Twente, Enschede, The Netherlands.

[29] Paulino, G.H. & Menezes, I.V.M & Gattass, M. & Mukherjee, S. (1994)
Node and element resequencing using the Laplacian of a finite element graph
International Journal of Numerical Methods in Engineering **37** 1511-1555.

[30] Pope, S.B. (2000)
Turbulent flows
Cambridge University Press, Cambridge, UK.

[31] Tanner, M. (1998)
Theories for base pressure in incompressible steady base flow
Progress Aerospace Science **34** 423-480.

[32] Visser, F.C & Brouwers, J.J.H. & Jonker, J.B. (1999)
Fluid flow in a rotating low specific-speed centrifugal impeller passage
Fluid Dynamics Research **24** 275-292.

[33] Visser, F.C. (1996)
On the flow in centrifugal impellers
Ph.D. Thesis, Department of Mechanical Engineering, University of Twente, Enschede, The Netherlands.

[34] Worster, R.C. (1963)
The flow in volutes and its effect on centrifugal pump performance
Proceedings Institution Mechanical Engineers **117** 843-861.

[35] Zienkiewicz, O.C. & Taylor, R.L (1989)
The finite element method
McGraw-Hill, Maidenhead, UK.

[36] Zienkiewicz, O.C. & Zhu, J.Z. (1992)
The superconvergent patch recovery and a posteriori error estimates. Part I: the recovery technique
International Journal of Numerical Methods in Engineering **33** 1331-1364.

INDEX